Title
Probing correlated electron matter with infrared magneto- optics

Permalink
https://escholarship.org/uc/item/2s10f0s0

Author
LaForge, Andrew David

Publication Date
2009

Peer reviewed|Thesis/dissertation

UNIVERSITY OF CALIFORNIA, SAN DIEGO

Probing Correlated Electron Matter with Infrared Magneto-Optics

A dissertation submitted in partial satisfaction of the
requirements for the degree
Doctor of Philosophy

in

Physics

by

Andrew David LaForge

Committee in charge:

Professor Dimitri N. Basov, Chair
Professor Eric Fullerton
Professor Jorge Hirsch
Professor Shayan Mookherjea
Professor Sunil Sinha

2009

The dissertation of Andrew David LaForge is approved, and it is acceptable in quality and form for publication on microfilm and electronically:

Chair

University of California, San Diego

2009

DEDICATION

To Heather and Clara, the loves of my life.

EPIGRAPH

It's a magical world . . . Let's go exploring!
—Bill Watterson

TABLE OF CONTENTS

LIST OF FIGURES

LIST OF TABLES

ACKNOWLEDGEMENTS

The primary influence in my shaping as a scientist and critical thinker while at UCSD has been my advisor, Professor Dimitri Basov. He has given me well-balanced portions of direction and independence, as well as a steady example of generosity and dedication.

My time in the Basov lab has been hugely enriched by the comraderie of my colleagues. I am thankful for memorable discussions, friendships, and coffee times with the students and postdocs with whom I have overlapped.

I owe much gratitude to the UCSD Physics support staff; their gracious assistance allowed the experiments to happen. Special thanks to Jeff Phillips and Bob Parker for their patience and good humor.

This work is devoted to my family. To my wife Heather, my faithful encourager, friend, and co-adventurer, whose love has lit my path. To my daughter Clara, in whom I hope to inspire a love for learning, and by whom I am continually inspired. To my Mom and Dad, for encouraging me to explore. And to my sisters, to the expanded LaForge and Donahoe families, and to my family of friends in San Diego, Tacoma, and elsewhere; for their constant love and understanding.

Chapters 2, 3, and 4 are reprints of previously published material. See the acknowledgments at the end of each chapter for specific citations of the journal articles.

VITA

2003	B. S. in Physics and Mathematics *summa cum laude*, University of Puget Sound
2003-2009	Research Assistant, University of California, San Diego
2009	Ph. D. in Physics, University of California, San Diego

PUBLICATIONS

A. D. LaForge, A. J. Frenzel, B. C. Pursley, Tao Lin, Xinfei Liu, Jing Shi, and D. N. Basov, “Optical characterization of Bi_2Se_3 in magnetic field: Searching for topological insulators in the infrared”, in preparation.

A. D. LaForge,A. A. Schafgans, S. V. Dordevic, W. J. Padilla, K. S. Burch, Z. Q. Li, Kouji Segawa, Seiki Komiya, Yoichi Ando, J. M. Tranquada, and D. N. Basov, “Infrared perspective on Fermi surface reconstruction in magnetic field”, in preparation.

J. M. Tranquada, D. N. Basov, A. D. LaForge, and A. A. Schafgans, “Stripes, quantum oscillations, and superconducting fluctuations”, submitted to Physical Review Letters.

A. A. Schafgans, A. D. LaForge, S. V. Dordevic, M. M. Qazilbash, W. J. Padilla, K. S. Burch, Z. Q. Li, Seiki Komiya, Yoichi Ando, and D. N. Basov, “Towards two-dimensional superconductivity in $La_{2-x}Sr_xCuO_2$ in a moderate magnetic field”, submitted to Physical Review Letters.

A. D. LaForge, W. J. Padilla, K. S. Burch, Z. Q. Li, A. A. Schafgans, Kouji Segawa, Yoichi Ando, and D. N. Basov, “Magnetic field induced modification of superfluid density and interplane spectral weight in $YBa_2Cu_3O_y$”, Physical Review B 79, 104516 (2009).

C. C. Homes, S. V. Dordevic, A. Gozar, G. Blumberg, T. Rm, D. Hvonen, U. Nagel, A. D. LaForge, D. N. Basov, and H. Kageyama, “Infrared spectra of the low-dimensional quantum magnet $SrCu_2(BO_3)_2$: Measurements and ab initio calculations”, Physical Review B 79, 125101 (2009).

A. D. LaForge, W. J. Padilla, K. S. Burch, Z. Q. Li, A. A. Schafgans, Kouji Segawa, Yoichi Ando, and D. N. Basov, “Sum Rules and Interlayer Infrared Response of the High Temperature $YBa_2Cu_3O_y$ Superconductor in an External Magnetic Field”, Physical Review Letters 101, 097008 (2008).

D. Talbayev, A. D. LaForge, S. A. Trugman, N. Hur, A. J. Taylor, R. D. Averitt, and D. N. Basov, "Magnetic Exchange Interaction between Rare-Earth and Mn Ions in Multiferroic Hexagonal Manganites", Physical Review Letters 101, 247601 (2008).

A. D. LaForge, W. J. Padilla, K. S. Burch, Z. Q. Li, S. V. Dordevic, Kouji Segawa, Yoichi Ando, and D. N. Basov, "Interlayer electrodynamics and unconventional vortex state in $YBa_2Cu_3O_y$", Physical Review B 76, 054524 (2007).

ABSTRACT OF THE DISSERTATION

Probing Correlated Electron Matter with Infrared Magneto-Optics

by

Andrew David LaForge

Doctor of Philosophy in Physics

University of California, San Diego, 2009

Professor Dimitri N. Basov, Chair

This dissertation describes the characterization of complex electronic materials via infrared magneto-spectroscopy. It primarily focuses on the interplane electrodynamics of the high-transition-temperature cuprate superconductors, but is extended to include semiconductors and semimetals. Due to the complex interconnection between superconductivity and magnetism, the magnetic field provides an ideal method for tuning the phase coherence of the superconducting order parameter. One component of this work examines the low-frequency response of the cuprates in the vortex state and critically assesses several theoretical descriptions of the vortex lattice dynamics. A detailed sum rule analysis in magnetic field illuminates the role of phase coherence and kinetic energy change in the formation of the superconducting condensate. The magneto-optical data for a range of cuprates are then discussed in the context of recent magneto-oscillation measurements, addressing the plausibility of coherent antinodal quasiparticle pockets on the Fermi surface. Finally, an infrared study of the proposed topological insulator Bi_2Se_3 utilizes a novel experimental apparatus to uncover dramatic spectral weight redistribution and electron-phonon coupling in this highly thermoelectric material.

Chapter 1

Introduction

Infrared/optical spectroscopy is a powerful and versatile tool for studying condensed matter systems. It is useful for interrogating the excitation spectra of materials on vastly disparate energy scales with both local specificity and broad integrability, benefitting from sensitive resolution of subtle spectral characteristics, but also the utilization of data from a wide frequency range to determine system properties based on conservation laws. Spectroscopy is at its most insightful when paired with a method of perturbation which allows the response of a system to be measured while traversing a region of the phase diagram. Such a perturbation may be realized through doping, temperature, pressure, or magnetic field, for example, and can drive the system into new states or modify the energy landscape altogether.

Magnetic field is a particularly functional tuning knob, as it can impact the electromagnetic response of a material in a reversible, precise way without introducing disorder. Furthermore, when the material of interest is a superconductor, the magnetic field competes with superconducting order parameter in a fundamental way, acting to break Cooper pairs as well as destroy phase coherence. Here we employ a newly refined, more accurate technique of infrared optics in magnetic field to probe previously inaccessible phenomena in correlated electron systems including the high-transition-temperature superconductors and candidate host materials for topological surface states.

In chapter 2 we report on the *c*-axis magneto-optical response of single crystals of the high-transition-temperature cuprate superconductor $\mathrm{YBa_2Cu_30}_y$

(YBCO), with magnetic fields oriented both parallel and perpendicular to the CuO_2 planes. For magnetic fields much smaller than the pairbreaking field, the field penetrates the material in finite lines of flux known as vortices, interrupting the superconducting phase coherence and forming vortex lattices with complex new phase relationships. Focusing on the $H \parallel CuO_2$ geometry, where the magnetic field initiates Josephson vortices, we contrast the field dependence of the low-frequency resonance behavior with that of two other cuprate materials, $La_{2-x}Sr_xCuO_4$ (LSCO) and $Bi_2Sr_2CaCu_2O_{8-\delta}$.

Chapter 3 discusses the role of c-axis magnetic field in the formation of the interplane superconducting condensate in YBCO. It has been known for some time that underdoped YBCO belongs to a class of cuprate superconductors in which the superfluid density (dissipationless spectral weight associated with superconducting carriers) is anomalously large compared to the spectral weight lost at low frequencies during the superconducting transition. This extra weight, inferred to originate from high-frequency regions of the spectrum, is associated with lowered electronic kinetic energy in the superconducting state. A sum rule analysis in magnetic field reveals that field suppresses the excess superfluid and returns it to high energies, eliminating the kinetic change.

In chapter 4 we extend the results of chapter 3 to the magnetic field configuration $H \parallel CuO_2$. For this geometry the kinetic energy change persists to the highest measured fields, highlighting the influence of phase conherence in the condensate formation. Additionally, the analysis is expanded to include data for intermediate temperatures within the superconducting state, where the weaker condensate is more susceptible to field.

Chapter 5 outlines the infrared perspective on magneto-oscillation studies of the cuprate superconductors. The recent discovery of quasiparticles with closed Fermi surfaces in underdoped cuprates has spurred the high-T_c community to explain the reciprocal-space origins of the coherent pockets. Here we utilize infrared conductivity measurements of YBCO and LSCO in magnetic field, in conjuction with angle-resolved photoemission spectroscopy and transport results, to address the plausibility of field-induced coherent electron pockets in the nodal and antinodal regions of k-space.

Lastly, chapter 6 presents infrared magneto-reflectance and -transmission measurements for the narrow-gap semiconductor Bi_2Se_3 which highlight new advances in accuracy and repeatability for the magneto-spectroscopy technique. Recent theoretical work has identified this material as a prime candidate for the realization of a topological insulator, an novel quantum state of matter characterized by robust metallic surface states and insulating bulk properties. We report on spectral weight transfer in magnetic field, as well as identify signatures of electron-phonon coupling.

Chapter 2

Interlayer electrodynamics and unconventional vortex state in $YBa_2Cu_3O_y$

Abstract

We report on the *c*-axis magneto-optical response of $YBa_2Cu_3O_y$ ($y = 6.65$ and 6.75) single crystals, with magnetic fields oriented both parallel and perpendicular to the CuO_2 planes. The dominant characteristic of the c-axis electrodynamics in the superconducting state, the Josephson plasma resonance (JPR), is remarkably sensitive to fairly modest magnetic fields below 8 T. Fields oriented perpendicular to the CuO_2 planes are shown to shift the edge of the JPR and also reduce the weight of the so-called "400-cm^{-1} mode", shedding light on this enigmatic feature. In the $H \parallel CuO_2$ geometry, where the magnetic field initiates Josephson vortices, we observed a strong mode in the far-infrared which hardens with increasing field. The field dependence of the low-frequency resonance behavior is contrasted to that of two other cuprate materials: $La_{2-x}SrCuO_4$ compounds that we have investigated earlier, and $Bi_2Sr_2CaCu_2O_{8-\delta}$. Specifically, there exist disparities in the number and field dependence of longitudinal modes measured for each system. Many of these differences can be explained through a new nu-

merical solution of the interlayer phase equations which includes effects of both in-plane and c-axis dissipation parameters. Support for this approach is given by calculations of the Josephson vortex lattice ground state configuration, and further insight is gained through the phenomenological framework of the transverse JPR model, as well as a classical model of vortex dynamics.

2.1 Introduction

Since the first synthesis of single crystal cuprate superconductors nearly two decades ago, there has been much interest in their interplane conductivity (1; 2). The coupling between the major structural subunits, the CuO_2 planes, has been shown to be of Josephson origin (3; 4; 5), and interplay has been observed between the phonon modes and the electronic background, both of which reveal complicated temperature dependence (6; 7; 8). The formation of the pseudogap in the c-axis electronic conductivity of underdoped crystals (9; 10; 11; 12; 13) (or of the superconducting gap in nearly optimally doped compounds (2)) and the local field effects involving the phonon modes (14) yield a rich variety of complex behaviors. Furthermore, observation of phenomena such as the change of kinetic energy below T_c (15; 16; 18; 19; 20; 17) may give insight into the mechanism of high-T_c superconductivity itself.

Both doping and temperature dependence of the interplane conductivity have been investigated in detail for several families of high-Tc cuprates (9; 12; 21; 19). There is an agreement on the gross trends (2), although the interpretation of several features, including the so-called “400-cm^{-1} resonance” seen only in bilayered materials, remains controversial (22; 12; 23)

There has been comparatively little work on the effect of magnetic field on the interlayer transport (24; 26; 25), with only two publications pertaining to the $YBa_2Cu_3O_y$ (YBCO) system (27; 28), which is otherwise one of the most studied high-T_c superconductors. This scarcity is an indicator of the technical difficulty of these experiments rather than their importance. Magnetic field constitutes an efficient tuning “knob;” the field can be used to impact the superfluid density more gently than temperature and, unlike doping, this tuning is reversible and does not change the level of disorder in the system. In this article we exploit the influence of magnetic field to better understand the origin of several characteristics of the vortex state as well as of the anomalies of the *c*-axis response.

For field magnitudes between the lower and upper critical fields, field lines enter a type-II superconductor in tubes of quantized flux known as vortices. The vortex state, particularly that of the high-T_c cuprates, presents a complex phase diagram characterized by varying degrees of structural order, pinning, and flux flow, among other properties (29; 30). The current theoretical descriptions of the vortex state have been successful at explaining, and at times even predicting, the phenomena observed in transport and thermodynamic experiments (31; 32; 33). The results of infrared and microwave measurements as a whole, however, have not been so easily accounted for; as we will show in this article, the data collected for the canonical cuprate families (27; 25; 34) reveal distinct electromagnetic responses which have thus far not yielded to description under a single theoretical picture. Here conductivity data for the underdoped YBCO system will be presented and compared with previous experimental results in light of several theoretical perspectives. Section II will describe the magneto-optical experiment carried out at University of Califonia, San Diego. We will present temperature and field dependence of both the reflectance data and the optical constants obtained from them. In Sec. III we will introduce a progression of theoretical models relevant to the interplane electrodynamics, including the vortex dynamical model of Tachiki, Koyama, and Takahashi (TKT) (36), the bilayer model by van der Marel and Tvetskov (vdMT) (35), vortex lattice ground state calculations by Nonomura and Hu (48), and a numerical solution of the interlayer phase equations by Koshelev (49; 47). We singled out Refs. (36), (35), and (47) out of many other models constructed to describe the vortex dynamics (37; 38; 39; 40) because the TKT, vdM/T, and Koshelev scenarios explicitly consider the frequency dependence of the optical constants in the vortex state. The vortex lattice calculations by Nonomura and Hu (48) and Koshelev (49) define the regimes in which these models are applicable. Each perspective contributes to the understanding of this problem, but we will show that dissimilar features of the Josephson vortex electrodynamics can best be reconciled by considering the role of both in-plane and c-axis dissipation following the recent theoretical treatment by Koshelev (47).

2.2 Magneto-optical experiment

2.2.1 Raw reflectance data

The single crystals of YBCO under study in this work were grown using the flux method and annealed to oxygen contents of $y = 6.65$ and 6.75. Transport measurements, reported elsewhere (41), show that these crystals are of high purity, and sharp transitions to the superconducting state occur at $T_c = 60$ K and 65 K, respectively. One large crystal (ac-face area $= 2 \times 5$ mm^2) was used for each zero-field characterization, while for magneto-optical measurements 3–4 smaller smaller samples were assembled to form 3×6 mm^2 mosaics. Samples were approximately 3 mm thick. For each doping, all samples studied were grown and annealed in the same batch.

Experimental data were collected in a two-step process. Zero-field absolute reflectance $R(\omega)$ was first obtained at near-normal incidence over a broad range of frequency ($18-48000$ cm^{-1}) and temperature ($8-295$ K). In order to minimize the effects of finite sample size the reference data were taken using a technique where a sample is coated in-situ with Au (42). Field induced changes of reflectance were then recorded as the ratio $R(T, H)/R(T, 0\text{ T})$ for magnetic fields H up to 8 T applied both parallel and perpendicular to the CuO$_2$ plane. Although the system has been characterized to be stable over changing fields, reference spectra were also collected in field using an aluminum mirror (43). In all measurements the electric field was linearly polarized along the c axis of the crystal.

Zero-field reflectance $R(\omega)$ at several temperatures is displayed in Fig. 2.1(a) for $y = 6.67$ and Fig. 2.2(a) for $y = 6.75$. At $T = 295$ K the reflectivity is flat in the far infrared with an upturn toward $R = 1$ as $\omega \to 0$. The rich structure above $\omega = 100$ cm^{-1} due to a series of transverse optical phonons is followed by nearly featureless mid-infrared response. As the temperature is lowered from room temperature to T_c the far-infrared reflectance shifts to lower values, indicating that the system is becoming less conducting in the c direction. A broad feature near $\omega = 450$ cm^{-1} appears at temperatures as high as 150 K and grows dramatically with further cooling. Below T_c a distinct change is seen in the low-frequency spectra; here we observe a sharp plasma edge at $\omega = \omega_B$, below which reflectance is nearly unity. This feature is a signature of the Josephson plasma resonance (JPR), a coherent interplane oscillation of Cooper pairs. This plasma edge grows sharper and moves to higher energy as the superconducting condensate is stiffened at lower temperatures. These results are consistent with earlier studies of similar dopings (9; 12).

Application of an external magnetic field in either orientation with respect to the CuO_2 plane produces dramatic changes in reflectance. For measurements made with $H \,||\, CuO_2$, shown in Figs. 1(b) and 2(b), a new absorption feature is observed at frequencies ω_A below the JPR edge. This dip in $R(\omega)$ (first appearing at $\omega_A = 40$ cm^{-1} for $y = 6.75$ at $H = 4$ T) deepens and moves to higher energies with increasing field. This agrees with optical studies of $YB_2Cu_3O_{6.60}$ in magnetic field (27). Several contrasts between dopings are observed, however. The present $H \,||\, CuO_2$ spectra for the $y = 6.75$ crystal do not exhibit the decrease of the JPR edge frequency ω_B seen for the $y = 6.60$ and 6.67 dopings. Also, the data reported in this work show no enhancement of the "400 cm^{-1}" resonance, as was seen in the prior data for $y = 6.60$ (27). In fact, no new absorptions appear at frequencies higher than 100 cm^{-1}, and the only modifications to the spectra involve minute shifts of phonon peak frequencies. In the $H \,||\, c$ geometry, an entirely different behavior is seen [see Figs. 1(c) and 2(c)] . There is no evidence of a new resonance in the low-frequency absorption; instead the JPR edge softens and broadens. The higher energy behavior is also clearly dissimilar between the two experiments, as only the $H \,||\, c$ reflectance exhibits a suppression of the "400 cm^{-1} feature." The differences between the various spectra are highlighted by the field ratios $R(H)/R(H = 0)$ in the insets to Figs. 1(b), 1(c), 2(b) and 2(c). For both $H \,||\, CuO_2$ and $H \,||\, c$ geometries field induced changes of reflectance became weaker and broader as the temperature was increased to T_c, and in the pseudogap

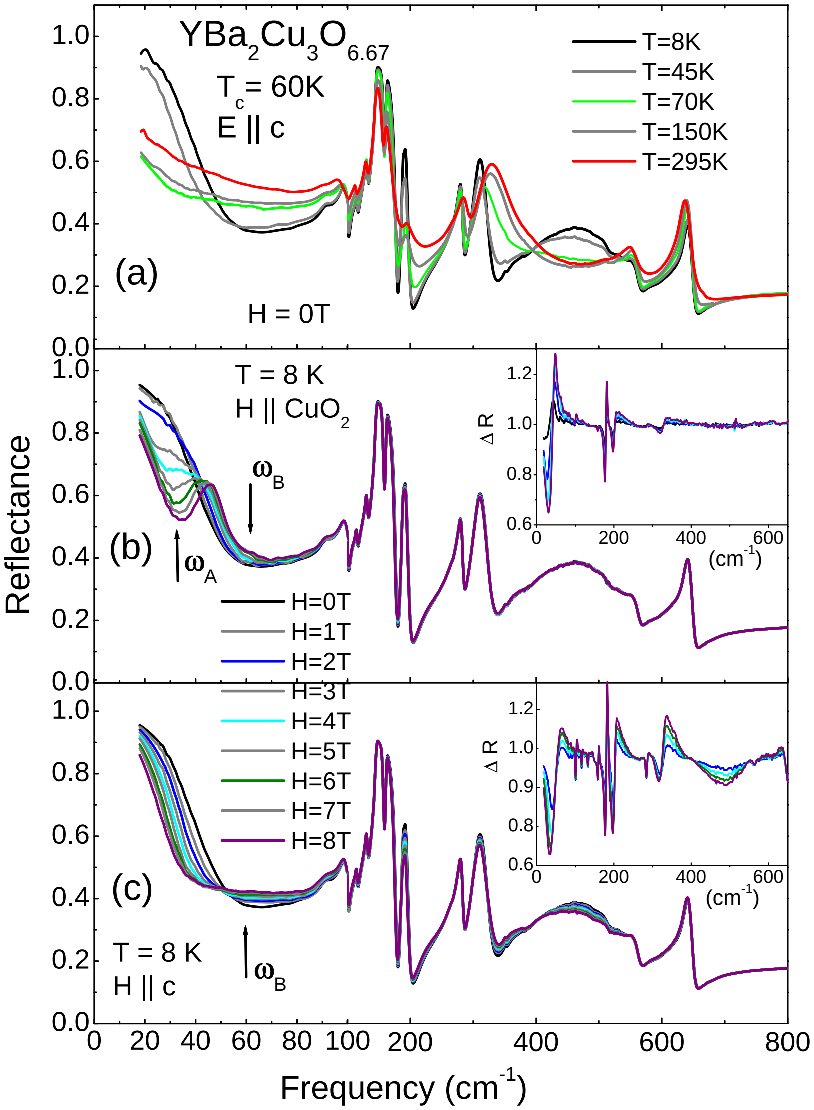

Figure 2.1: Infrared reflectance $R(\omega)$ of $YBa_2Cu_3O_{6.67}$ single crystal for (a) several temperatures above and below T_c and at 8 K for magnetic fields oriented (b) parallel to the CuO_2 planes and c) parallel to the c axis . Below T_c the sharp reflectance edge characteristic of the Josephson plasma resonance (JPR) is evident. Fields applied parallel to the CuO_2 planes produce a new resonance feature below the plasma edge which shifts upward with increasing field, while c-axis fields shift the JPR to lower energies. The “400 cm^{-1}” mode, which appears above T_c, is clearly modified by c-axis, but not in-plane, magnetic fields. Inset: Field ratios $\Delta R = R(8\ \mathrm{K}, H\ \mathrm{T})/R(8\ \mathrm{K}, 0\ \mathrm{T})$.

state above T_c no field induced changes were observed within the signal-to-noise of our experiment.

2.2.2 c-axis optical conductivity, loss function, and superfluid density

Reflectance data were transformed via the Kramers-Kronig (KK) relations to produce the complex conductivity $\hat{\sigma}(\omega) = \sigma_1(\omega) + i\sigma_2(\omega)$ and complex dielectric function $\hat{\varepsilon}(\omega) = \varepsilon_1(\omega) + i\varepsilon_2(\omega)$. We have verified that the extrapolations required for the KK analysis do not affect the conductivity spectra within the range where actual data exist. Generally, the conventional form of the KK integrals is not suitable for reflectance data collected in magnetic field due to the emergence of nondiagonal components in the conductivity tensor (44). In a metal these contributions are governed by the cyclotron frequency $\omega_c = eH/m^*c$, where H is the applied magnetic field and m^* is the electronic effective mass. Since the effective masses relevant to both the intraplane and particularly interplane response of cuprates are large (45), the use of the conventional KK relations would be justified. In a superconductor, however, the relevant parameter is the hall angle, which has been shown to be small both in the plane and along the c axis of YBCO (46).

The dissipative part of the conductivity, $\sigma_1(\omega)$, is shown in Figs. 3 and 4. At room temperature $\sigma_1(\omega)$ is characterized by a series of infrared active phonons superimposed upon a nearly flat electronic background. The zero-field conductivities, displayed in Figs. 3(a) and 4(a), show that both the phonon structure and electronic background are temperature dependent, with two major effects taking place. First is the emergence of the pseudogap, a partial suppression of low-frequency conductivity common in underdoped cuprates. Also important is the shift in spectral weight from the high-frequency tail of the 320 cm^{-1} phonon to the asymmetrical mode at 450–500 cm^{-1} (8). Note that this shift begins at temperatures as high as 150 K, far above T_c. This mode, which appears in a variety of bilayered cuprates, has been attributed to a Josephson transverse mode (35), and alternatively to bilayer splitting (23). Note that the overall conductivity levels are

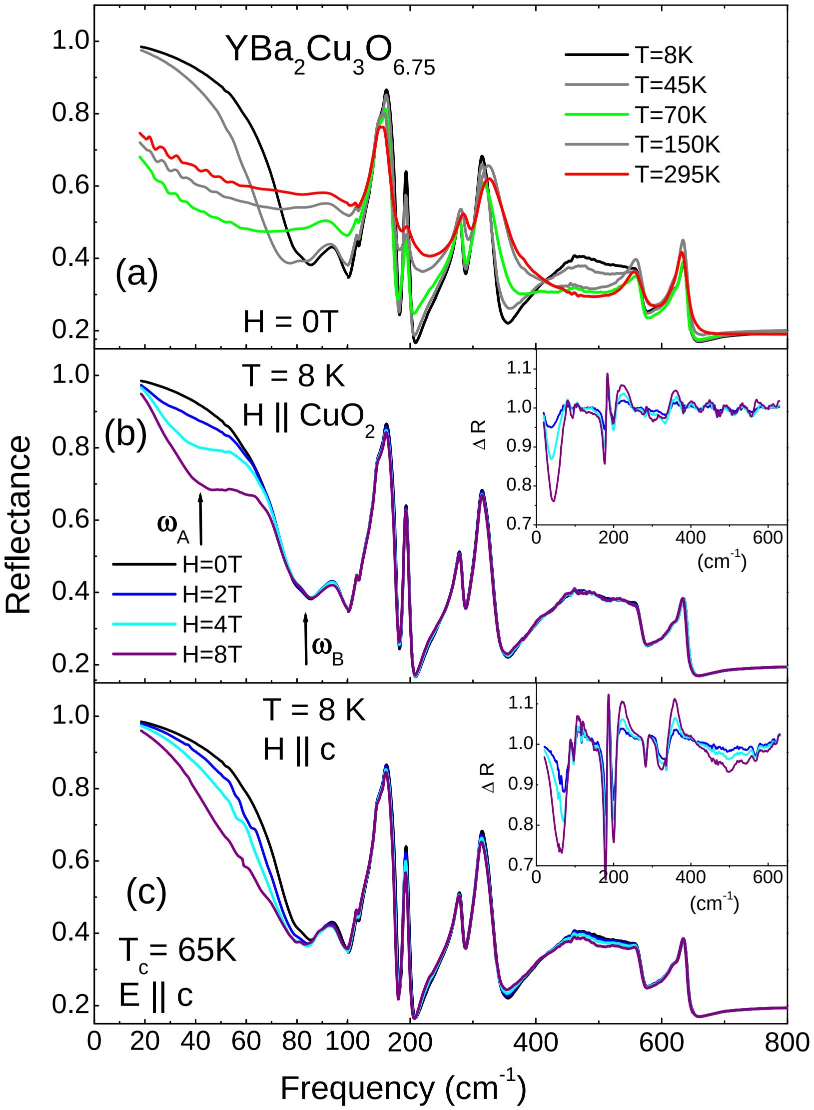

Figure 2.2: Infrared reflectance $R(\omega)$ of $YBa_2Cu_3O_{6.75}$ single crystal. See caption of Fig. 1 for details.

higher for $y = 6.75$ than for $y = 6.67$, and that the assymmetrical mode occurs at a higher frequency.

Similar to the raw reflectance data, the optical conductivity displays dramatically different behavior between the two field orientations studied. For $H \parallel \mathrm{CuO}_2$, shown in Figs. 3(b) and 4(b), the low frequency dip seen in the reflectance spectra is manifested in $\sigma_1(\omega)$ as a resonance whose strength and center frequency depend on magnetic field. In contrast, the $H \parallel c$ conductivity changes very little in the low-frequency region [see Figs. 3(c) and 4(c)]. The contribution due to the electronic background increases monotonically with field, and only a broad absorption is seen. Significant field-induced changes do appear at higher energies, however, as the "400 cm^{-1}" mode is systematically suppressed with $H \parallel c$. Spectral weight is transferred back into the edge of the 320 cm^{-1} phonon, reversing the effects of lowering temperature.

Further insight into the field dependence of the JPR can be gained by examining the loss function Im[-1/$\varepsilon(\omega)$], shown in Figs. 5 and 6. Peaks in the loss function occur at possible zero crossings of $\varepsilon_1(\omega)$, identifying the screened frequency position of longitudinal plasma oscillations. The low-frequency loss function spectra in Figs. 5(a) and 6(a) are mainly featureless at temperatures above the superconducting transition, but below T_c they exhibit a resonance at $\omega_B = 50$ (77) cm^{-1} which corresponds to the longitudinal JPR in the $y = 6.67$ (6.75) sample. As the field applied parallel to the planes is increased a new peak develops at a lower frequency $\omega_A = 30$ (40) cm^{-1} [see Figs. 5(b) and 6(b)]. In the more underdoped sample the main loss function peak hardens by 5 cm^{-1} by 4 T, but does not change as field is increased to 8 T. At the higher doping the main peak frequency is field independent. This additional mode does not appear for $H \parallel c$ in Figs. 5(c) and 6(c); rather, the original peak at ω_B is shifted to lower energies, reflecting the suppression of the JPR.

We will now show that the dominant effect underlying the trends in the optical conductivity seen above is a destruction of the superconducting condensate by magnetic field. The electronic response of a superconducting material can be quantified within a two-fluid framework in which the optical conductivity has the

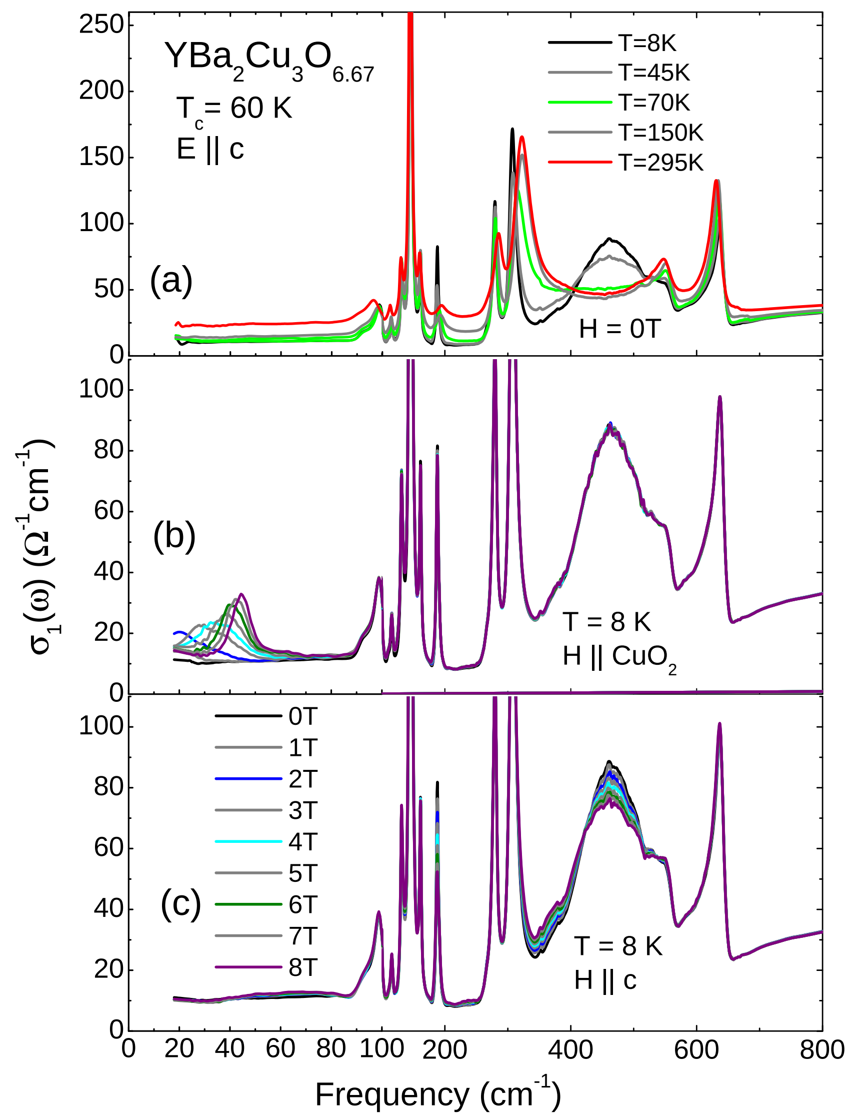

Figure 2.3: Optical conductivity of $YBa_2Cu_3O_{6.67}$ for (a) several temperatures and at 8 K for magnetic fields oriented (b) parallel to the CuO_2 planes and (c) parallel to the *c* axis . Similar to $R(\omega)$, the new low-frequency resonance is only seen for in-plane fields. Fields applied along the *c* axis reverse the effect of lowering temperature by weakening the "400-cm^{-1}" mode and restoring spectral weight to the 320 cm^{-1} phonon.

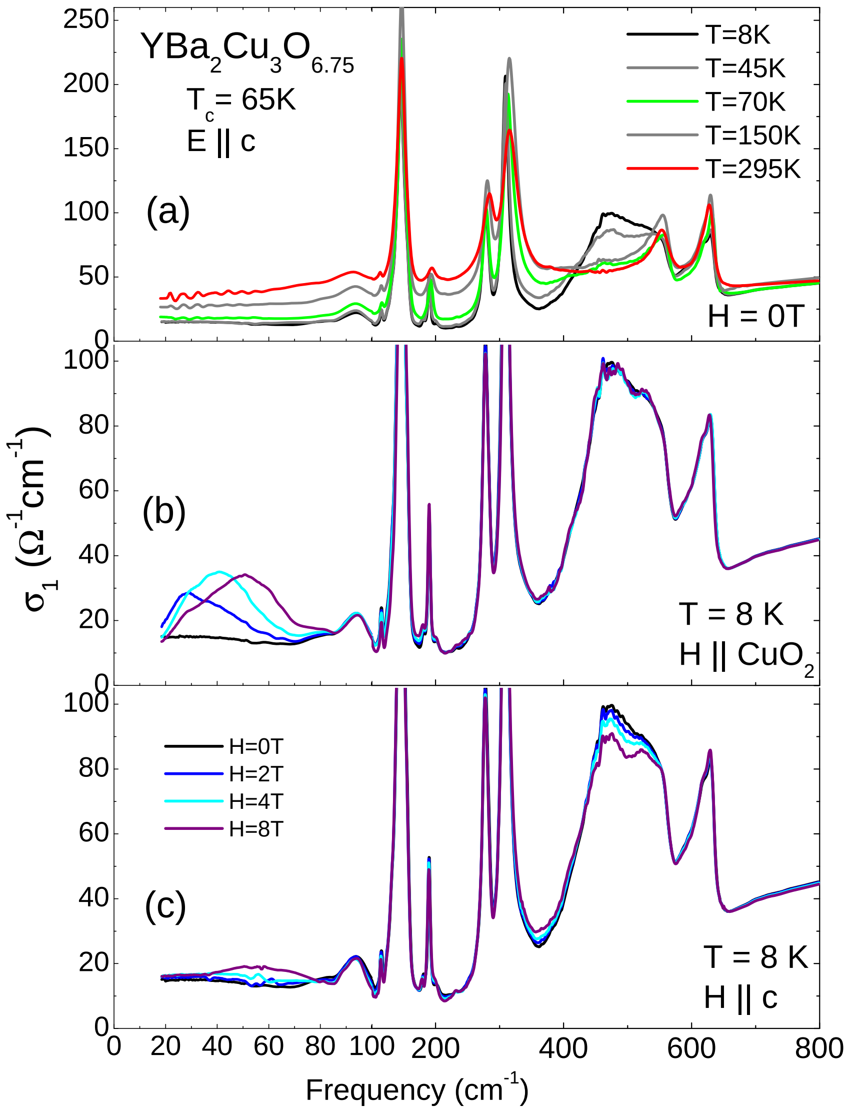

Figure 2.4: Optical conductivity $\sigma_1(\omega)$ of $YBa_2Cu_3O_{6.75}$ single crystal. See caption of Fig. 2.3 for details.

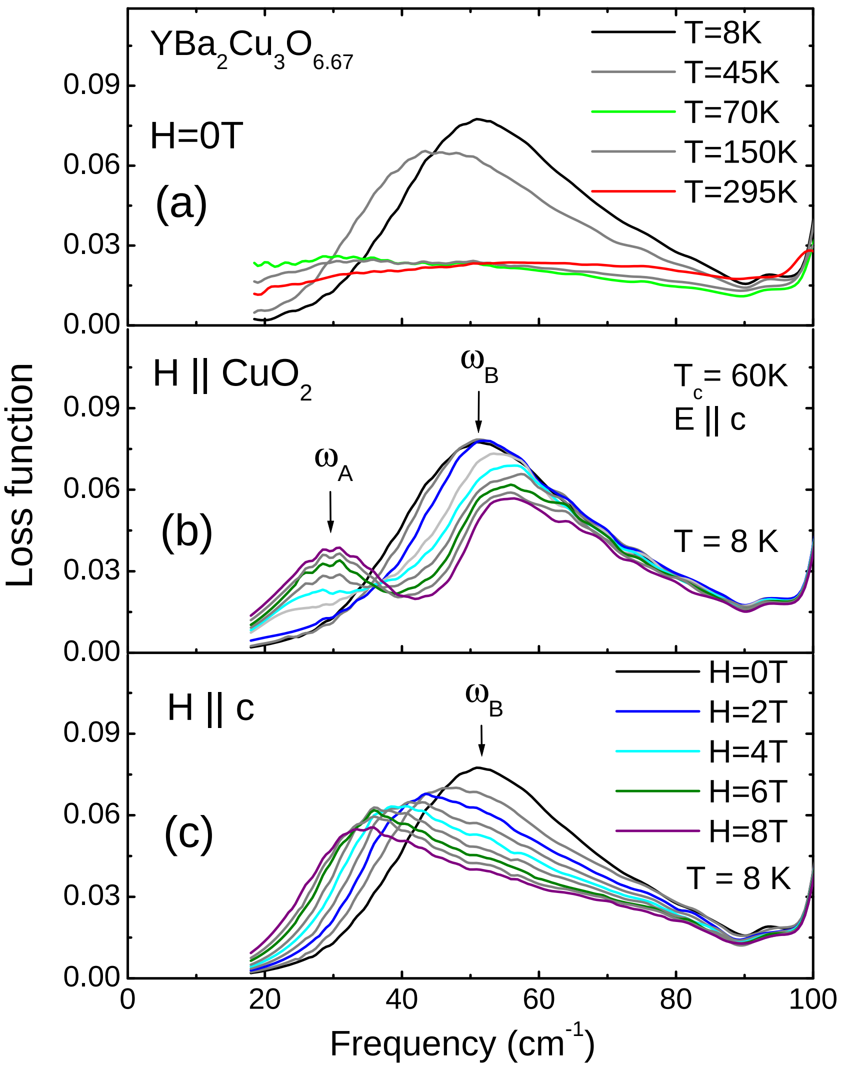

Figure 2.5: Loss function for $YBa_2Cu_3O_{6.67}$ for (a) several temperatures above and below T_c and at 8 K for magnetic fields oriented (b) parallel to the CuO_2 planes and (c) parallel to the c axis. Peaks in the loss function generally identify electromagnetically active ionic motions along the c axis, such as longitudinal plasma oscillations and phonons. In the normal state, phonon peaks can be identified above 90 cm^{-1}. Below T_c a strong new peak at $\omega_B = 50$ cm^{-1} indicates the presence of the Josephson plasma resonance (JPR). A second peak emerges near $\omega_A = 30$ cm^{-1} in fields parallel to the CuO_2 planes, and the JPR peak broadens and weakens for fields parallel to the c axis.

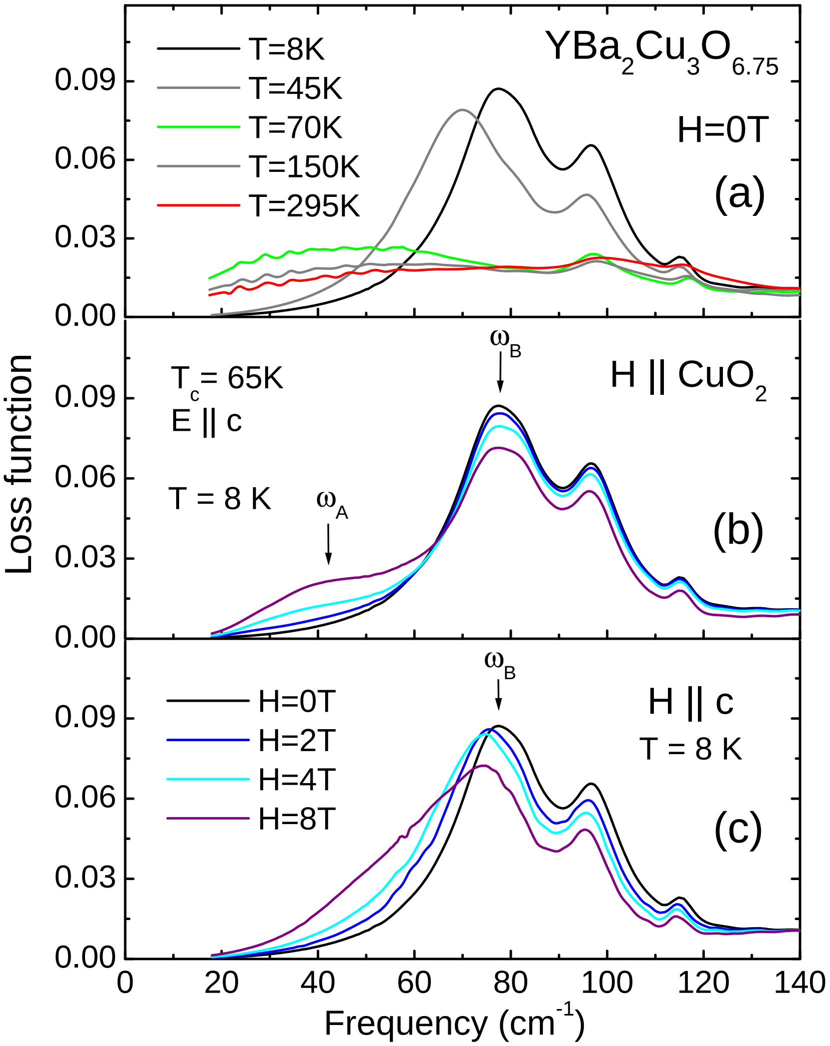

Figure 2.6: Loss function for $YBa_2Cu_3O_{6.75}$ single crystal. See caption of Fig. 2.5 for details.

form $\sigma_1(\omega) = \rho_s \delta(\omega) + \sigma_1^{\text{reg}}(\omega)$. The first term stands for the contribution of the superconducting condensate, which has the form of a zero-frequency delta function whose weight is the superfluid density $\rho_s = \pi e^2 n_s / 2m^*$. Here n_s is the superconducting carrier density and m^* is the pair effective mass. The latter term is the regular, finite-frequency contribution $\sigma_1^{\text{reg}}(\omega)$ due to unpaired carriers and pinned vortex modes, among other sources. The δ function cannot be directly observed in the $\sigma_1(\omega)$ spectra, but its influence can be deduced by examining $\sigma_2(\omega)$. This virtue of imaginary conductivity is due to Kramers-Kronig relations implying that the δ function in $\sigma_1(\omega)$ must be matched with a $1/\omega$ dependence in $\sigma_2(\omega)$. The net outcome of the condensate formation is the following expression for the imaginary conductivity:

$$\sigma_2(\omega) = \frac{\rho_s}{\pi\omega} + \sigma_2^{\text{reg}}(\omega). \tag{2.1}$$

Similar to the real conductivity, the spectra of $\sigma_2(\omega)$ inferred from KK analysis of the data also contain a contribution due to unpaired carriers and pinned vortex modes in addition to the superfluid term. Therefore, in order to extract accurate values of the superfluid density from the conductivity data it is imperative to correct the results of the KK analysis for this regular contribution $\sigma_2^{\text{reg}}(\omega)$ (5). Equation 2.1 can then be solved for the corrected superfluid density $\rho_s = \pi\omega[\sigma_2(\omega) - \sigma_2^{\text{reg}}(\omega)]$, which is plotted for $YBa_2Cu_3O_{6.75}$ in Fig. 2.7 for $H = 0 - 8$ T and several temperatures below T_c. As emphasized by the 3D nature of the graph, the increases of temperature and field share the common aspect of suppressing ρ_s, but with disparate power law dependencies. Different power laws are also observed between the two field geometries; although ρ_s is suppressed by 50% at $8T$ in both cases, the field dependence of ρ_s in the $H \mid\mid CuO_2$ orientation [Fig. 2.7(a)] has a concave curvature whereas the $H \mid\mid c$ suppression [Fig. 2.7(b)] is nearly linear in field. The crystal with $y = 6.67$ (not shown) exhibited similar trends of suppression of superfluid, but with smaller magnitudes.

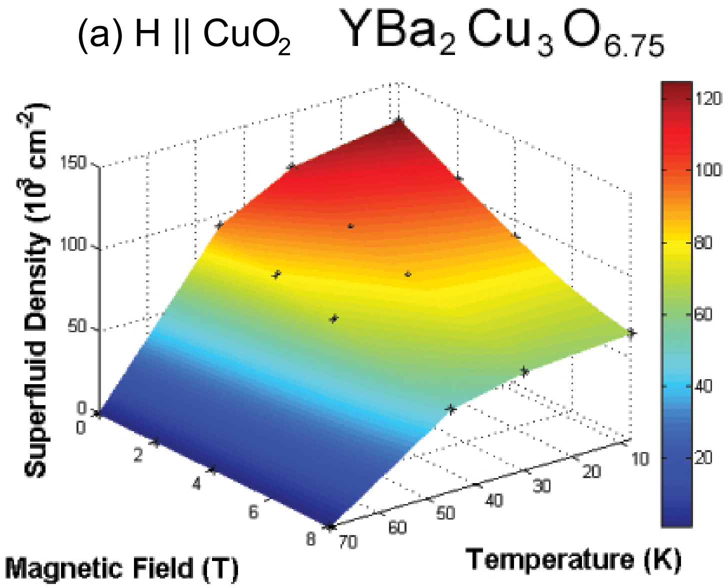

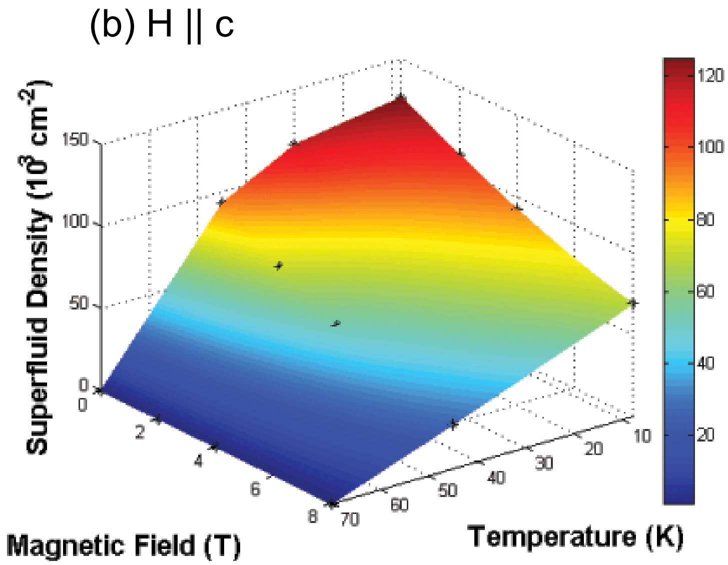

Figure 2.7: Superfluid density ρ_s for YBa$_2$Cu$_3$O$_{6.75}$, determined by σ_2 analysis with correction for regular contribution, as a function of temperature and magnetic field. Although both plots show suppression of superfluid density with field, the parallel field orientation (a) produces a concave curvature, while the perpedicular field dependence (b) is nearly linear.

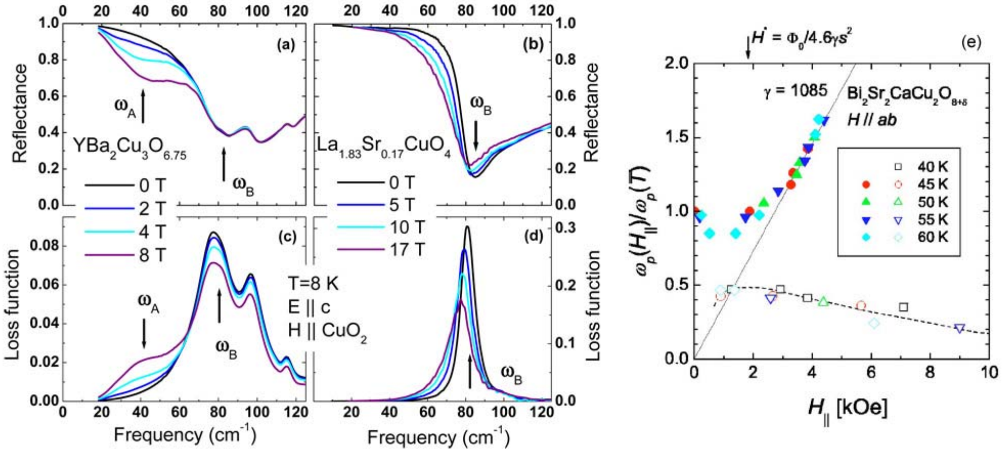

Figure 2.8: Comparison of electrodynamic response data for various families of cuprate superconductors. Raw reflectance spectra reveal a resonance feature below the Josephson plasma edge for YBCO (a) but not La214 (b). The loss function spectra show two longitudinal resonance modes for YBCO (c), but only one for La214 (d). A frequency-field phase diagram for Bi2212 (e) from ref. (65) displays two magnetoabsorption modes.

2.2.3 Comparison to other cuprate superconductors

To place into context the electrodynamic response of the $\mathrm{YBa_2Cu_3O}_y$ compounds described above, it is useful to make a comparison to two other cuprate superconductors, $\mathrm{La}_{2-x}\mathrm{Sr}_x\mathrm{CuO}_4$ (La214) and $\mathrm{Bi_2Sr_2CaCu_2O}_{8+d}$ (Bi2212). We will show that despite the common structural characteristics of these compounds, their Josephson vortex state electrodynamics exhibit striking differences. Consider, for example, the c-axis optical properties of La214 crystals under magnetic field applied parallel to the $\mathrm{CuO_2}$ planes. The reflectance, shown in Fig. 2.8(b), shows no sign of the structure at $\omega = \omega_A$ seen in YBCO. Rather, the JPR frequency ω_B softens and the entire plasmon structure is weakened. Stark differences also appear in the low frequency optical conductivity, plotted above in Figs. 3(b) and 4(c) for YBCO and published elsewhere for La214 (57). In contrast to the behavior observed for YBCO, $\sigma_1(\omega)$ increases broadly with field for La214, with no formation of a sharp transverse resonance.

In the Bi2212 system the larger anisotropy lowers the JPR frequency to a range inaccessible to infrared spectroscopy; microwave magnetoabsorption techniques are used instead (65). Since the latter method identifies longitudinal modes, the features it reveals can be most directly compared to the loss function in the above IR results. The work in ref. (65) focused on an underdoped crystal with transition temperature $T_c = 70$ K, but all trends were observed at optimal doping as well. The frequency-field diagram for Bi2212 in Fig. 2.8(e) displays two resonances: one appears only at higher temperatures and hardens linearly with parallel field as a dense vortex lattice is formed (39); the other resonance, visible at low temperature and nonzero fields, softens with magnetic field. This result differs distinctly from that of the other systems; La214 supports only one sharp longitudinal mode, and its peak frequency ω_B decreases with field [see Fig. 2.8(d)]. As mentioned above, in YBCO the JPR peak frequency ω_B is field independent or weakly increasing, and the linewidth is broader [see Fig. 2.8(c)]. Furthermore, both modes in YBCO are sharpest at low temperature, with no evidence of the additional temperature scale seen in Bi2212. The closest agreement between the data sets is in the lower-frequency modes of YBCO (labeled as ω_A) and Bi2212. Both are too weak to be resolved at the lowest fields and have little frequency dependence in modest fields. At the outset, the electromagnetic responses of the three systems appear to be quite distinct and without a common pattern; thus, the task of finding a universal explanation has not been straightforward (66; 67; 68; 69).

2.3 Theoretical models

Many theoretical models have been proposed to explain the low-frequency infrared and microwave properties of the layered high-T_c superconductors. Earlier theories (37; 38; 40) have accurately described elements of the experimental data for individual families of cuprates but have not sufficiently accounted for the differences in resonance behaviors from family to family displayed in Fig. 2.8. Discussion below outlines a series of developments which form a coherent explanation of these disparities. All models discussed give predictions for the frequency dependence of the optical conductivity. In Sec. III A, a classical description of

Josephson vortex oscillation presented by Tachiki, Koyama, and Takahashi (TKT) (36) marks a good starting point for approaching this problem. Here the interlayer phase equations are solved analytically for small fields. A different perspective is gained in Sec. III B with the phenomenological model of van der Marel and Tsvetkov (35; 95), which considers the modification of the JPR behavior in a multilayer system. The parameter space where this model is applicable is specified in detail by calculations of the Josephson vortex lattice ground state, computed by Nonomura and Hu (48), as well as Koshelev (49), and discussed in Sec. III C. This knowledge of the ground state configuration has been integrated into new numerical solutions of the interlayer phase equations which take into account the in-plane and *c*-axis dissipations. This approach by Koshelev (47) is described in Sec. III D.

2.3.1 Vortex oscillation model

Any microscopic derivation of the electrodynamic properties of a coupled Josephson system must begin with the interlayer phase equations (50; 51), and it is instructive to first consider their analytical solution. With this objective, we have found many of the features of the low-frequency resonance mode to be in qualitative, and perhaps even quantitative, agreement with predictions of the vortex dynamics model of TKT (36). This theory has been applied to explain changes in superfluid density and plasma edge position in LSCO (25; 24) but the present work is the first to employ it to fit a finite-frequency mode in the conductivity data. The TKT model offers descriptions of the low frequency electromagnetic response of cuprate superconductors for magnetic fields oriented both parallel and perpendicular to the CuO_2 planes, taking into account the difference in vortex structure between the two geometries. For the case of magnetic fields oriented parallel to the *c* axis, the flux penetrates the material by forming pancake vortices which order in an Abrikosov lattice in the *ab* plane (29). According to the TKT model, since the *c*-axis plasma induced by the applied electric field does not couple to these pancake vortices, the primary effect of the field on the low-frequency optics is quasiparticle scattering inside the normal vortex core and the change in dielectric function this engenders. The normal and superconducting areas of the *ab* plane are modeled with oscillators with and without damping, respectively, and the total dielectric function is a weighted average of the two regions. Thus, for low temperatures, we have

$$\varepsilon\left(\omega\right)=\varepsilon_c-\frac{\omega_p^2}{\omega(\omega+i0^+)}\left[1-\frac{H}{H_{c2}}\right]-\frac{\omega_p^2}{\omega(\omega+i\gamma)}\left[\frac{H}{H_{c2}}\right], \tag{2.2}$$

where H is the applied magnetic field, H_{c2} is the thermodynamic upper critical field, γ is the quasiparticle scattering rate in the normal region, and ω_p is proportional to the total number of carriers.

Fields applied paralled to the *ab* plane, however, will create Josephson vortices with cores pinned in the normal regions between CuO_2 planes and current patterns sustained by Josephson tunneling. Here the vortex dynamics play an important role, and the equation of motion for a vortex oscillating with viscous damping constant η and mass M about a pinning site with Labusch constant κ_p is

$$M\ \ddot{u}+\eta\ \dot{u}+\kappa_p u=\frac{\Phi_0}{c}\vec{J}\times\hat{n},$$

where Φ_0 is the flux quantum, $\vec{J}$ is the current, and $\hat{n}$ is the unit vector along the vortex direction. Solving for the transverse dielectric function yields

$$\varepsilon(\omega)=\varepsilon-\frac{\frac{\omega_{ps}^2}{\omega^2}+\frac{\omega_{pn}^2}{\omega(\omega+i\gamma)}}{1+\frac{\phi_0}{4\pi\lambda_c^2}\frac{H}{\kappa_p-i\eta\omega-M\omega^2}}, \tag{2.3}$$

where $\omega_{ps}=\sqrt{c^2/\lambda_c^2}$ and ω_{pn} are the superconducting and normal state plasma frequencies, respectively, and λ_c is the *c*-axis penetration depth. Representative $R(\omega)$ and $\sigma_1\left(\omega\right)$ obtained from this model are shown in Fig. 2.9. Note that the dip in $R(\omega)$ and peak in $\sigma_1\left(\omega\right)$ appear only for the H || CuO_2 orientation, as was observed in the experimental data. The H || c spectra exhibit a shift in the frequency of the plasma edge in $R(\omega)$ and a monotonic increase of $\sigma_1\left(\omega\right)$, also corresponding to the data. One aspect of the H || c data not accounted for in the TKT theory is the broad absorption near 60 cm^{-1} at H = 8 T. This feature, different in appearance from the resonance seen for H || CuO_2, may be a result of the in-plane inhomogeneities produced by pancake vortices and their random fluctuations in the vortex liquid state (58; 57).

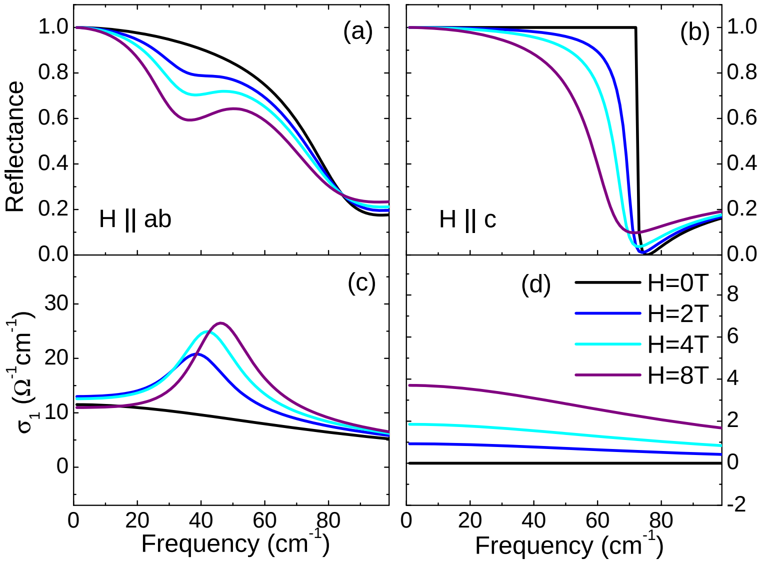

Figure 2.9: Theoretical model curves for c-axis reflectance and optical conductivity, as derived from the vortex dynamical model of Tachiki, Koyama, and Takahashi (Eqs. (2.2) and (2.3)). Here the penetration depth is adjusted with field to account for the suppression of superfluid density in field. Qualitative trends seen here mirror those seen in the experimental data in Figs. 1 and 2. For H || CuO_2, the low frequency resonance is visible in (a) the reflectance and (c) the optical conductivity. Such a feature is only produced for a large vortex mass. In the H || c orientation, the plasma edge in the reflectance (b) is shifted to lower energies with field. The normal vortex cores increase dissipation in $\sigma_1(\omega)$ (d).

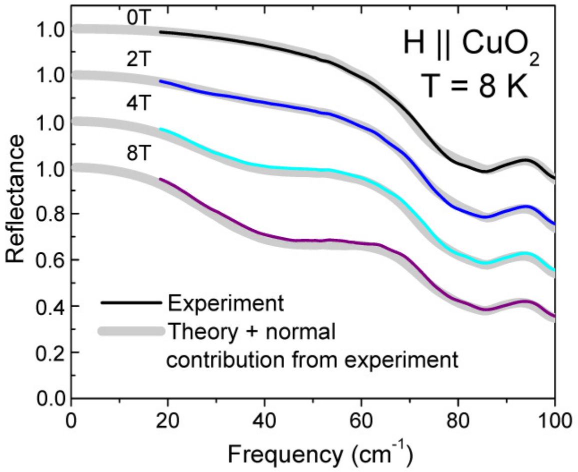

Figure 2.10: Theoretical fits (thick gray) to experimental reflectance data for $YBa_2Cu_3O_{6.75}$ at 8 K (thin colored) using vortex dynamical model of Tachiki, Koyama, and Takahashi. Several values of magnetic field applied parallel to the CuO_2 planes are shown. For these fits the normal contribution $\sigma_1^{\mathrm{reg}}(\omega)$ was added to the optical conductivity derived from the theory in order to account for phonons and electronic background. Fit parameters are listed in Table 2.1.

The TKT functional forms for $R(\omega)$ generated from Eqs. (2.2) and (2.3) were successfully fitted to the perpendicular and parallel field experimental data, respectively, for the $y = 6.75$ sample. In the $H \parallel c$ case we used the mean-field $H_{c2} = 41$ T obtained from magnetoresistance measurements (59) and fit for ω_p and γ. The theoretical agreement is closest for the lower fields, as the 8 T data shows a stronger suppression of the plasmon than theory predicts. For $H \parallel CuO_2$ the fitting was performed in the following way: first, zero-field $R(\omega)$ was fitted using λ_c and ω_p as free parameters. Next, in-field curves were iteratively fitted with κ_p and η, then λ_c, allowed to vary. A single value of M was acceptable for all fields. The regular (nonsuperconducting) components of $\sigma_1(\omega)$ and $\sigma_2(\omega)$ were added to the theoretical prediction to compensate for the presence of phonons and electronic background, which are not accounted for by the model.

When comparing the fit curves to the data in Fig. 2.7, remarkable agreement is observed in both field and frequency dependency of the resonance. Though not shown, the corresponding peak in $\sigma_1(\omega)$ is also reproduced. As seen in Table 2.1, best-fit values for $\lambda_c(8T)$ were within 20% of those measured experimentally, with better agreement at lower fields, and vortex dynamical parameters κ_p and η were within the range of those reported elsewhere (30). The exception was the vortex inertial mass, which was required to be much larger (factor of 10^4) than theoretically predicted for fields oriented parallel to the planes of a layered superconductor (60). Since there exists no widely accepted method for determining the vortex mass (61; 63; 62; 64), it is difficult to interpret the large value of the mass required to reproduce the experimental line shape.

The success of these fits should be tempered with some criticism. The TKT analysis depends sensitively on the dynamical parameters, which can only be corroborated with transport or microwave resonance experiments. It is unclear whether values obtained via these methods should be compatible with those inferred optically, so they were allowed to vary in the fitting. Thus, the fact that the vortex dynamical theory yields such an accurate fit to the data is hardly surprising, given the extra degrees of freedom allowed in the fit. A more fundamental issue is that the application of the TKT model to these systems relies on assumptions which may be invalid. First, the TKT model will produce a new field-induced resonance only if large effective mass is assigned to Josephson vortices. In related work in LSCO (25), vortex-induced suppression of superfluid density was explained through the TKT theory; as shown above no finite frequency feature was observed, and little or no mass was needed to produce a fit. Then within this framework one has to assume massive vortices in YBCO and much lighter ones in La214, an unlikely premise given the similarities in the zero-field response between the two systems, and the parameters upon which vortex mass is theorized to depend. Second, it is likely that the approximations for low frequencies and fields place the features under consideration outside of the physcially meaningful parameter space. Nonetheless, the TKT theory affords insight into the influence of the vortex dynamical parameters and provides a good theoretical starting point.

Table 2.1: Parameters used for fitting reflectance data with TKT theory, as shown in Fig. 2.7.

H (T)	0	2	4	8
λ_c^{obs} (μm)	4.42	4.80	5.26	6.16
λ_c^{fit} (μm)	4.14	4.14	4.42	4.85
$(\lambda_c^{obs} - \lambda_c^{fit})/\lambda_c^{obs}$	0.06	0.14	0.16	0.21
ω_p (cm^{-1})	386	358	324	271
κ ($\times 10^6$ Pa)	-	5.81	5.12	6.15
η ($\times 10^5$ Pa cm^{-1})	-	1.72	1.18	1.07
M (Pa cm^{-2})	-	3190	3190	3190

2.3.2 Transverse plasmon model

The van der Marel–Tvetskov (vdMT) model was developed specifically to describe the electrodynamics of multilayer superconductors (35). It predicts that in a system composed of layers with alternating Josephson coupling strengths the out-of-phase charge oscillations between layers will produce a transverse optical plasma resonance. A mode of this type is manifested as a resonance in the optical conductivity spectra. This theory was originally introduced as a possible explanation for the anomalously broad "400 cm^{-1}" resonance observed in underdoped bilayered cuprates (9; 95). The centrality of the compounds' bilayer nature is supported by the fact that the feature has not been observed in single-layer cuprates such as LSCO. However, when LSCO is doped with Sm a bilayer structure is created, and with it an transverse resonance near 12 cm^{-1}. Calculations based on frequency positions of the longitudinal plasmons within the constituent layers have been used to accurately track the position of the transverse plasmon through changes in temperature (52; 53) and field (54).

Following this progression, the theory has also been extended to the vortex state of YBCO under a magnetic field applied parallel to the $\mathrm{CuO_2}$ layers (27). The key assumption in this case is that vortices will penetrate only some of the layers, forming a quantized lattice along the c axis with a lattice parameter comensurate with the interlayer spacing (37). The differing couplings between junctions with and without vortices then define a vortex superstructure and a transverse resonance is produced. Although the pertinent resonance features in these three systems (YBCO intrinsic bilayer, $Sm_2O_2/(La, Sr)_2O_{2-\delta}$ superlattice, and YBCO vortex superstructure) occur over different energy scales and exhibit strikingly different temperature and magnetic field response, all have been explained using the fundamental idea of the transverse resonance (35).

In a derivation of the dielectric function due to a transverse plasmon (35), the bilayer system is modeled as a stack of superconducting layers with alternating Josephson coupling strengths and corresponding plasma frequencies ω_{pA} and ω_{pB}. By adding in series the impedances of the individual layers (rather than the conductivities, as is the case for parallel conduction channels) the dielectric function can be expressed in the form

$$\frac{\varepsilon(\omega)}{\varepsilon_\infty} = \frac{z_A\omega^2}{\omega(\omega+i\gamma_A)-\omega_{pA}^2} + \frac{z_B\omega^2}{\omega(\omega+i\gamma_B)-\omega_{pB}^2}, \tag{2.4}$$

where ε_∞ is the high-frequency dielectric constant, and ω_{pv} and γ_v are the screened Josephson plasma frequencies and damping constants which characterize each type of junction. The zeros of this function correspond to longitudinal plasma oscillations, which can be observed as peaks in the loss function Im[-1/$\varepsilon(\omega)$]. A pole in the dielectric function at $\omega_T = (z_A\omega^2 + z_B\omega^2)^{1/2}$ identifies a transverse plasmon and appears as a resonance peak in $\sigma_1(\omega)$. In the simplest form of the bilayer model, the weight factors z_v (constrained by $z_A + z_B = 1$) are determined solely by the volume fractions occupied by the layers, but the theory has been expanded to include the influence of electronic compressibility (55).

The transverse plasmon formalism has been applied to the present YBCO data for fields parallel to the CuO_2 planes, with all relevant parameters listed in Table 2.2. Examination of the loss function and conductivity spectra in Figs. 3–6 yields, for a fixed magnetic field, the longitudinal plasma frequencies ω_B and ω_A, corresponding respectively to JPRs in junctions with and without vortices, as well as the transverse plasma frequency ω_T. The proximity of a phonon peak at $\omega = 94$ cm^{-1} introduces at most a systematic error of 5% in ω_B for the more highly doped sample. From these frequency positions the weight factors z_A and z_B can be calculated. The high-frequency limit of the experimental $\varepsilon_1(\omega)$ is also taken directly from the data. The theoretical reflectivity corresponding to Eq. 2.4 was fitted to the $R(\omega)$ data, with the damping constants γ_v as the only free parameters.

As seen in Fig. 2.11, the fit matches well the shapes of $R(\omega)$ and $\sigma_1(\omega)$, and the theoretical integrated spectral weight of the tranverse mode S_T^{calc} is close to the observed value of S_T^{exp}. For example, for $y = 6.75$ we find $S_T^{\text{calc}} = 5.88 \times 10^4$ cm^{-2} and $S_T^{\text{exp}} = 5.93 \times 10^4$ cm^{-2}. Fits were obtained at 4–8 (8) T for the crystal with $y = 6.67$ (6.75); below these fields the frequency position of the lower longitudinal mode is not well defined, precluding similar quantitative analysis.

Provided the structural parameters of the bilayer crystal are known, then it is possible to calculate the electronic compressibility from the weight factors z_v (54; 56). In the case of a vortex superstructure, however, we have no separate measurement of the c-axis vortex lattice constant, and the effects of the changing lattice structure and compressiblity cannot be deconvoluted.

Table 2.2: Parameters used for fitting reflectivity with transverse plasmon model (Eq. 2.4). The only free parameters were γ_A and γ_B. All others were inferred from the experimental data in Figs. 2 and 3, as described in the text. The theoretical curves which utilize these parameters are displayed in Fig. 2.5.

	$y = 6.75$	$y = 6.67$				
H (T)	8	4	5	6	7	8
ω_A (cm^{-1})	40	30	30	30	30	30
ω_B (cm^{-1})	80	55	55	55	55	55
ω_T (cm^{-1})	52	34	39	40	42	45
z_A	0.23	0.12	0.29	0.34	0.41	0.53
z_B	0.77	0.88	0.71	0.66	0.59	0.47
γ_a (cm^{-1})	25	8.9	13	12	13	15
γ_b (cm^{-1})	39	32	25	24	23	19
$S_T^{\text{calc}}(10^3\text{cm}^{-2})$	58	40	40	39	37	35
$S_T^{\text{obs}}(10^3\text{cm}^{-2})$	59	37	38	38	38	37

The observed effects of magnetic field upon the 400 cm^{-1} mode are also in qualitative agreement with the transverse plasmon description. As detailed in the introduction to the vdMT theory, this mode has been described as a transverse plasmon arising from out of phase oscillation of the JPR and another, broader longitudinal mode at a higher frequency. Since the frequency position and spectral weight of the 400 cm^{-1} transverse mode (see Fig. 2.2) are dependent upon the positions of the longitudinal modes (see Fig. 2.3), one could expect to see correlations between these entities as they are altered by the field. Indeed, for the $y = 6.75$ sample any changes in the position of the loss function peak ω_B corresponding to the Josephson plasmon are linked to changes in the 400 cm^{-1} mode. For $H \,||\, \mathrm{CuO}_2$, ω_B and the 400 cm^{-1} mode are both not affected. When H is applied along the c axis, however, we observe a softening of ω_B, matched by a suppression of the 400 cm^{-1} mode. For the more underdoped sample, the hardening of the loss function mode at $\omega = \omega_B$ is not matched by a growth of the 400 cm^{-1} mode. This may suggest that both low frequency longitudinal modes are involved in the out-of-phase coupling which produces the broad transverse mode, and that the hardening of the mode at ω_B is balanced by the growth of the one at ω_A to maintain a constant "center of spectral weight."

This model yields a good fit to the present YBCO data with few free parameters, and has an excellent track record in describing far-infrared resonances in a variety of systems with multilayer geometries (28; 54). The strength and versatility of the approach stem from its phenomenological handling of the modification of interlayer Josephson couplings. When augmented with detailed calculations of the Josephson vortex superstructure (discussed below) the vdMT framework provides a qualitative account of differences between magneto-optics data in YBCO and La214 compounds.

2.3.3 Josephson vortex lattice ground state calculations

The effect of magnetic field upon a superconducting material depends on the relevant field scales for that particular system. Therefore, to analyze on the same footing the in-field JPR response of different families of cuprates it is imperative to turn to calculations of vortex lattice configuration which account for those scales. Recent studies by Koshelev (49) as well as Nonomura and Hu (48) have worked within the Lawrence-Doniach model. By minimizing the free energy functional they obtained the Josephson vortex lattice ground state. Here the critical field is defined as $H_{cr} = \Phi_0/2\pi\gamma s^2$, where Φ_0 is the magnetic flux quantum, γ is the anisotropy parameter, and s is the interlayer distance. For high fields the Josephson

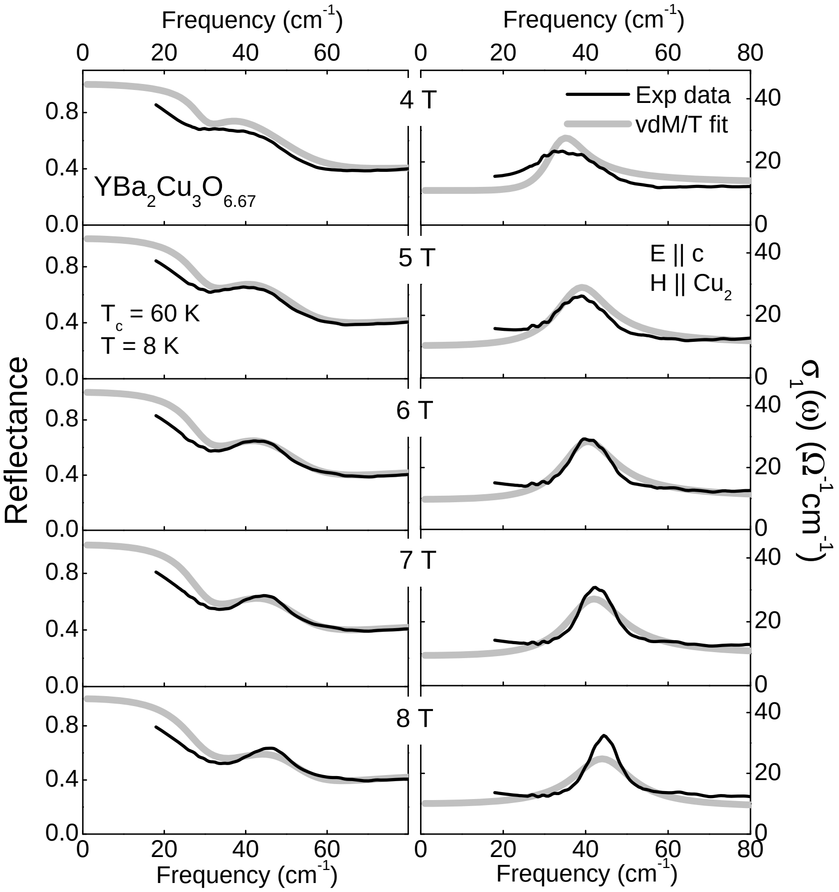

Figure 2.11: Fits (thick gray) to experimental reflectance data (thin black) at T=8 K and several values of magnetic field using theory of van der Marel and Tvetskov (left panels) and optical conductivity derived from fit function (right panels). These curves from the $y = 6.67$ doping are shown as example of the quality of fit which can be obtained. The model was also successful for the sample with $y = 6.75$. Fit parameters are displayed in Table 2.2, with the only free parameters being the linewidths γ_a and γ_b. All other parameters were measured directly in the conductivity and loss function or calculated as described in the text.

vortices fill every layer to form a dense lattice (Fig. 2.12(a)), but upon lowering below $H = H_{cr}$ it becomes favorable for each pair of layers containing vortices to be separated by an empty layer [Fig. 2.12(b)]. As the field is further decreased there is a complicated series of first order transitions between configurations with varying spacings, until a dilute lattice is eventually formed for $H << H_{cr}$ [Fig. 2.12(c)]. For Bi2212, $H_{cr} \approx 0.21$ T ($\gamma = 1100$, $s = 12$ Å), while for YBCO and La214 the field scales are 11 T ($\gamma = 20$, $s = 12$ Å) and 60 T ($\gamma = 13$, $s = 6.4$ Å), respectively.

The limitations on experimentally available magnetic field strength then place each sample in Fig. 2.8 in a different field regime. In the case of La214, the maximum field experimentally available (17 T) is just over a quarter of H_{cr}, so the vortex structure is still dilute. Thus, the data for La214 would be more accurately compared to the far left side of Fig. 2.8(e), where the upper frequency mode softens with field and the lower frequency mode is not yet observed. For YBCO, however, H_{cr} is only slightly higher than the upper experimental limit. For this system the low-frequency loss function peak is first resolved just below $H_{cr}/2$, as was observed for Bi2212. The broad onset of this feature in YBCO at fields as low as $H_{cr}/4$ has not yet been reconciled with the single-peaked spectra of La214. Only for Bi2212, which boasts an anisotropy 50–100 times as large as that of YBCO or La214, is the dense vortex lattice regime explored. This information provides justification for the assumptions of vortex superstructure at the core of the vdMT theory. It also allows insight into charging effects, for if the theoretical value of the vortex spacing is inserted into the equation for layer weight factors it is possible to determine the electronic compressibility. Further, these calculations allow for new numerical solutions of the interlayer phase equations (47) which will be discussed in Sec. III D.

2.3.4 Numerical solution of interlayer phase equations

Understanding of the Josephson vortex state electrodynamic response has been further advanced by the inclusion of another set of key parameters, the c-axis and in-plane dissipation values. Recently the equations describing phase dynam-

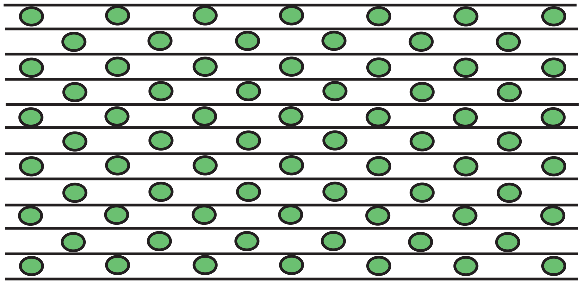

(a) $H >> H_{cr}$

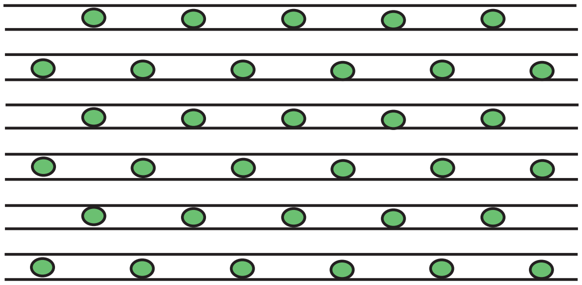

(b) $H < H_{cr}$

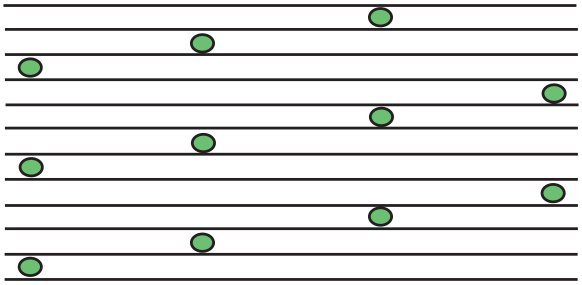

(c) $H << H_{cr}$

Figure 2.12: Ground state configuration of Josephson vortex lattice for several values of magnetic field, as predicted by Nonomura and Hu (48), and Koshelev (49). (a) For fields larger than the critical field scale H_{cr} (see text) vortices form a dense lattice. (b) Below H_{cr} the lattice undergoes a series of first order transitions to configurations in which layers with vortices are separated by N_z planes. (c) For small fields $H << H_{cr}$ vortices form a dilute lattice.

ics in a layered superconductor in parallel field have been solved numerically by Koshelev (47), yielding a solution for the complex dielectric function $\hat{\varepsilon}(\omega)$ which is valid for all frequencies and fields. This work begins with the coupled equations for the phase difference and magnetic field in the absence of charging effects (50; 51). Assuming a vortex lattice configuration with lattice spacing N_z, the static phase equations are solved for a fixed field. This solution is then input into dynamic phase equations to calculate the oscillating phase, and from it the loss function. This description depends strongly upon both the in-plane and c-axis dissipation parameters, $\nu_{ab} = 4\pi\sigma_c/\epsilon_c\omega_p$ and $\nu_c = 4\pi\sigma_{ab}\lambda_{ab}^2\omega_p/c^2$, which scale roughly as the inverse of the anisotropy. Also critical is the frequency dependence of their relative strengths. Such an approach provides a natural pathway for addressing the differences among cuprate families, and indeed many observed features are reproduced by the theory. For low values of the dissipation parameters (typical of those measured in Bi2212), the model matches the field dependence of the two modes measured in that system. And for high dissipation, as realized in underdoped YBCO, fields below H_{cr} generate the observed depletion of the main loss function peak and introduce a low-frequency mode, shown in Fig. 2.13. The model also exhibits a finite resonance in $\sigma_1(\omega)$ which hardens with magnetic field, in agreement with experimental observations. Here the theoretical curves have been scaled to the plasma frequency and peak heights of the experimental data. Excellent agreement is found in both the linewidths and frequency positions of field-induced modes.

The reliance of this method upon the quasiparticle dissipation initiates a comparison across cuprate families. It is known, for example, that the dc conductivities along the c axis of Bi2212 and YBCO can differ by three orders of magnitude (71). Also, the infrared/microwave data for YBCO reveal both a wider JPR linewidth and a stronger frequency dependence of the in-plane optical conductivity than is observed for La214 (72; 73; 74). This model, then, could be exposing the sensitivity of the JPR to these properties.

For completeness, we briefly mention two other structural differences which could contribute to disparities: pinning and layeredness. The CuO chain structure and twin boundaries, which are present only in YBCO, have been shown to affect

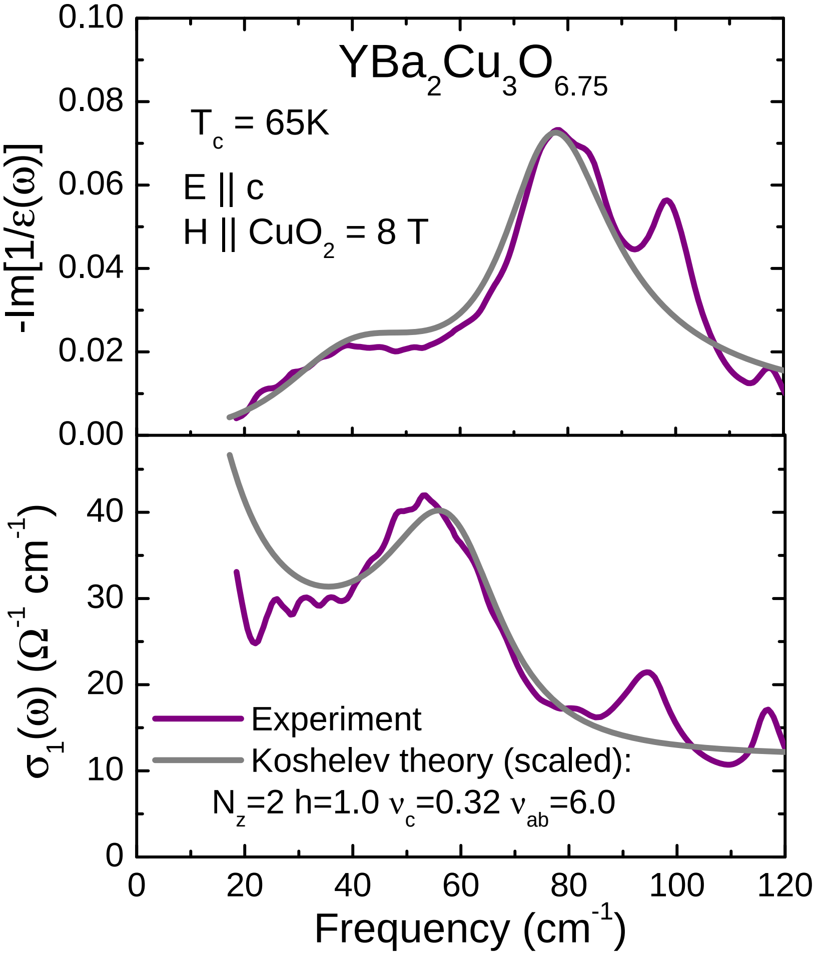

Figure 2.13: Theoretical loss function and optical conductivity (gray curves) predicted by Koshelev model (47) for a system with high dissipation ($\nu_c = 0.32, \nu_{ab} = 6.0$) in a static magnetic field $h = H/H_{cr}$ (see text). The value of $N_z = 2$ refers indicates there are two structural layers between each pair of layers with vortices. Experimental data (purple curves) represent measurements of YBa$_2$Cu$_3$O$_{6.75}$ crystals at $T = 8$ K and $H = 8$ T.

properties of vortex pinning (75; 76; 77) and may in turn influence the vortex resonance spectra. And of the three systems discussed here, only La214 is single-layered, while YBCO and Bi2212 have two and three layers, respectively. This factor could affect the vortex lattice ground state configuration.

2.4 Conclusion

In conclusion, we have tracked the electrodynamic response of $YBa_2Cu_3O_{6.67}$ and $YBa_2Cu_3O_{6.75}$ through changes in temperature and magnetic field, paying special attention to the low frequency resonance which appears in the vortex state. In contrast to the in-plane optical properties, which are largely insensitive to magnetic field (70), the c-axis response is strongly modified. We have shown that apparent disparities exist in the Josephson vortex state electrodynamic response of several families of cuprate superconductors. After examining proposed theoretical models we can conclude that the differences originate not in variations of vortex mass, but in anisotropy and dissipation. The description proposed by Koshelev (47) represents a significant step towards a coherent understanding of the interlayer response of the Josephson vortex state. Future spectroscopic measurements which expand the experimental phase diagram with higher magnetic fields and lower frequencies (78) should further elucidate this subject (78).

Acknowledgments

We thank A. E. Koshelev for illuminating discussions and for sharing his drafts prior to publication. This research was supported by the United States Department of Energy and the National Science Foundation. The work done at CRIEPI was supported by the Grant-in-Aid for Science provided by the Japan Society for the Promotion of Science.

Chapter 2, in full, is a reprint of the material as it appears in Phys. Rev. B **76**, 054524 (2007). A. D. LaForge, W. J. Padilla, K. S. Burch, Z. Q. Li, S. V.

Dordevic, Kouji Segawa, Yoichi Ando, and D. N. Basov, . The dissertation author was the primary investigator and author of this paper.

Chapter 3

Sum Rules and Interlayer Infrared Response of the High Temperature $YBa_2Cu_3O_y$ Superconductor in an External Magnetic Field

Abstract

We present infrared magneto-optical measurements of the *c*-axis conductivity of $YBa_2Cu_3O_y$ in both the underdoped (y=6.67 and 6.75) and optimally doped (y=6.95) regimes. We show that modest *c*-axis magnetic fields radically modify the condensate formation and restore conventional BCS-like energetics. Additionally, we demonstrate the pivotal role of interplane coherence in the anomalous high-energy contribution to the superfluid density.

3.1 Introduction

The theory of Bardeen, Cooper, and Schreiffer (BCS), undisputed for metallic superconductors, dictates that the transition involves a narrow interval of energies on the order of k_BT_c. Arguably, the most significant departure from the BCS scheme in high-T_c cuprate superconductors is revealed by optical studies (79; 15), which indicate that electronic processes occurring on the energy scale $(10^2 - 10^3)k_BT_c$ are often involved in the formation of the superconducting condensate (15; 16; 80; 81; 82; 83; 84; 85). These high-frequency optical effects can be interpreted in terms of electronic kinetic energy savings at $T < T_c$ (86; 87), at odds with predictions of the BCS theory.

The infrared (IR) optics technique offers an unparalleled window into the formation of the condensate in superconductors due to a well known relationship between the integral of the real part of the complex optical conductivity $\hat{\sigma}(\omega) = \sigma_1(\omega) + i\sigma_2(\omega)$ and the electronic kinetic energy $K_{\mathbf{r}}$ in the direction $\mathbf{r}$ (88; 89; 86; 87),

$$\int_0^\Omega d\omega\ \sigma_1(\omega) = \frac{\pi e^2 a_{\mathbf{r}}^2}{2\hbar^2} K_{\mathbf{r}}. \tag{3.1}$$

Here $a_{\mathbf{r}}$ is the lattice spacing in the $\mathbf{r}$ direction. The conductivity of a superconductor at $T < T_c$ has two contributions: $\sigma_{1,\mathbf{r}}^{SC}(\omega) = \rho_{s,\mathbf{r}}\delta(w) + \sigma_{1,\mathbf{r}}^{\text{reg}}(\omega)$, where the first term accounts for the response of the condensate and the second stands for the response of charges not participating in the pairing. Low-frequency spectral weight lost across the transition is transferred to the superfluid density $\rho_{s,\mathbf{r}} = \pi e^2 n_s / 2m_{\mathbf{r}}^*$, where n_s is the superconducting carrier density and $m_{\mathbf{r}}^*$ is the pair effective mass. Provided changes of the $K_{\mathbf{r}}$ are small, the conductivity follows the Ferrel-Glover-Tinkham (FGT) sum rule (90):

$$\int_0^\Omega d\omega\sigma_{1,\mathbf{r}}^{\text{N}}(\omega) = \rho_{s,\mathbf{r}} + \int_{0^+}^\Omega d\omega\sigma_{1,\mathbf{r}}^{\text{SC}}(\omega). \tag{3.2}$$

N denotes the normal state, and the cut-off Ω is usually comparable to few energy gap values. In many cuprates, however, the suppression of the conductivity in this frequency range is insufficient to fully account for the superfluid density (15; 16; 80; 81; 82; 83; 84; 85). The Hirsch kinetic energy sum rule (86) then allows one to interpret this additional contribution as a lowering of the electronic kinetic energy:

$$\rho_{s,\mathbf{r}} = \int_{0^+}^{\Omega} d\omega[\sigma_{1,\mathbf{r}}^{\mathrm{N}}(\omega) - \sigma_{1,\mathbf{r}}^{\mathrm{SC}}(\omega)] + \Delta K_{\mathbf{r}}. \tag{3.3}$$

An experimental survey of the energy scales associated with the superconducting condensate requires a perturbation that destroys or suppresses superconductivity, such as temperature, doping, and/or magnetic field. The former two approaches are easily achieved but may lead to artifacts in the analysis since they impact multiple coexisting interactions, thus obscuring processes directly related to the condensate formation (91). The magnetic field competes with superconductivity without introducing disorder; therefore, magneto-optical experiments are uniquely suited for exploring the condensate formation without significantly altering other properties.

Here, we use IR magneto-optical reflectance measurements to characterize the interplane electrodynamics across the phase diagram of $\mathrm{YBa_2Cu_3O}_y$, a prototypical high-T_c cuprate. We focused on the interplane (c-axis) response, where the condensate formation anomalies are most prominent. Doping trends seen in the c-axis energetics mirror in-plane results (15; 16; 80; 82; 83; 84), supporting the notion that it is the same phenomenon which is probed in two different polarizations of IR experiments (2). Our experiments show that high-energy contributions to the c-axis superfluid density in underdoped YBCO are eliminated with the application of modest magnetic fields, suggesting that kinetic energy-lowering is not essential to high-temperature superconductivity.

3.2 Experiment and results

Very clean YBCO single crystals studied in this work were grown in pure $\mathrm{Y_2O_3}$ crucibles using a flux method (92). They were annealed to oxygen dopings of $y = 6.67$, 6.75, and 6.95, leading to sharp superconducting transitions at temperatures $T_c = 60$, 65, and 93 K, respectively (41). c-axis polarized magneto reflectance measurements were performed over a broad range of frequency (18-35 000 cm^{-1}) and magnetic field (0-8 T) and are described in greater detail in Refs. (93) and

(43). Reflectance data with appropriate extrapolations were transformed using the Kramers-Kronig relations to obtain the optical conductivity $\hat{\sigma}(\omega)$. Figures 3.1(a-c) show the real part $\sigma_1(\omega)$. At optimal doping [Fig. 3.1(c)] the optical conductivity at T_c is flat in the far-IR, followed by a series of optically active phonons from 100-700 cm^{-1}. As temperature is lowered below T_c, far-IR conductivity levels drop and spectral weight (SW) is transferred into the superconducting δ-peak at $\omega = 0$. In underdoped samples [Figs. 1(a) and 1(b)], however, the suppression of the far-IR conductivity begins in the pseudogap state at T above T_c and is accompanied by transfer of spectral weight at mid-IR frequencies (94). The asymmetrical mode near 450 cm^{-1} (23; 95), which is already visible in the pseudogap state, grows dramatically below T_c. All these findings are consistent with earlier systematic studies of YBCO (10; 96; 97).

The dominant effects of the c-axis magnetic field H on the 8 K conductivity of both underdoped samples [Fig. 3.1 (a,b)] are the simultaneous softening/weakening of the asymmetric mode near 450 cm^{-1} and the growth of the high-frequency tail of the phonon at 320 cm^{-1}. In the optimally doped sample, background conductivity levels increase with field, and the resonance at 800 cm^{-1} is suppressed.

Next we present, in Fig. 3.1 (d-f) and Fig. 3.2, the key experimental results of this work revealing the field-induced redistribution of the electronic spectral weight in the conductivity. It is instructive to introduce the integral spectral function $\Delta N_{T_c}(\omega, H) = \int_{0^+}^{\omega} d\omega'[\sigma_1(\omega', T_c, 0\,\mathrm{T}) - \sigma_1(\omega', 8\,\mathrm{K}, H)]$ quantifying the spectral weight transferred to the $\delta(\omega)$ peak from the frequency region confined to ω. Values of ρ_s (calculated from $\sigma_2(\omega)$ (5)) are plotted for 0 T and 8 T on the right-hand axes of the main panels of Fig. 3.1 in the same units as the SW change, and they appear for all fields and dopings in Fig. 3.2. Figure 3.2 also displays the values of $\Delta N_{T_c}(\Omega_c)$ for H=0-8 T. We used cut-off frequencies Ω_c=1000 cm^{-1} for underdoped samples and 1300 cm^{-1} for the optimally doped crystal because field-induced changes of raw reflectance become negligibly small beyond these values. Lastly, we have identified the difference between ρ_s and $\Delta N_{T_c}(\Omega_c)$ as the high-frequency contribution to the superconducting condensate. This term is labeled

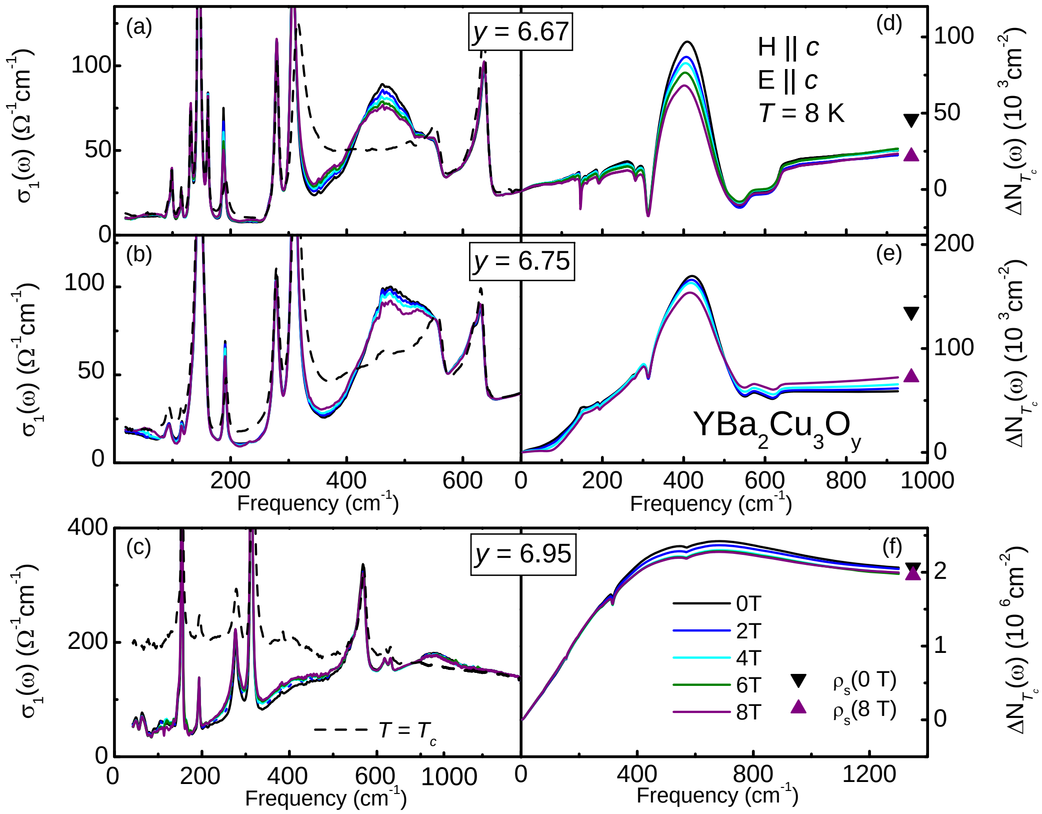

Figure 3.1: Condensate formation revealed by IR magneto-optics for $YBa_2Cu_3O_y$ crystals with oxygen content y=6.67 (top), y=6.75 (middle), and y=6.95 (bottom) Magnetic field is oriented parallel to the c axis. Left panels: Optical conductivity at T=8 K in magnetic field (solid curves) and at T_c (dashed). Right panels: Difference in integrated SW between normal ($T > T_c$) and superconducting state $\Delta N_{T_c}(\omega, H) = \int_{0+}^{\omega} d\omega'[\sigma_1(\omega', T_c, 0\,\mathrm{T}) - \sigma_1(\omega', 8\,\mathrm{K}, H)]$. Line legend is common for all panels.

as ΔK_c to underscore the proposed link to the kinetic energy change.

Proceeding with discussion of the field-induced redistribution of the electronic SW, we will consider first the y=6.67 crystal. The data in Fig. 3.1(d) show that at $H = 0$ (black curves) the background level of $\Delta N_{T_c}(\omega)$ increases with frequency, with changes to phonons and the asymmetrical mode appearing as sharp features. Importantly, $\Delta N_{T_c}(\Omega_c)$ is nearly unchanged for $H||c$. The asymmetrical mode and the 320 cm^{-1} phonon in the conductivity are significantly modified by field, but the majority of the SW transfer takes place between these two features, conserving the finite-frequency SW in the far-IR region. Figure 3.2 illustrates trends in the field dependence of $\Delta N_{T_c}(\Omega_c)$ and ρ_s; the latter is suppressed by about 50% at the highest field in both underdoped samples. At zero field the finite-frequency SW lost below Ω_c only constitutes half of that gained by the superconducting condensate, implying that the remaining portion of the condensate must be transferred from higher energies. As magnetic field is applied we see in greater detail the effect apparent in Fig. 3.1: $\Delta N_{T_c}(\Omega_c)$ is roughly constant, while ρ_s is suppressed nearly linearly with H. Thus, the shrinking shaded regions in Fig. 3.2 represent the waning contribution of higher-energy SW to the condensate. This result is significant since, in view of Eq. 3.3, it implies that the energetics of the superconducting transition are dramatically modified by magnetic field.

Continuation of this analysis across the phase diagram reveals other interesting trends. Features of the $H||c$ data for the second underdoped sample (y=6.75) are generally similar to those discussed for y=6.67, but data for the optimally doped crystal, shown in Fig. 3.2(c), exhibit important differences. First, there is no high-energy contribution to the condensate observed at zero field: $\Delta N_{T_c}(\Omega_c)/\rho_s \simeq 1$ with high accuracy. Second, this condition is maintained up to the highest measured fields, as changes in ρ_s consistently match those in $\Delta N_{T_c}(\Omega_c)$. Thus, at optimal doping the superconducting transition involves no high-energy transfer of spectral weight.

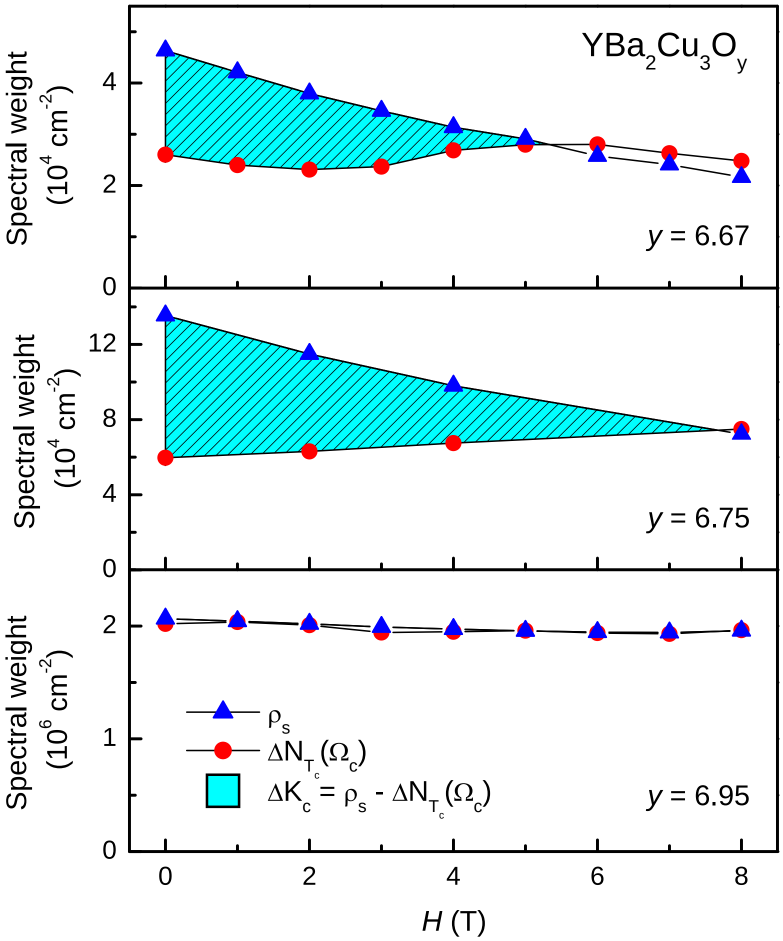

Figure 3.2: Comparison of spectral weight redistribution in c-axis magnetic field for $\mathrm{YBa_2Cu_3O}_y$ at y=6.67 (top panel), 6.75 (middle), and 6.95 (bottom) doping levels. Red circles represent the value of $\Delta N_{T_c}(\Omega_c,\, H)$ at cut-off frequencies Ω_c = 1000 cm^{-1} for the underdoped crystals and Ω_c = 1300 cm^{-1} for the optimally doped system. Blue triangles indicate total superfluid density at each value of magnetic field. High energy contributions (shaded regions) were inferred from $\rho_s - \Delta N_{T_c}(\Omega_c,\, H)$ and can be interpreted as kinetic energy change ΔK_c via Ref. (86).

3.3 Discussion

In light of the introductory comments on the energetics of condensate formation, it is clear that the magneto-optics data presented in Figs. 1-2 for $H||c$ seriously undermine the notion of kinetic-energy-driven superconductivity. We see that the high-energy contribution to the condensate, which can be interpreted in terms of kinetic energy change in underdoped samples, is mostly eliminated by 5-8 T. This evidence for a robust superconducting state in the absence of a substantial kinetic energy change weakens the case for this type of condensation mechanism. Furthermore, effects attributable to kinetic energy change never appear at optimal doping.

Remarkably, the conventional condensation scheme has been restored in underdoped samples via field-induced modification of processes occurring at energies exceeding the energy scale of the magnetic field by several orders of magnitude. Equally surprising is the giant (50%) depression of the superfluid density observed in underdoped samples despite the fact that the maximum field in our experiments is much smaller than the pairbreaking field (98; 99). We propose that both effects share a common origin related to the interlayer phase coherence. First, note that pancake vortices initiated by the $H||c$ field are likely to be misaligned in the c direction due to pinning (100). This vortex meandering is known to introduce a phase difference $\phi_{n,n+1}(r)$ between neighboring layers (101; 102). An immediate consequence is that the average strength of the interlayer Josephson coupling $J \propto J_0 cos(\phi_{n,n+1})$ is reduced, leading to suppression of the c-axis superfluid density governed by J. The finite interplane phase difference in the vortex state is of direct relevance to a scenario for a contribution to ρ_s originating from energies much larger than $k_B T_c$ proposed by Ioffe, Millis, and Shah (IMS) (103; 104). According to these calculations the high-energy contribution is indeed expected, provided the superconducting transition occurs from a state where pairing already exists but phase coherence between the planes is still missing and is only established below T_c. Importantly, vortex meandering is in direct competition with the restoration of interlayer phase coherence. Extending this argument to the IMS picture one can conclude that the above competition reduces and eventually eliminates the high-energy contribution to the δ peak, in accordance with our findings. It is important to note that the theoretical results in Refs. (103; 104),are sensitive to the details of the bilayer couplings, and that a different behavior may be expected for single-layer cuprate compounds. The central role of phase fluctutation is underscored by the fact that these enigmatic field-induced effects are observed only in the underdoped region of the phase diagram, where accurate terahertz experiments (105) and Nernst measurements (106) have established superconducting pairing above T_c.

In summary, our data demonstrate that relatively small magnetic fields can modify spectral weight redistribution in a prototypical family of cuprate superconductors over an anomalously large energy scale. Fields $H||c$ of 8 T suppress the high-frequency contribution to the zero-ω $\delta(\omega)$ peak but do not completely destroy the superfluid density, leaving a robust superconducting state. These findings point toward a more BCS-like formation of the superconducting condensate even in underdoped samples where earlier zero-field data pointed to a highly exotic condensation process. The large energy scale of the associated electronic processes then seems to be a generic property of correlated electron systems, but only peripherally related to superconductivity. Furthermore, we have proposed a scenario in which the changes in spectral weight redistribution are linked to a reduction in phase coherence in the superconducting state, primarily due to vortex meandering.

Acknowlegdments

This research was supported by the National Science Foundation. YA was supported by KAKENHI 19674002.

Chapter 3, in full, is a reprint of the material as it appears in Physical Review Letters **101**, 097008 (2008). A. D. LaForge, W. J. Padilla, K. S. Burch, Z. Q. Li, A. A. Schafgans, Kouji Segawa, Yoichi Ando, and D. N. Basov. The dissertation author was the primary investigator and author of this paper.

Chapter 4

Magnetic field-induced modification of superfluid density and interplane spectral weight in $YBa_2Cu_3O_y$

4.1 Abstract

We report on the interlayer infrared response of $YBa_2Cu_3O_y$ in an applied magnetic field. This study explores both the underdoped ($y = 6.67$ and 6.75) and optimally doped ($y = 6.95$) regions of the phase diagram, and includes data for fields applied both parallel to the c axis and to the CuO_2 planes in this anisotropic superconductor. We focus on the transfer of optical conductivity spectral weight from high-frequency regions of the spectrum to the non-dissipative superconducting condensate, and examine the effect of magnetic field upon this process. A sum rule analysis reveals that magnetic fields $H \parallel c$ eliminate the high-frequency contribution to the superfluid density, returning the system to a more BCS-like energy scale. For fields $H \parallel CuO_2$, however, the high-energy contribution scales

with the superfluid density, and the anomalous scheme of condenstate formation is maintained, at least in underdoped y=6.67 and 6.75 samples. This behavior is discussed in relation to the change of electronic kinetic energy and shown to be closely related to the suppression of interplane phase coherence.

4.2 Introduction

Infrared spectroscopy is a powerful tool for studying condensed matter systems. It provides numerous insights due to its sensitive resolution of subtle spectral characteristics, but also for its ability to utilize data from a wide frequency range to determine system properties based on conservation laws and sum rules. For example, one of the Kubo conductivity sum rules relates the integrated real part of the optical conductivity $\sigma_1(\omega)$, or spectral weight, over all bands to the number density N_e and mass m of electrons in the solid (107):

$$\int_0^\infty d\omega\ \sigma_{1,\mathbf{r}}(\omega) = \frac{\pi}{2}\frac{ne^2}{m} \tag{4.1}$$

If we restrict our attention to a single band, however, it is possible to relate the low-frequency spectral weight to the occupancy and dispersion of that band. In the tight binding approximation the spectral weight is simply proportional to the electronic kinetic energy $K_\mathbf{r}$ (88; 89; 86; 87; 2):

$$\int_0^\Omega d\omega\ \sigma_{1,\mathbf{r}}(\omega) = \frac{\pi}{2}\frac{e^2 a_\mathbf{r}^2}{\hbar^2} K_\mathbf{r}. \tag{4.2}$$

A sum rule which is quintessential for the understanding of superconductivity was formulated by Ferrell, Glover, and Tinkham (FGT); it equates the spectral weight lost in the superconducting gap to the strength of the zero-frequency superconducting condensate, quantified by the superfluid density ρ_s:

$$\rho_{s,\mathbf{r}} = \int_{0^+}^\Omega d\omega[\sigma_{1,\mathbf{r}}^{\mathrm{N}}(\omega) - \sigma_{1,\mathbf{r}}^{\mathrm{SC}}(\omega)]. \tag{4.3}$$

The FGT sum rule (90) is valid for elemental superconductors which are well-described by the theory of Bardeen, Cooper, and Schreiffer (BCS). In this case the difference in spectral weight between the normal and superconducting states

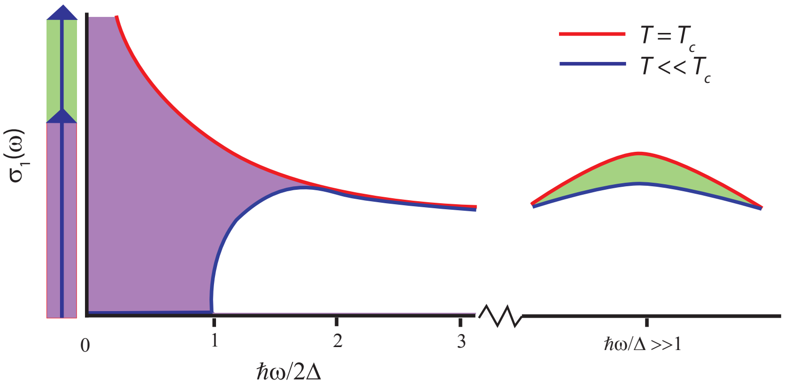

Figure 4.1: Optical conductivity of a superconductor in the normal (dashed lines) and superconducting (solid lines) states (schematic, adapted from Ref. 4). As the superconducting gap opens,spectral weight is shifted from finite frequencies to the δ function at zero frequency. In many cuprate superconductors the superfluid is composed of spectral weight transferred from both low- (solid shaded regions) and high- (horizontally hatched regions) frequency parts of the spectrum.

reaches the full value of ρ_s by an integration cutoff of only a few gap values. However, for many high-T_c cuprate superconductors, optical experiments (79; 15; 16; 108; 80; 81; 82; 83; 84; 109; 85) have revealed that the difference in conductivity only constitutes a portion of the superfluid when integrated up to several gap values. This behavior implies that the extra spectral weight in the superconducting condensate must be transferred from much higher energies, and also that the system experiences a lowering of electronic kinetic energy during the superconducting transition. The spectral weight shift during the transition is then described (86) by

$$\rho_{s,\mathbf{r}} = \int_{0^+}^{\Omega} d\omega[\sigma_{1,\mathbf{r}}^{\mathrm{N}}(\omega) - \sigma_{1,\mathbf{r}}^{\mathrm{SC}}(\omega)] + \Delta K_{\mathbf{r}}, \tag{4.4}$$

and is illustrated schematically in Fig. 4.1.

High-energy effects are common to at least four different families of cuprates, appearing in both ab-plane and c-axis measurements. Typically, they are only observed at doping levels below the optimal value, and not in the overdoped regime. Such broad occurance and similarity in doping dependence prompted many to consider whether the lowering of electronic energy was an essential component to the superconducting mechanism in this class of materials. These questions sparked a need for experiments that could unambiguously identify the high-energy spectral weight transfer and access a weakened superconducting state to verify if the condensation scheme remained intact when the order parameter was suppressed. Infrared measurements in which the incident electric field is polarized parallel to the c axis are highly sensitive to changes in kinetic energy and therefore uniquely suited to address this experimental need. Further, the desired perturbation can be provided by application of an external mangetic field, which competes with superconductivity without promoting disorder. Consequently, the technique of infrared optics in magnetic field is an ideal tool for probing these phenomena.

We have previously reported on infrared measurements (110) of underdoped $YBa_2Cu_3O_y$, a prototypical high-T_c superconductor, recording the evolution of the spectral weight balance in magnetic field $H \parallel c$. We found that, from a sum rule analysis point of view, the high field data were less anomalous than at zero field. Here, we extend these results to include sum rule analysis in magnetic field for data recorded at higher temperatures, as well as for magnetic fields oriented parallel to the CuO_2 planes. Section 4.2 provides details regarding our infrared magneto-optical experiment and reflectance data, and Section 4.3 presents the calculated optical conductivity. The sum rule analysis of the conductivity data is described in Section 4.4 and, lastly, connections to interlayer phase coherence and vortex lattice resonance modes are discussed in Section 4.5.

4.3 Infrared reflectance experiment in magnetic field

High-quality ac-face single crystals of $YBa_2Cu_3O_y$ (YBCO) were grown using a flux method (92) and annealed to achieve doping levels of y=6.67, 6.75 (both underdoped), and 6.95 (optimally doped). Transport measurements (41) reveal sharp transitions to the superconducting state at 60 K, 65 K, and 93 K, demonstrating the high purity of the crystals. For each doping several single crystals from a single batch were assembled to form mosaics approximately 3x6 mm^2 in size.

Near-normal reflectance measurements were performed in a broadband Fourier transform spectrometer over a frequency range of 18-35 000 cm^{-1}. First, absolute reflectance was obtained at temperatures T = 8-295 K by measuring sample reflectance relative to a stainless steel reference mirror and normalizing by the reflectance of the sample coated with Au (42). Then, changes in reflectance induced by magnetic field H were recorded via the ratio $R(T,H)/R(T,H=0)$ in a split-coil magnet (43) for field magnitudes up to 8 T. This step utilized an Al reference mirror to correct for minor spurious effects in the magnet system.

Reflectance spectra for the YBCO system (Fig. 4.2) are weakly metallic near room temperature, with an upturn toward $R=1$ as $\omega \to 0$. The sharp peaks in the far infrared correspond to phonons. As temperature is decreased to T_c the reflectance of the most metallic, optimally doped sample increases, while that of the underdoped crystals decreases, due to the formation of the pseudogap (9; 111; 10; 13). At temperatures below T_c the Josephson plasma edge develops, corresponding to coherent oscillation of the non-dissipative superconducting condensate. This feature is characterized by very high reflectance at low- frequencies followed by a sharp dip at the Josephson plasma resonance (JPR) frequency $\omega_s = \sqrt{\rho_s/\epsilon_\infty}$. This frequency, a direct measure of the superfluid density, softens with oxygen reduction, (from $\omega_{JPR} = \approx 250$ cm^{-1} at $y = 6.95$ to $\omega_{JPR} = 60$ cm^{-1} at y=6.67) and stiffens at lower temperatures. Also, in the underdoped crystals a broad, asymmetric feature near 450 cm^{-1} which is weakly visible above T_c becomes significantly more prominent in the superconducting state. These results are consistent with previous studies of similar YBa$_2Cu_3O_y$ compounds (9; 10; 11; 7; 12; 13; 8).

Application of magnetic field parallel to the c axis in many respects reverses the trends of lowering temperature. As seen in Fig. 4.3, for underdoped crystals the field softens the JPR and reduces the magnitude of the asymmetric feature. For $H \parallel c$ no new features are observed in $R(\omega)$. Magnetic fields $H \parallel$ CuO$_2$ (Fig. 4.4), however, do introduce new absorption features at frequencies below the JPR. The frequency of the dip in $R(\omega)$ increases with field, moving from 26 to 36 cm^{-1} by 8 T. This behavior is consistent with earlier studies of the YBCO system, and has been discussed in detail previously by some of us (93). The magnetic field $H \parallel$

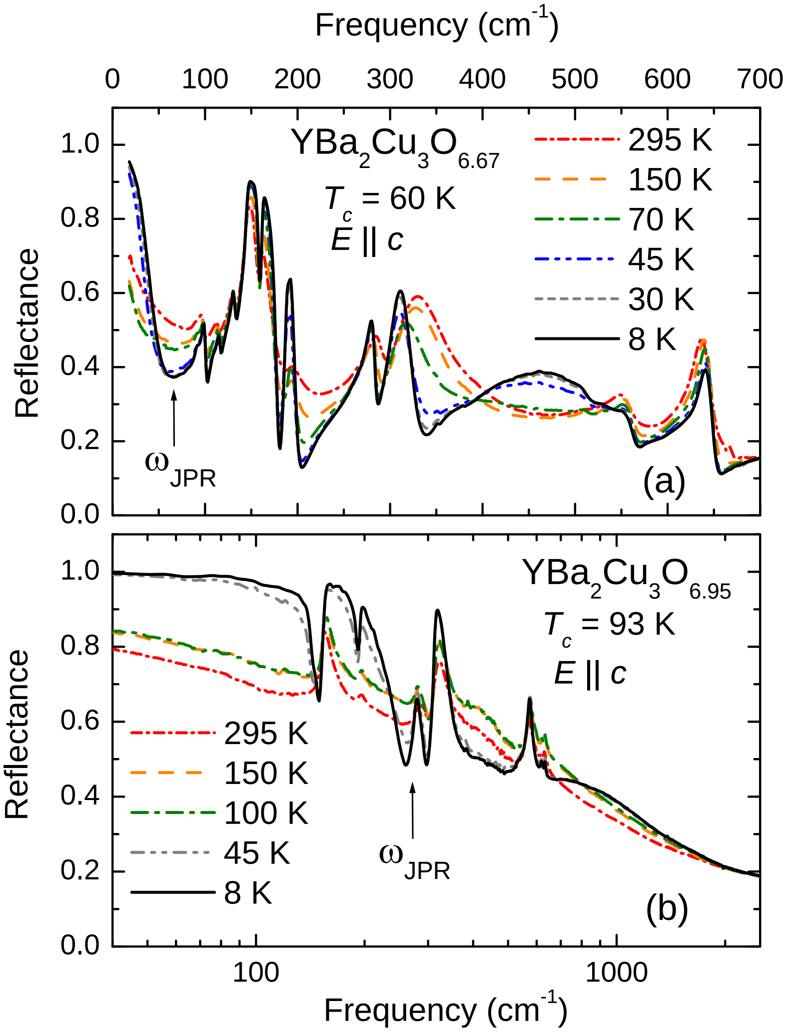

Figure 4.2: Infrared reflectance $R(\omega)$ of $YBa_2Cu_3O_y$ single crystals for dopings (a) y=6.67 and (b) 6.95 at several temperatures above and below T_c.

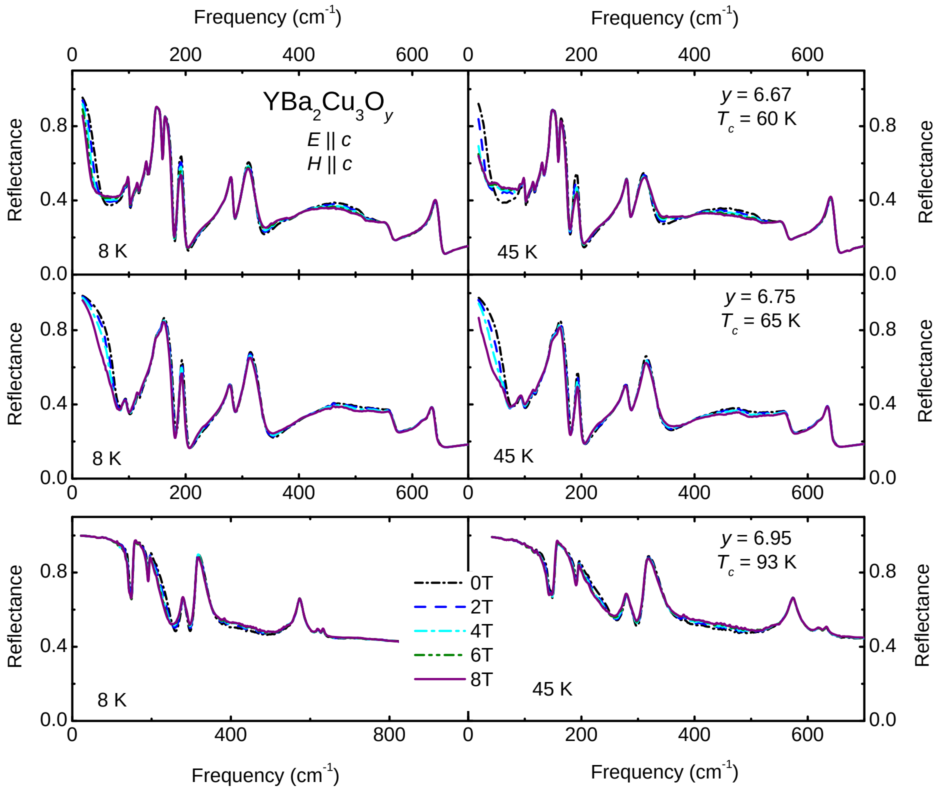

Figure 4.3: Infrared reflectance $R(\omega)$ of $YBa_2Cu_3O_y$ single crystals for dopings y=6.67 (top), 6.75 (middle) and 6.95 (bottom) at temperatures T=8 K (left) and 45 K (right). Magnetic fields up to H=8 T are applied parallel to the c axis.

CuO_2 induces no appreciable changes in the reflectance for frequencies $\omega > 100$ cm^{-1}.

4.4 Optical conductivity

Reflectance data were transformed via the Kramers-Kronig relations to obtain the optical conductivity $\hat{\sigma}(\omega)$. Because this calculation requires the input of $R(\omega)$ over the full frequency half-space, we augment the raw data with appropriate low- and high-frequency extrapolations. In the normal state we assumed a Hagen-Rubens metallic response of the form $(1 - R) \propto \omega^{1/2}$ for frequencies below the lowest measured data. A two-fluid form was assumed in the superconducting state. High frequency data were extended to $+\infty$ with a combination of linear and

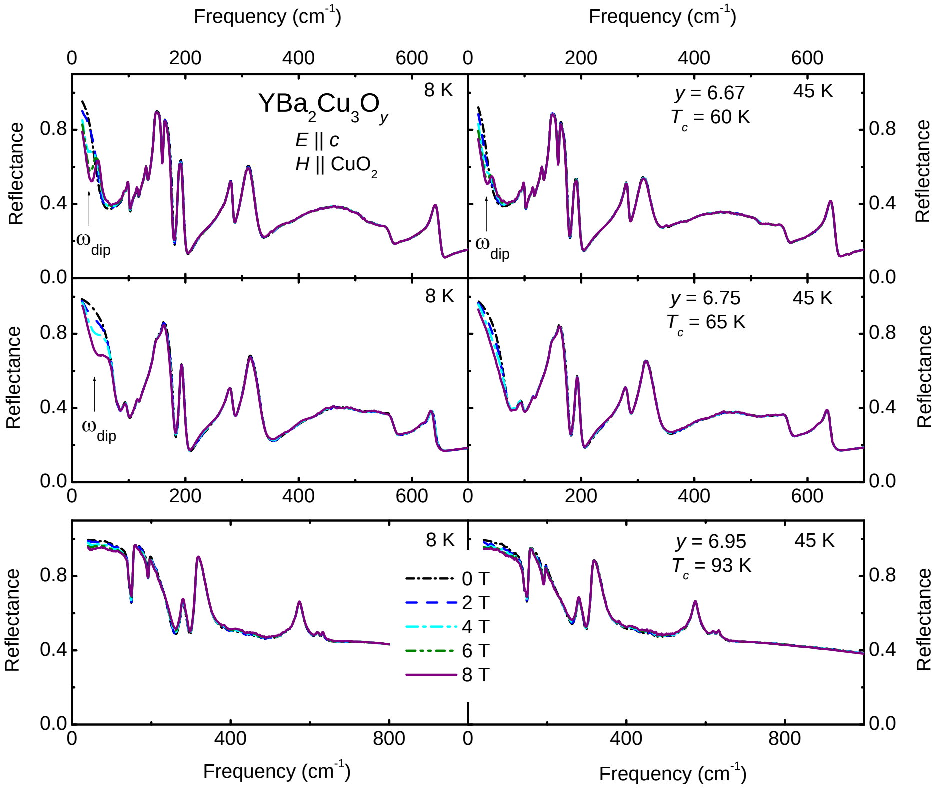

Figure 4.4: Infrared reflectance $R(\omega)$ of YBa$_2$Cu$_3$O$_y$ single crystals for dopings y=6.67 (top), 6.75 (middle) and 6.95 (bottom) at temperatures T=8 K (left) and 45 K (right). Magnetic fields up to H=8 T are applied parallel to the CuO$_2$ planes.

ω^{-4} asymptotic extrapolations.

The real part of the optical conductivity $\sigma_1(\omega)$ at zero magnetic field is displayed in Fig. 4.5. The room temperature conductivity is flat overall, interrupted only by a series of infrared active phonons. For the optimally-doped crystal, the background conductivity increases with decreasing temperature to T_c, consistent with a metallic system. The underdoped crystals, however, become less conductive upon lowering to $T = T_c$, and reach maximum conductivity levels roughly an order of magnitude smaller than those of the optimally-doped case. Further cooling reveals a partial gapping of the Fermi surface, characteristic of the pseudogap. In oxygen-reduced crystals spectral weight (SW) is removed from phonons to create a broad band near 450 cm^{-1}. This feature has been previously studied in detail and may be consistent with either a bilayer transverse plasmon mode or a bilayer splitting (14; 8; 95; 23).

As found in the reflectance, modifications to the conductivity by the magnetic field are strikingly dissimilar in the different field orientations. For $H \parallel c$ (Fig. 4.6) no new modes appear in $\sigma_1(\omega)$, but substantial changes occur in the phonon region. In the underdoped crystals the field initiates a pronounced shift of SW from the asymmetrical mode back into the phonon at 320 cm^{-1}, mirroring the effect of raising temperature. Direct evidence for the equivalence of increasing magnetic field and temperature is found in Fig. 4.7, where we plot for the $y = 6.67$ crystal $\sigma_1(\omega)$ at 8 K (0 T and 8 T), 45 K (0 T and 8 T) as well as just above T_c at 70 K. Using the 8 K, 0 T result as a starting point, it is clear that both H and T drive the spectrum towards the 70 K curve. The result of raising T to 45 K at zero field is nearly identical to that of raising H to 8 T and keeping T fixed.

The data for fields applied parallel to the CuO$_2$ planes, shown in Fig. 4.8, exhibit fundamentally different behavior than was observed for $H \parallel c$. For magnetic fields $H \parallel$ CuO$_2$ a resonance appears at low frequencies (27). With increasing magnetic field the resonance hardens and gains SW. This feature has been shown to have its origin in Josephson vortex lattice dynamics (27; 93; 47). Other than minor modifications to the electronic background which affect phonon features, minimal field-induced changes occur at higher frequencies.

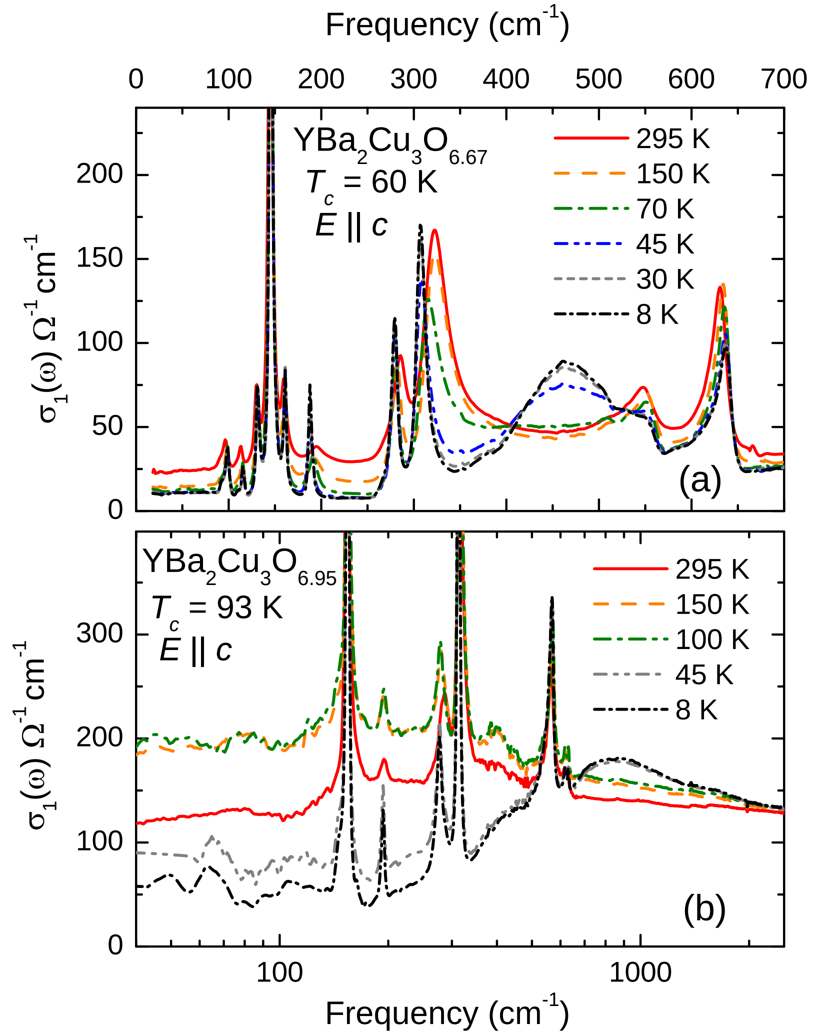

Figure 4.5: Optical conductivity of YBa$_2$Cu$_3$O$_y$ single crystals for dopings (a) y=6.67 and (b) 6.95 at several temperatures above and below T_c.

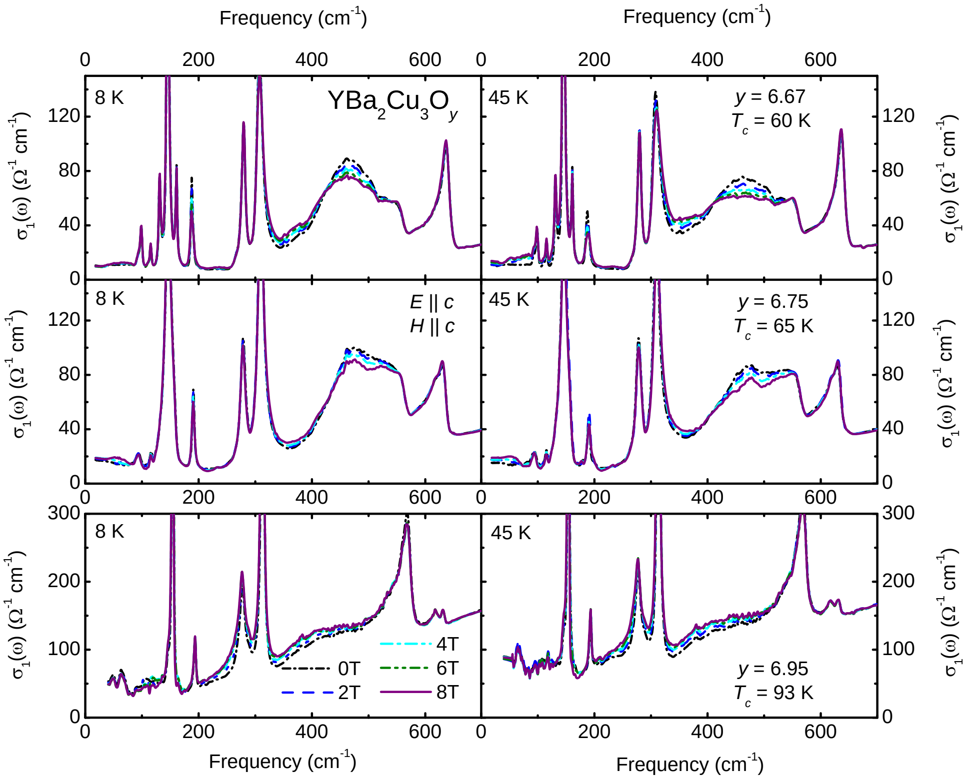

Figure 4.6: Optical conductivity of YBa$_2$Cu$_3$O$_y$ single crystals for dopings y=6.67 (top), 6.75 (middle) and 6.95 (bottom) at temperatures T=8 K (left) and 45 K (right). Magnetic fields up to H=8 T are applied parallel to the c axis.

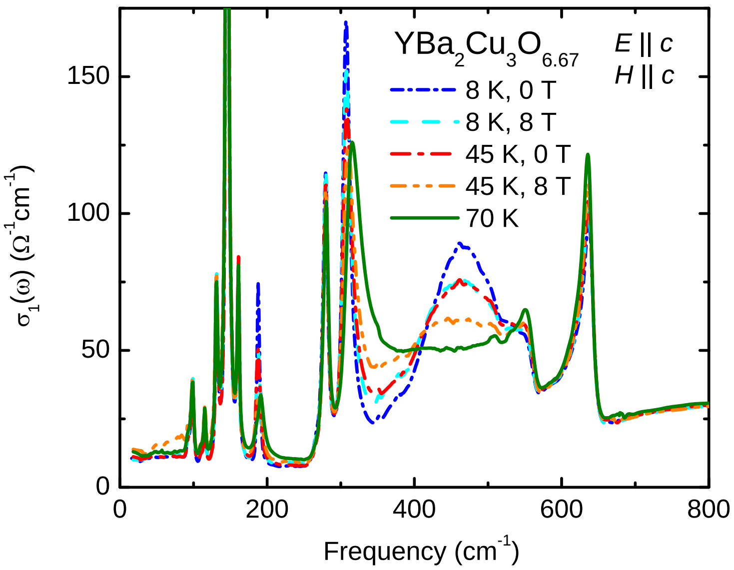

Figure 4.7: Optical conductivity for $YBa_2Cu_3O_{6.67}$ single crystal at 8 K (0 T and 8 T), 45 K (0 T and 8 T) and just above T_c at 70 K. Similarity between 8 K, 8 T curve and 45 K, 0 T curve demonstrates equivalence of temperature and magnetic field $H \parallel c$ for modification of optical properties.

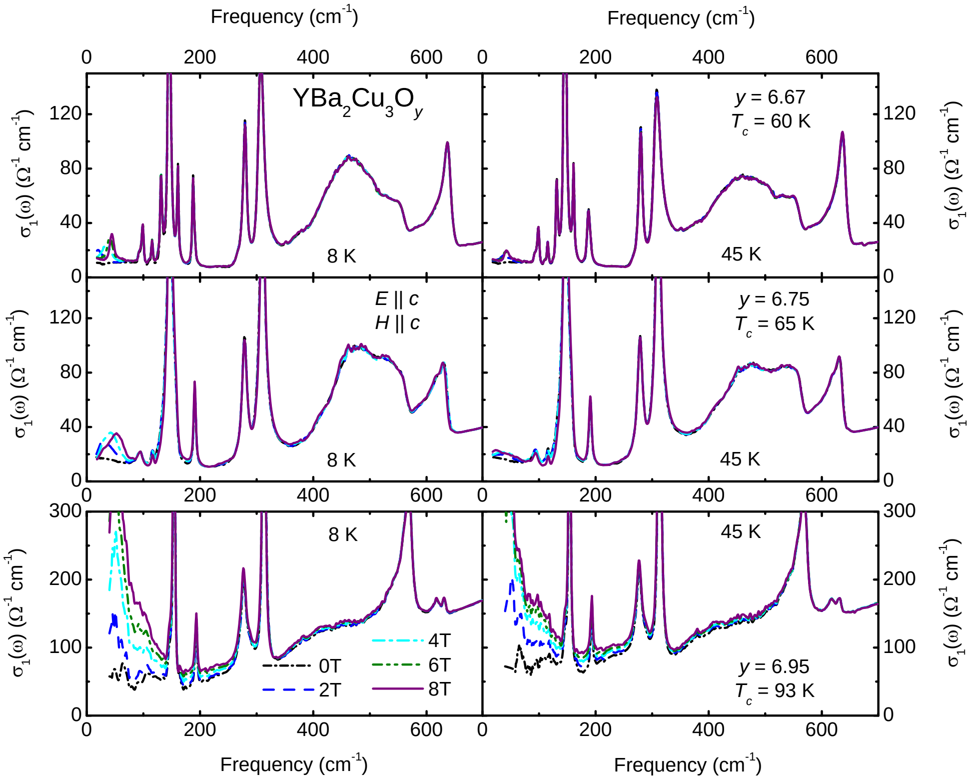

Figure 4.8: Optical conductivity of $YBa_2Cu_3O_y$ single crystals for dopings y=6.67 (top), 6.75 (middle) and 6.95 (bottom) at temperatures T=8 K (left) and 45 K (right). Magnetic fields up to H=8 T are applied parallel to the CuO_2 planes.

4.5 Sum rules and spectral weight transfer

To investigate in more detail the energy scales governing the superconducting transition we now compare the low-frequency integrated SW with the superfluid density at key values of temperature and magnetic field. We will show that magnetic fields $H \parallel c$ rapidly eliminate the high-frequency transfer of spectral weight to the superfluid density, while fields $H \parallel \mathrm{CuO_2}$ suppress the high-energy contribution proportionately to the superfluid density. The integral spectral function $\Delta N_{T_c}(\omega,\, H) = \int_{0+}^{\omega} d\omega' [\sigma_1(\omega',\, T_c,\, 0\,\mathrm{T}) - \sigma_1(\omega',\, 8\,\mathrm{K},\, H)]$ quantifies the SW transferred to the $\delta(\omega)$ peak from frequencies less than ω. Representative $\Delta N_{T_c}(\omega,\, H)$ curves are plotted in Fig. 4.9 for fields oriented both parallel to the c axis (panels a and b) and to the $\mathrm{CuO_2}$ planes (panels c and d) at T=8 K. The values of $\Delta N_{T_c}(\Omega_c)$ are plotted in Figs. 4.10 and 4.11 at $T = 8$ K (left column) and 45 K (right column) for magnetic fields up to 8 T. Also plotted in Figs. 4.10-4.11 is the superfluid density $\rho_s(H)$. The zero-frequency superconducting condensate is non-dissipative, and thus cannot be directly observed in the $\sigma_1(\omega)$ spectra. Due to causality relations, however, its strength can be deduced from the inductive part of the conductivity $\sigma_2(\omega)$, which behaves as ρ_s/ω in the superconducting state (5). At each value of magnetic field the difference $\rho_s(H)$-$\Delta N_{T_c}(\omega,\, H)$ is indicated by the shaded region and labeled as ΔKE to emphasize the connection to the kinetic energy change, as outlined in the introduction.

The differing effects of the two magnetic field geometries can be clearly seen in the evolution of low-frequency SW. In general, each $\Delta N_{T_c}(\omega,\, H)$ spectrum exhibits spikes in the far-infrared at frequencies where phonons or other modes are modified. These spikes are superimposed upon a background which increases as a function of frequency through the far-infrared, then levels off to a constant value. The cutoff frequencies Ω_c were chosen to be in these flat regions, at 1000 cm^{-1} for the underdoped crystals and 1300 cm^{-1} for the optimally doped one. Let us begin with the case of $H \parallel c$ (top panels). Here, for both underdoped and optimally doped crystals the values of $\Delta N_{T_c}(\omega,\, H)$ at frequencies above the phonon region are unchanged by magnetic field. The primary impact of magnetic field is simply to redistribute SW within the low-frequency region. Comparing SWs in Fig. 4.10,

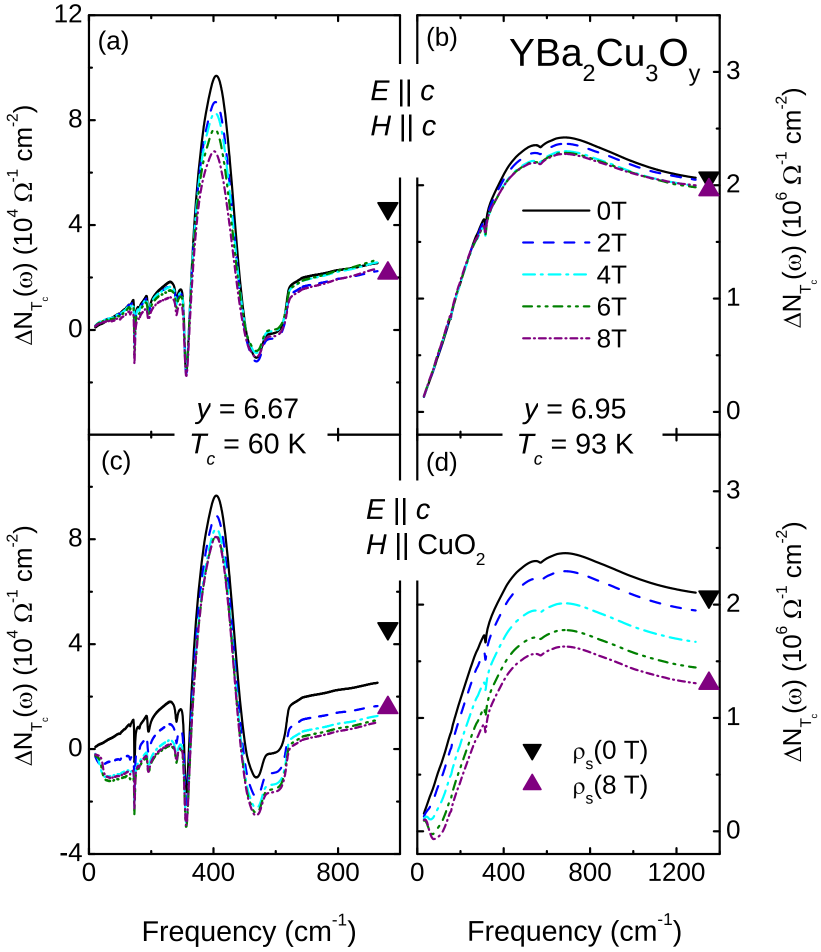

Figure 4.9: Difference in integrated SW between normal ($T > T_c$) and superconducting state $\Delta N_{T_c}(\omega, H) = \int_{0^+}^{\omega} d\omega' [\sigma_1(\omega', T_c, 0\,\mathrm{T}) - \sigma_1(\omega', 8\,\mathrm{K}, H)]$ for dopings y=6.67 (left) and 6.95 (right). Magnetic fields are applied parallel to the c axis (top) and $\mathrm{CuO_2}$ planes (bottom).

we see that for underdoped samples at zero field the value of the superfluid density is nearly twice that of $\Delta N_{T_c}(\omega)$. From this we infer that the extra SW in the superfluid must have been transferred from higher frequencies. As the magnetic field is increased the superfluid density is strongly suppressed, in contrast to the mostly flat behavior of $\Delta N_{T_c}(\Omega_c, H)$. Eventually the two curves cross or merge, with the intersection being driven to lower fields as temperature is increased to 45 K. In the data recorded for the optimally doped crystal, the superfluid density closely matches the missing SW at zero field, and neither quantity is changed by magnetic field.

Application of the magnetic field parallel to the CuO_2 planes results in a qualitatively different picture of SW transfer. For underdoped crystals, the superfluid density behaves similarly to the $H \parallel c$ orientation, with a strong suppression in field. The low-frequency finite SW change, seen in the bottom panels of Fig. 4.9, as well as in Fig. 4.11, is no longer field-independent: the limiting values of $\Delta N_{T_c}(\omega, H)$ decrease monotonically with magnetic field, mirroring the $\rho_s(H)$ curve. Thus, the high-frequency SW transfer (the difference between ρ_s and $\Delta N_{T_c}(\Omega_c, H)$) is not entirely suppressed in the superconducting state. Rather, it is gradually diminished, trending toward zero along with the superconducting order parameter. This behavior continues at higher temperatures for the y=6.75 crystal. The optimally-doped crystal again shows no SW anomaly, with $\Delta N_{T_c}(\omega, H) = \rho_s(H)$ at all fields, even as both are reduced. It should be noted that the field-dependence of the magnitudes of the changes for the y=6.95 crystal are somewhat extrapolation-dependent. However, their equality at all fields holds for any reasonable extrapolation.

The fundamental empirical difference between the results of the two orientations of the the magnetic field is the final destination of the SW which is removed from the superfluid density. For $H \parallel c$ the SW is returned to higher frequencies, thus implying that that the energy scale of the condensate formation evolves towards a BCS-like regime. Fields applied $H \parallel CuO_2$, on the other hand, reduce the high-frequency SW transfer proportionately to the superfluid density, maintaining a discrepancy between $\Delta N_{T_c}(\omega, H)$ and $\rho_s(H)$. This behavior suggests that the

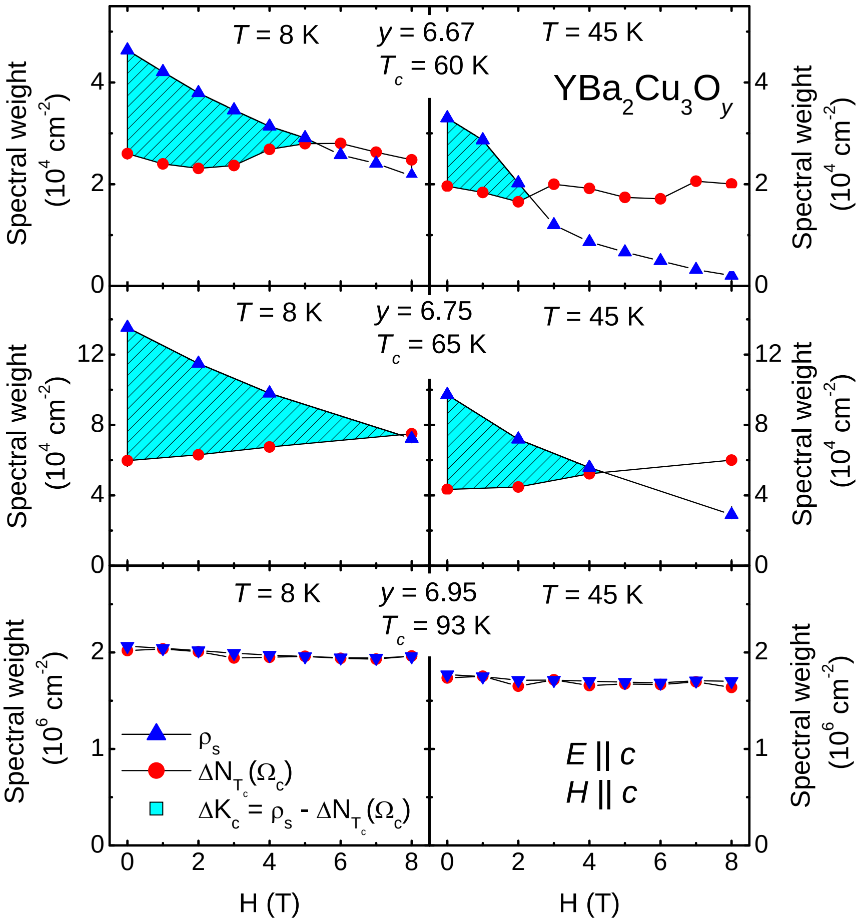

Figure 4.10: Comparison of spectral weight redistribution in c-axis magnetic field for YBa$_2$Cu$_3$O$_y$ at y=6.67 (top panel), 6.75 (middle), and 6.95 (bottom) doping levels and temperatures T=8 K (left) and 45 K (right). Circles represent the value of $\Delta N_{T_c}(\Omega_c,\, H)/\rho_s(0\mathrm{T})$ at cut-off frequencies $\Omega_c = 1000$ cm^{-1} for the underdoped crystals and $\Omega_c = 1300$ cm^{-1} for the optimally doped system. Triangles indicate total superfluid density at each value of magnetic field. High energy contributions (shaded regions) were inferred from $\rho_s - \Delta N_{T_c}(\Omega_c,\, H)$ and can be interpreted as kinetic energy change ΔK_c via Ref. (86).

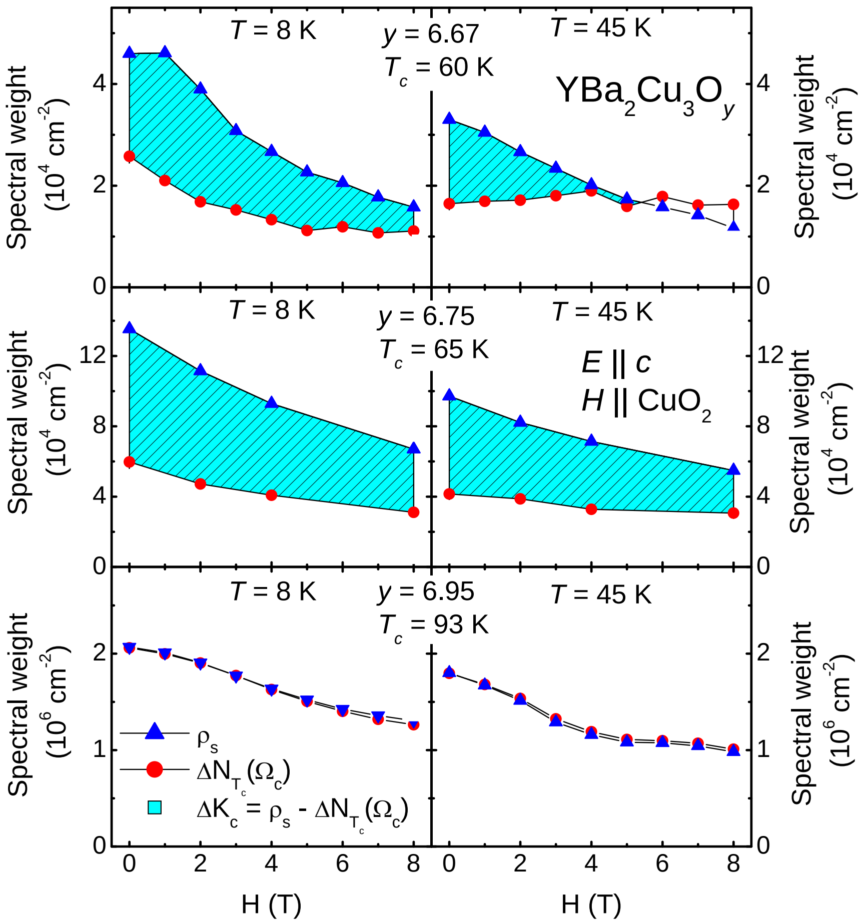

Figure 4.11: See caption for Fig. 4.10. Magnetic field is applied parallel to CuO_2 planes.

mechanism of condensate formation involving transfer of SW from high frequencies remains intact for all values of magnetic field.

4.6 Vortex meandering and interlayer phase coherence

The dramatic change in the infrared response at relatively small fields $H \parallel c$ is surprising in several respects. Most notable are the modification of the SW redistribution scheme over an anomalously large energy scale, and the substantial (50%) reduction of superfluid density seen in underdoped samples at fields much smaller than the pairbreaking field (98; 99). Both of these effects may be consistent with a theoretical perspective involving the wandering of pancake vortices and the subsequent suppression of interlayer phase coherence (101; 102). In a layered type-II superconductor material with no disorder, it is known that pancake vortices will be well aligned along the c axis, maintaining phase coherence between adjacent planes. A disordered pinning potential, however, will produce a random displacement of vortices from layer to layer. As magnetic field is increased this pinning eventually destroys vortex lines and interlayer phase coherence. Since the interlayer phase difference $\phi_{n,n+1}$ is intimately related to the interlayer coupling J and superfluid density ρ_s ($J \propto J_0 cos(\phi_{n,n+1}) \propto \rho_s$) (101; 102), the effect is visible in the infrared data.

The finite interplane phase difference is central to of a model of bilayer dynamics proposed by Ioffe, Millis, and Shah (IMS) in which SW derived from energies far above $k_B T_c$ contributes to ρ_s (103; 104). High-energy SW transfer is expected within the IMS picture when the transition occurs between a normal state above T_c characterized by pairing, but no phase coherence, and a SC state with well-defined phase coherence. One can then extend this description to attribute the elimination of high-energy SW transfer to the competition between vortex meandering and restoration of interlayer phase coherence in magnetic field.

Similar shrinking of the energy scale for condensate formation is not seen in the $H \parallel CuO_2$ data, consistent with the above considerations of phase coherence.

The Josephson vortices created in this field geometry affect the phase of the superconducting order parameter in a more complicated way than pancake vortices do (47). Oscillations of the Josephson vortex lattice result in an interlayer phase relationship which is dynamic and highly frequency-dependent, a departure from the simple linear suppression of coherence expected for pancakes. Furthermore, additional complications arise in the analysis of the IR data obtained in this geometry due to the new resonances in the conductivity spectra which are produced by the motion of Josephson vortices. For vortex-dynamics-related features in $\sigma(\omega)$ the distinction between normal and superconducting SW is no longer as clear as in the zero-field data. Indeed, these resonances are believed to result from oscillations of Josephson vortices and therefore are of superfluid origin. Yet the features appear in the dissipative part of the conductivity at the expense of the suppression of the superconducting δ-peak. Since both the vortex resonance and the Josephson plasma resonance are modified significantly by magnetic field, the SW shifts and possible changes of kinetic energy may be related in a more subtle manner than this analysis allows. Regardless of these complications, the linear scaling of $\Delta N_{T_c}(\Omega_c)$ and ρ_s informs us that high-energy SW transfer is not as easily stifled by $H \parallel \mathrm{CuO_2}$.

Reflectance measurements were also recorded for both magnetic field geometries at temperatures just above the superconducting transition. In both cases no field-induced modifications to the infrared reflectance were observed within the signal to noise of our data. This result has important implications in relation to the subject of pre-formed pairing. In this theoretical description of the pseudogap, for temperatures between T_c and the pseudogap temperature T^*, Cooper pairs are believed to exist but do not have long-ranged phase coherence (112; 113). The null result above T_c is consistent with the preformed pairs picture since the primary action of magnetic field is to destroy phase coherence, rather than to break Cooper pairs. For this reason, the magnetic field only impacts the optics when phase coherence is appreciable, below T_c. As a result, features in the data which are connected to superconductivity but appear above T_c, such as the asymmetric mode, are not modified by field in this temperature range. It would be highly instructive to extend these measurements to higher magnetic fields to determine if the low-field trends are continued.

It should be noted that the kinetic energy change observed in c-axis polarized experiments is not a phenomenon constrained to the interplane conductivity. In fact, kinetic energy lowering at zero field is consistent with angle-resolved photoemission spectroscopy (ARPES) data measured with ab-face crystals (see Ref. (16) and references therein). ARPES measurements of underdoped cuprates at the anti-nodal [(π,0) and (0, π)] regions of k-space reveal indicators of quasiparticle coherence consistent with the IMS picture described above: coherence at temperaures below T_c, but not above (114; 115). Comparison of IR and ARPES data confirms that kinetic energy change only occurs when this pattern of coherence is observed. Since the c-axis electrodynamics are thought to be strongly determined by the properties of the Fermi surface at the anti-nodal regions, free of the strong nodal contributions inherent to the CuO_2 planes (116), interplane measurements are especially sensitive to modifications of kinetic energy. In this way, c-axis experiments can be regarded as a probe of superconductivity in the planes.

This study is not unique in its approach of using magnetic field to tune anomalous properties of the high-T_c superconductors. Recent transport measurements (117) of the normal state in overdoped $Tl_2Ba_2CuO_{6+x}$ have shown that magnetic field $H \parallel c$ can tune the ground state from non-Fermi Liquid to Fermi Liquid in the vicinity of a quantum critical point. This strong modification of the electronic structure by magnetic field points toward the important role which spin plays in this doped Mott insulator system, even far from the antiferromagnetic region of the phase diagram. Other interesting connections between spin and electromagnetic response were uncovered by magneto-optical studies (118) of $La_{2-x}Sr_xCuO_4$ in which c-axis magnetic fields were shown to promote antiferromagnetism in the CuO_2 planes.

Conclusion

The primary finding of this work is that the application of an external magnetic can initiate profound redistribution of spectral weight from the superfluid density to the finite-frequency spectrum. The character of these effects differs depending on the orientation of the field with respect to the CuO_2 planes. Fields $H \parallel c$ return weight to high-energy regions of the spectrum, undoing the lowering of kinetic energy observed at zero field. Fields $H \parallel CuO_2$ place the weight at frequencies on the order of the superconducting gap, maintaining the reduction of kinetic energy. Since it is possible to reduce the interlayer phase coherence to the point where high-energy spectral weight transfer ceases, but a robust superconducting state remains, we must conclude that the reduction of kinetic energy seen at zero field is not a necessary condition for superconductivity. The importance of the phase coherence to this process is supported by the data for fields $H \parallel CuO_2$; these fields are less destructive to the interlayer phase relationship and leave intact the kinetic energy reduction intact.

Acknowledgments

This research was supported by NSF DMR 0705171. Y. A. was supported by KAKENHI 19674002 and 20030004, as was K. S. by KAKENHI 20740196.

Chapter 4, in full, is a reprint of the material as it appears in Phys. Rev. B. **79**, 104516 (2009). A. D. LaForge, W. J. Padilla, K. S. Burch, Z. Q. Li, A. A. Schafgans, Kouji Segawa, Yoichi Ando, and D. N. Basov. The dissertation author was the primary investigator and author of this paper.

Chapter 5

Infrared perspective on Fermi surface reconstruction in magnetic field

Abstract

We present an analysis of infrared optical and magneto-optical conductivity data for a range of underdoped cuprate superconductors including $YBa_2Cu_3O_y$ and $La_{2-x}Sr_xCuO_4$. In light of recent experiments which have been interpreted in terms of Fermi surface reconstruction in magnetic field, we search for far-infrared signatures of field-induced coherent electron pockets. By analyzing the effect of low-frequency spectral weight upon the complex conductivity, we are able to place limits on the oscillator strength of field-induced coherent pockets in the Fermi surface. In underdoped $La_{2-x}Sr_xCuO_4$ we observe a complete suppression of low-frequency spectral weight, indicating that no coherent contribution exists.

5.1 Introduction

The high-temperature copper-oxygen superconductors are reasonably well-understood on the edges of their phase diagram: an antiferromagnetic Mott insulator parent compound becomes, with doping, a metal. The ground state of the intermediate region, however, has thus far been more mysterious, especially in the underdoped region. In this part of the phase diagram, where stripe-ordered and pseudogap phases compete or cooperate with superconductivity, it was long uncertain whether a well-defined Fermi surface existed at all. In fact, most studies using angle-resolved photoemission spectroscopy (ARPES) have reported disconnected Fermi arcs (119; 120), rather than closed pockets (121). In-plane optical measurements (**E** polarized parallel to the CuO_2 planes) have revealed a nodal metal state with behavior resembling a Fermi liquid (122). Further complicating the situation is a partial suppression of the density of states, or pseudogap, in the antinodal region of reciprocal space (9; 10). The pseudogap is seen in ARPES measurements and also in the interplane (*c*-axis) conductivity, since the interlayer dynamics are dominated by antinodal states (116).

In the last several years breakthrough experiments (123; 124; 125; 126) have identified quantum oscillations in the transport and magnetization properties in underdoped $YBa_2Cu_3O_y$ (Y123) and $YBa_2Cu_4O_8$ (Y124), as well as in the electron-doped material $Nd_{2-x}Ce_xCuO_4$ (128), providing firm evidence of quasiparticles with closed fermi-surface orbits. The data from these high-field experiments, along with probes of the Nernst and Hall effects (127), have been interpreted as a density wave-driven reconstruction of the Fermi surface from large hole sheets to small electron and hole pockets, with electron pockets playing a dominant role in the transport (129; 130; 131). These observations may move us closer to understanding the underdoped region of the cuprate phase diagram, but they also open new questions involving the nature of the reconstruction, its relationship with the ground state properties of underdoped cuprates in the absence of the magnetic field, as well as the mapping of the FS in *k*-space.

Most theoretical attempts at explaining the magneto-oscillation data postulate the formation of electron pockets in the antinodal regions (See refs. (129) and (130), for example). Recently, however, some of us postulated an argument against the notion of coherent antinodal states at moderate fields (132). There we presented ARPES data (133; 134) which document a large antinodal gap in the density of states, as well as c-axis transport data which is consistent with the gap surviving in moderate magnetic fields. We showed that since the electron-like behavior cannot be explained in terms of normal-state carriers, some other explanation, such as superconducting fluctuations, is necessary. In this article we further address this important issue by discussing the infrared magneto-optical properties of two relevant classes of materials: $La_{2-x}Sr_xCuO_4$ (LSCO) near $x = 1/8$, and underdoped Y123. In the former, reconstruction of the Fermi surface is likely and stripe-like magnetic order is known to be induced by weak magnetic fields (151); the latter is the system in which the vast majority of quantum oscillation observations have been made. We critically assess the issue of a coherent contribution to the c-axis conductivity implied by a small pocket of light quasiparticles in the antinodal direction.

The essential capability of infrared spectroscopy is the determination of the dynamic optical constants, including the optical conductivity $\hat{\sigma}(\omega) = \sigma_1(\omega) + i\sigma_2(\omega)$. This comprehensive probe of the response of an electronic system yields an intuitive and quantitative description of its excitation spectrum. The presence of a Drude component (Lorentzian mode centered at zero frequency) in $\sigma_1(\omega)$ is a signature of coherent quasiparticles. Since the interplane conductivity is dominated by states in the antinodal region of k-space (116; 135; 16; 136), any reconstruction of the Fermi surface which produces coherent antinodal quasiparticles is expected to introduce a Drude signature into the interlayer optical conductivity, visible as an upturn at low frequencies. This direct examination of $\sigma_1(\omega)$ is complemented by a separate technique that infers spectral weight information from the imaginary part of the conductivity, $\sigma_2(\omega)$. Therefore, c-axis magneto-optical measurements are ideally suited to observe coherent quasiparticles due to magnetic field-induced fermi surface reconstruction.

Through considerations of the low-frequency optical response we are able to place limits on the spectral weight associated with reconstructed Fermi pockets. In underdoped samples of LSCO no new mode is directly observed, and less than 7% of the spectral weight from the low-temperature superconducting condensate is available for the creation of a coherent free carrier mode. Similar limits are established for underdoped Y123 in magnetic field. We will also discuss these magneto-optical data in the context of the interlayer electrodynamics of $\mathrm{La}_{2-x-y}\mathrm{Sr}_x(\mathrm{Nd, Eu})_y\mathrm{CuO}_4$ (148), where stripe order is firmly established but does not lead to the appearance of c-axis coherence.

5.2 Experimental details and results

Interplane reflectance measurements in magnetic field were performed for two prototypical high-T_c cuprate families, Y123 and LSCO. Sample growth and transport characterization are described in Refs. (92) and (41) and details of the magneto-optical experiment can be found in Refs. (110), (137), and (138). Infrared reflectance was measured over a wide frequency range (18-40 000 cm^{-1}) in magnetic fields $H = 0 - 8$ T applied parallel to the c axis. In all measurements the electric field of the incident light was also polarized parallel to the c axis to isolate the interplane response.

5.2.1 Raw reflectance

Infrared reflectance $R(\omega)$ is plotted in Fig. 5.1 for underdoped crystals $\mathrm{La}_{1.90}\mathrm{Sr}_{0.10}\mathrm{CuO}_4$ (LSCO 0.10, Fig. 5.1a), $\mathrm{La}_{1.875}\mathrm{Sr}_{0.125}\mathrm{CuO}_4$ (LSCO 0.125, Fig. 5.1b), and $\mathrm{YBa}_2\mathrm{Cu}_3\mathrm{O}_{6.67}$ (Y123 6.67, Fig. 5.1c). The latter sample represents a hole doping value not far from those where quantum oscillations have been observed (139) in the transport properties of Y123 ($y = 6.67$ corresponds to a hole doping value of approximately 0.12). All crystals exhibit “insulating” behavior at temperatures $T \gtrapprox T_c$, with low, mostly flat $R(\omega)$. Thus raw $R(\omega)$ data are in stark conflict with the notion of a coherent quasiparticle contribution in the antinodal region in the normal state. We will further elaborate on this point when analyzing the complex conductivity plotted in Fig. 5.2. Below T_c the interplane coherence of the superconducting phase allows Cooper pairs to oscillate freely between layers, producing the sharp reflectance edge of the Josephson plasma resonance (JPR). As magnetic field H is applied perpendicular to the planes, phase coherence is diminished. The JPR is suppressed, broadening and moving to lower frequencies.

For the LSCO crystals, the response returns to that of the normal state, suggesting that the Josephson coupling of CuO_2 has been arrested. For Y123, field magnitudes of 8 T cause the spectra at 8 K to resemble that of $T = 45$ K and zero field.

5.2.2 Optical conductivity

As pointed out above, the most straightforward approach for detecting coherent charge dynamics is the direct observation of a Drude feature in the dissipative part of the optical conductivity $\sigma_1(\omega)$. In Fig. 5.2 (a-c) we plot $\sigma_1(\omega)$ for the same crystals as in Fig. 5.1, calculated from the reflectance via the Kramers-Kronig relations. At room temperature $\sigma_1(\omega)$ consists of several strong phonons superimposed upon a nearly frequency-independent electronic background. At temperatures below $T = T^* > T_c$ we observe the dramatic suppression of low-frequency conductivity due to the pseudogap (PG) (9; 140; 141; 13) . The PG is only a partial gap, with finite residual conductivity remaining below the gap frequency. The spectral weight missing from the gap is transferred to higher energies, above the high-energy cutoff of the data. Upon entering the superconducting state the LSCO crystals experience a montonic decrease of conductivity at low frequencies as spectral weight is transferred to the superfluid density, represented by a $\delta(\omega)$ peak at zero frequency. For Y123 the presence of the bilayer plasmon feature near 400 cm^{-1}, which is coupled to several c-axis phonons, produces a more complicated spectrum (23; 95). However, a similar condensate formation is observed.

Empirically, the application of magnetic field $H \parallel c$ serves to undo the effect of lowering temperature, driving the conductivity toward the normal state spectra. One common characteristic of the magneto-optical response of the three representative data sets displayed in Fig. 5.2 is that no new Drude-like absorption feature is observed. The conductivity of the LSCO 0.125 and Y123 6.67 crystals are flat at lowest frequencies. The LSCO 0.10 sample does exhibit an upturn of conductivity toward low frequencies, but it is clear in this case that we are witnessing a return of the conductivity to its normal state value, and not the

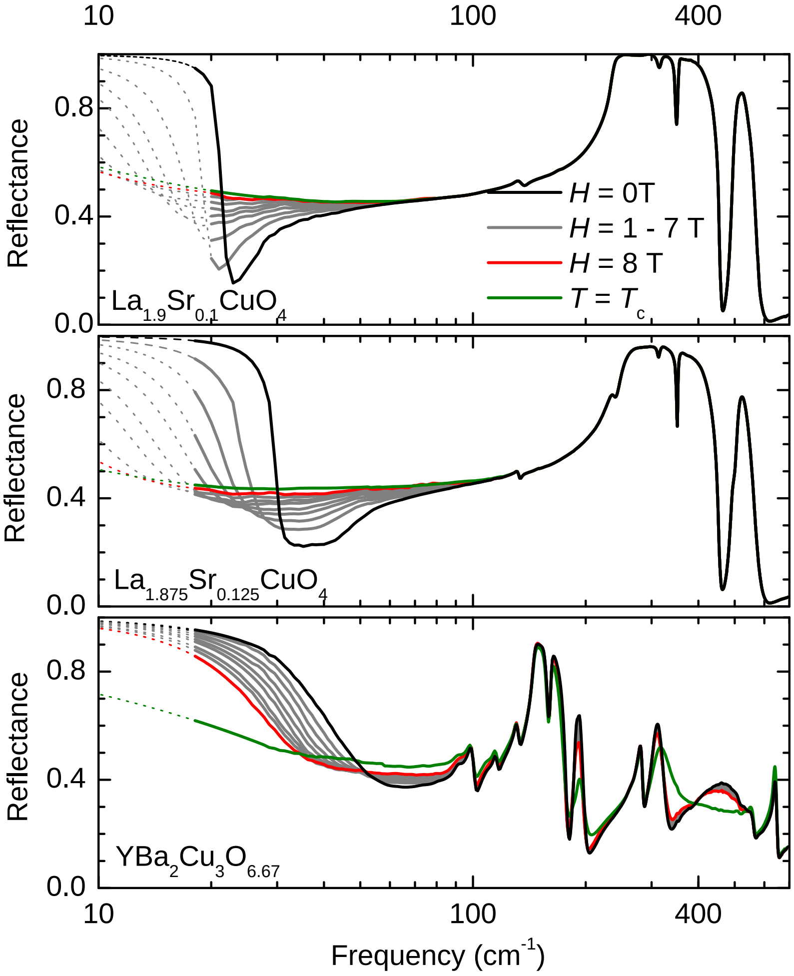

Figure 5.1: Optical reflectivity $\sigma_1(\omega, H)$ of $\mathrm{YBa_2Cu_3O_{6.67}}$ and $\mathrm{La_{1.90}Sr_0.10CuO_4}$ single crystals at T_c, and at 8 K for magnetic fields up to 8 T.

emergenece of a new coherence peak indicative of new pockets in the Fermi surface. The reversion to the normal state response is especially clear in the raw reflectance data in Fig. 5.1.

If an emergent coherent mode had narrow width relative to the low-frequency experimental cutoff (20 cm^{-1}), then its contribution would be difficult to resolve in $\sigma_1(\omega)$, even if the lower-frequency response exhibited a marked upturn. In this case we are aided by the fact that the optical constants in the frequency range where data exist are sensitive to spectral weight at lower frequencies. This consequence of the Kramers-Kronig (KK) relations is often exploited to measure the superfluid density in superconducting materials (5). Any coherent mode ($\delta(\omega)$-peak or narrow Lorentzian resonance) appearing below the low-ω cut-off results in a $1/\omega$ behavior of the imaginary part of the conductivity. In the raw reflectance data this mode yields a sharp plasma edge form of $R(\omega)$. Therefore $\sigma_2(\omega)$ spectra along with raw reflectance data allow us to comment on the possibility of a coherent mode in the c-axis response.

5.2.3 Spectral weight

Given this sensitivity to both Cooper pair and quasiparticle coherence, the coefficient of the $1/\omega$ contribution to $\sigma_2(\omega)$ (defined more generally as $\Sigma_{LF} = \rho_s + \Sigma_{QP}$) is the sum of the spectral weights of the superfluid and the coherent quasiparticle peak. As shown in Fig. 5.3 for LSCO 0.10, the low-frequency level of $\pi\omega\sigma_2(\omega)$ indicates the value $\Sigma_{LF}(H)$. The values of $\Sigma_{LF}(H)$ are displayed for each sample in the righthand column of Fig. 5.2. Consistent with the behavior of the JPR in the raw reflectance data, Σ_{LF} is completely suppressed (within detection limits of 5 %) by 8 T in both LSCO crystals. This unambiguously shows that all spectral weight from the c-axis condensate is transferred out of the low frequency part of the spectrum, leaving no room for the formation of a coherent quasiparticle peak.

For the Y123 crystal it is possible to place bounds on the expected infrared response based on the results of the magneto-oscillation experiments. The Drude linewidth is equal to the scattering rate $1/\tau$, which is dependent upon disorder and

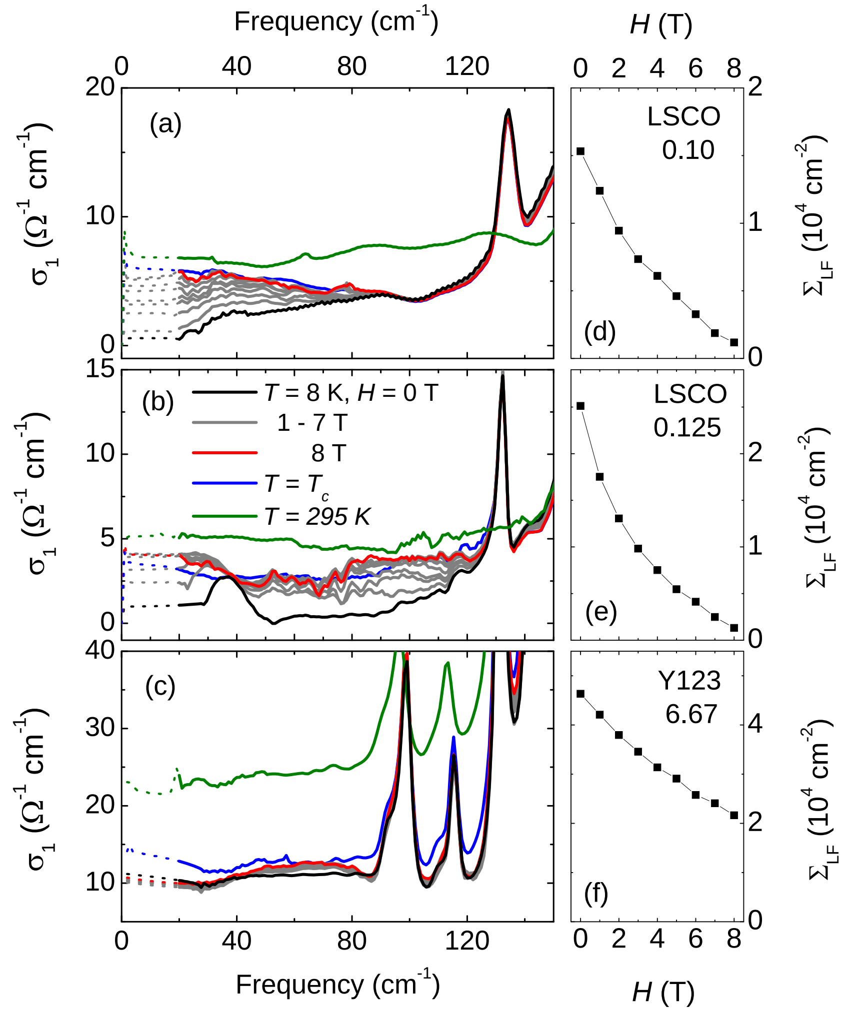

Figure 5.2: (a) Optical conductivity $\sigma_1(\omega, H)$ of $YBa_2Cu_3O_{6.67}$ and $La_{1.90}Sr_0$.10CuO_4 single crystals at T_c, and at 8 K for magnetic fields up to 8 T. (b) Superfluid density ρ_s, as determined from $\sigma_2(\omega)$.

temperature. $1/\tau$ for Y123 may be deduced from the magneto-oscillation experiments by considering the fundamental condition for the realization of quantum oscillations: $1/\tau < \omega_c = \frac{eH}{cm^*}$, where ω_c is the cyclotron frequency and e and m^* are the electron charge and effective mass, respectively. The smallest field at which oscillations have been reported is 30 T; inputting the effective mass $m^* = 1.76$ determined in the same study (125) yields a lower bound on $1/\tau$ of $\omega_c = 15$ cm^{-1}. As discussed above, no feature consistent with this estimate of scattering rate is observed in our data. It is clear that for scattering rates compatible with the cyclotron resonance conditions, the conductivity contains no infrared signature of coherent antinodal quasiparticles.

Considering the low-frequency spectral weight for Y123 6.67, it is shown in Fig. 5.2(f) that the application of an 8-T magnetic field reduces $\Sigma_{LF}(H)$ by 50% . Since independent data for the magnetic field-dependent c-axis superfluid density are not available, we are unable to discern between the two possible contributions to $\Sigma_{LF}(H)$. Instead we may place limits upon the allowed quasiparticle weight $\Sigma_{QP} \leq \Sigma_{LF}$. If new coherent pockets were being populated through pair-breaking processes, then the transfer of spectral weight from the superconducting condensate to the narrow Drude-like mode would occur at very low energies, and Σ_{LF} would have no magnetic field dependence. Instead, we observe in our data a transfer of spectral weight out of the low-energy region. The linear suppression of Σ_{LF} is in agreement with a fairly straightforward model involving the misalignment of pinned vortices (101; 102). Since the rate of suppression is in fact slightly faster than predicted for reasonable material parameters for Y123, the transfer of spectral weight to a narrow Drude-like mode seems unlikely.

It is well known that the incoherent c-axis response of underdoped cuprates is a consequence of the pseudogap (2). One can therefore speculate that the formation of interplane quasiparticle coherence would require diminishing of the pseudogap. However, our data exhibit no sign of pseudogap suppression. Closing of the pseudogap with magnetic field has been observed in transport experiments, but only for thin films (142) or very large fields (143) (much larger than those accessed in this work). In tunneling transport measurements, even pulsed magnetic fields

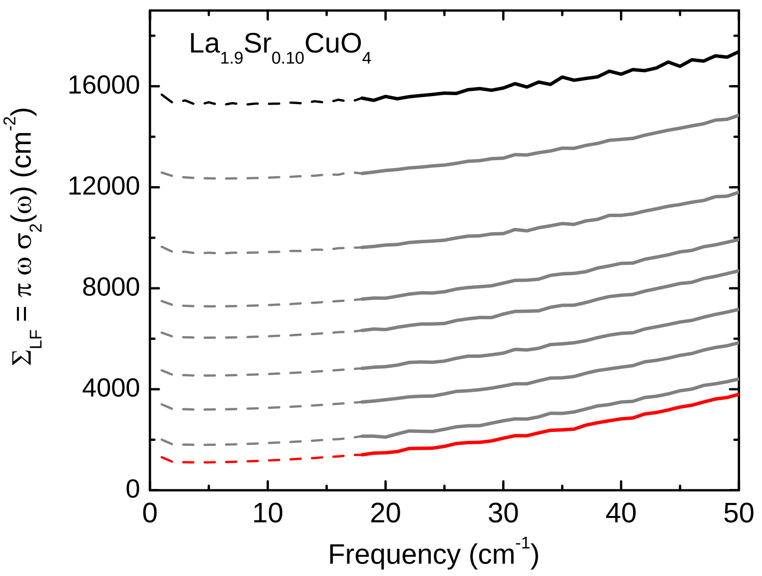

Figure 5.3: Magnetic field dependence of low-frequency spectral weight Σ_{LF} as determined by $1/\omega$ contribution to σ_2.

of the order of those used in magneto-oscillation experiments do not suppress the pseudogap (144).

5.3 Discussion

The reduction of the *c*-axis superconducting phase coherence in underdoped LSCO is best understood within the picture of the stripe-like order, a scenario that also has been hypothesized to explain the quantum oscillations data (145; 138). Therefore it may be instructive to examine the *c*-axis electrodynamics of other stripe-ordered materials. Important examples of density-wave states competing and coexisting with superconductivity are realized in $La_{2-x-y}Sr_x(Nd, Eu)_yCuO_4$ and $La_{1.875}Ba_{0.125}CuO_4$. Optical studies of rare earth-doped LSCO revealed dramatic suppression of the JPR frequency, signaling the decoupling of CuO_2 planes (148). This interplane decoherence coincides with the onset of stripe order and a structural transition to a low-temperature tetragonal configuration. These combined observations offer a window into the underlying physics: when lattice distortions provide a sufficient pinning potential for collective stripe pinning, stripe order is stabilized at the expense of interlayer phase coherence. As the doping corresponding to the strongest stripe order is approached, the JPR minimum is broadened by incoherent processes (57), and is eventually suppressed completely. The severely diminished oscillator strength of the c-axis plasmon places a strict limit on the available spectral weight for coherent transport.

A similar situation is encountered at the $x = \frac{1}{8}$ doping level of $\mathrm{La}_{2-x}\mathrm{Ba}_x\mathrm{CuO}_4$, a material so dominated by stripe order that its bulk T_c is suppressed to < 5 K . Optical measurements showed the c-axis response of this system to be very insulating, with low-frequency conductivity levels below 1 $\Omega^{-1}\mathrm{cm}^{-1}$ and no Drude-like upturn or Josephson plasmon, again placing an upper bound on the size of a coherent peak (149). Recent ARPES and transport experiments have yielded further insight into the k-dependence of the quasiparticle dynamics; correlations between the opening of the d-wave-like gap at the Fermi surface and the abrupt cessation of negative thermopower indicate that the available quasiparticle states in that system are located in the near-nodal region, and not at the antinodes (133; 134; 132). Also, reports of insulating c-axis resistivity in high magnetic field (150) agree with the non-metallic response observed by optical techniques.

There are, of course, several discrepancies in experimental conditions between the optical measurements desribed here and the observations of magneto-oscillations. However, these differences should not be significant enough to completely obsure the signatures of quasiparticle coherence in the infrared conductivity. For example, the transport experiments were conducted in extreme regions of the temperature/magnetic field parameter space which are presently inaccessible to magneto-optical techniques: the magnetic field scale accessed in the optics data (8 T) is only a fraction of that for which oscillations were discovered (50 T). Yet, the 8-T field does produce dramatic modifications to the interplane response. In underdoped LSCO it has been shown that induced static magnetic order plays a significant role in the complete suppression of superfluid density mentioned above, leading to a regime of two-dimensional superconductivity (138). For underdoped Y123 crystals the halving of the superfluid is accompanied by a modification of the condensate formation scheme over a wide energy scale (110; 137), as well as by the enhancement of static incommensurate magnetic order (152).

An additional difference lies in the precise chemical compostion of crystals studied: quantum oscillations have only been observed for extremely clean crystals with dopings near $p = 0.10$ in $YBa_2Cu_3O_y$ and at $p = 0.125$ in $YBa_2Cu_4O_8$, and never in $La_{2-x}Sr_xCuO_4$. However, the doping of $YBa_2Cu_3O_y$ presented here (p=0.12) lies in the doping interval bounded by the above results. And although LSCO crystals are generally too disordered to permit observation of magneto-oscillations, the conditions for observing coherence are more easily satisfied in IR optics than in other techniques. For instance, IR measurements can easily detect a Drude response in dirty metals which would never exhibit quantum oscillations.

It should be noted that incoherent interlayer transport is not a generic feature of anisotropic, strongly correlated electronic systems. For example, the layered ruthenate Sr_2RuO_4 is anisotropic by approximately three orders of magnitude, yet displays coherence along all three crystal axes. This is evidenced by T^2 temperature dependence of both ab-plane and c-axis resistivity at low temperatures (153), as well as by the presence of a low-frequency plasma edge in the infrared reflectance (154). These observations are indicative of Fermi-liquid-like electron-electron scattering, and Drude-like contribution to the conductivity, respectively, in stark contrast with the incoherent behavior of the cuprates discussed here.

The analysis of optical conductivity data in magnetic field has been shown to be a insightful tool for probing the coherence of antinodal quasiparticles. Like transport, optics is a bulk probe, which broadens its applicability and reliability. The limits placed on the possible reconstructed Fermi pockets should be useful for guiding future theoretical efforts, especially in conjuction with ARPES and transport results.

Acknowledgments

This research was supported by NSF DMR 0705171. Y. A. was supported by KAKENHI 19674002 and 20030004, as was K. S. by KAKENHI 20740196.

Chapter 6

Optical characterization of Bi_2Se_3 in magnetic field: searching for topological insulators in the infrared

Abstract

We present an infrared magneto-optical study of the highly thermoelectric narrow-gap semiconductor Bi_2Se_3. Far- and mid-infrared (IR) reflectance and transmission measurements have been performed in magnetic fields oriented both parallel and perpendicular to the trigonal c axis of this layered material, and supplemented with UV-visible ellipsometry to obtain the optical conductivity $\sigma_1(\omega)$. With lowering of temperature we observe narrowing of the Drude conductivity due to reduced quasiparticle scattering, as well as the increase of the band gap absorption edge. Magnetic fields $H \parallel c$ dramatically renormalize and assymetrically broaden the strongest far-IR optical phonon, indicating significant coupling to the continuum free-carrier spectrum. For the perpendicular field orientation, a new far-IR absorption is observed, and the plasma edge is slightly shifted to higher energies. In both cases the band gap edge is softened in magnetic field.

6.1 Introduction

Since the first synthesis of Bi_2Se_3 in the late 1950s (155), a rich body of theoretical and experimental work has grown out of the effort to explain and exploit the large thermoelectric effect which the material exhibits (156). Recently this compound was vaulted back into the forefront of the condensed matter field after being named a prime candidate for the physical realization of topological surface states (157). A topological insulator has an energy gap in the bulk but, due to spin-orbit coupling, possesses one or more robust metallic surface states which are protected by time-reversal symmetry. So far, the only three-dimensional material to exhibit this behavior is the alloy Bi_xSb_{1-x} (158). Recent band structure calculations (157), however, predict that Bi_2Se_3 and several related layered compounds should exhibit a single Dirac cone on the Fermi surface, a hallmark of a topological insulator. Beyond the inherent importance of exploring a new phase of quantum matter, these systems are of great interest for device applications involving quantum computing (159) and photonics (160), the latter due to nonlinear electron-phonon interaction effects.

Here we present an infrared spectroscopic study of Bi_2Se_3 in magnetic field. The original motivation for this work was to search for signatures of the topological insulator state, a proposal with two-fold justification. First, the topological nature of such a material is theorized to be sensitve to the application of electromagnetic fields (161; 162), and such a tuning of the surface states may display a spectroscopic signature. Second, the magnetic field allows the probing of band dispersion via the cyclotron resonance. As mentioned above, a defining characteristic of the topological surface state is the existence of an odd number of Dirac cones at the Fermi surface (157), which in turn prescribes the presence of massless Dirac fermions moving at the Fermi velocity. Such quasiparticles can be detected by angle-resolved photoemission spectroscopy (163; 164), or alternatively by measurement of the cyclotron resonance. In the latter, optical or tunneling spectroscopy techniques measure transitions between Landau levels in an applied magnetic field, and massless quasiparticles are distinguished from massive ones by their square-root, rather than linear, dependence of transition energy upon magnetic field (165). Thus, infrared magneto-spectroscopy is an ideal tool for probing the topological insulator quantum state.

As we will show below, the doping of the sample under investigation was found to place the Fermi surface away from the Dirac cone, precluding the formation of topological surface states. However, the remarkable field-induced effects uncovered by this study, including broad transfer of spectral weight and strong electron-phonon coupling, demonstrate the intrinsic complexity of the host material and set a baseline against which future samples in the topological phase may be compared.

Bismuth selenide (Bi_2Se_3), a member of the V_2VI_3 group of materials (V= Bi, Sb, S; VI = Se, Te, S), crytallizes in a rhombohedral structure (point group $\bar{3}mD_3d$) (155). Five-atom layers, known as quintuple layers, are oriented perpendicular to a trigonal c axis, and the covalent bonding within each quintuple layer is much stronger than weak van der Waals forces bonding neighboring layers. Due to selenium vacancies the material is easily n-doped over a wide range of carrier concentrations (166; 167), but has recently been p-doped as well (168). Transport and optical experiments (155) have determined the semiconducting gap to be approximately 0.25-0.35 eV, in good agreement with theoretical calculations (157). Further studies have investigated the details of the interband transitions (155; 169) and phonons (170), as well as characterized the doping trends with the substitution of Te, Sb (172), As (171), Fe (173), Mn (174) and other elements.

6.2 Magneto-optical experiment

6.2.1 Sample information

Single crystals of Bi_2Se_3 were prepared by melting stoichiometric alloys of high purity Bi_2Se_3 (99.999%) in a vacuum-sealed quartz tube (with diameter 1/4 in. or 3/8 in.). Typically the vacuum of the tube is about 6×10^6 Torr. The sealed sample was heated to 850° C and then cooled over a period of three days, from 850 to 650° C, and annealed at that temperature for a week. The sample was then slowly cooled to room temperature. Single crystals were obtained and could be easily cleaved from the boule. Transport measurements at room temperature determined a carrier density of 4×10^{18} cm^{-3} and resistivity of 1.04 mΩcm.

6.2.2 Experimental description

Infrared reflectance and transmission measurements were performed in a novel magneto-optical cryostat developed at UCSD. In this system a translator actuates a helium-flow cryostat through the side port of a split-coil superconducting magnet, yielding highly repeatable spectra in both the Faraday and Voight geometries. This arrangement places the sample in the magnet outer vacuum chamber, which effectively provides a cold trap and requires one less window than the traditional variable temperature insert configuration. Furthermore, an *in situ* gold coating apparatus permits the determination of absolute reflectance in magnetic field and corrects for any spurious effects due to field-induced misalignment.

Reflectance and transmission spectra were recorded at selected temperatures from 6-295 K and magnetic fields 0-8 T, over the frequency range 30-6000 cm^{-1}. For photon energies above the mid-infrared the reflectance data were supplemented with visible-UV ellipsometry up to 48 000 cm^{-1}. Magneto-optical experiments were performed by first measuring the sample reflectance relative to a reference mirror for all temperatures and magnetic fields of interest. Then the sample was coated with gold and the entire measurement was repeated. The data were augmented with appropriate low- and high-frequency extrapolations and transformed via the Kramers-Kronig (KK) relations to obtain the frequency-dependent optical constants, including the optical conductivity $\hat{\sigma}(\omega) = \sigma_1(\omega) + i\sigma_2(\omega)$ The ellipsometry technique provides a direct, model-independent measurement of the high-frequency optical constants, and serves as a constraint for extrapolations used in the KK calculation.

6.2.3 Transmission experiment

Transmission data for Bi_2Se_3 in zero magnetic field are diplayed in Fig. 6.1(a). The crystal is transparent only within a narrow band in the mid-IR extending from 470-2000 cm^{-1} at room temperature. The low-frequency absorption is indicative of free-carrier transport, while the high-frequency cutoff identifies the band gap absorption threshold. At lower temperatures the low-frequency transmission onset becomes very steep and the band-gap absorption edge moves to higher frequencies, as the obscuring effects of thermal level broadening are reduced. At 6 K the band gap edge lies at 2650 cm^{-1} = 0.329 eV. Application of magnetic field perpendicular to the trigonal c axis acts to undo the effects of lowering temperature. As seen in the transmission ratios $T(6\text{ K}, H)/T(6\text{ K}, 0\text{ T})$ in Fig. 6.1(b), transmittance decreases with field on both ends of the transmission window, particularly on the high-frequency side defined by the band gap edge. The inset to Fig. 6.1(b) records the value of the band gap at magnetic fields up to 8 T; a total shift of 3 cm^{-1} is induced.

6.2.4 Reflectance and optical conductivity in zero magnetic field

Reflectance data for Bi_2Se_3 in zero magnetic field are found in Fig. 6.2. At room temperature the spectrum is dominated by a plasma edge in the far-IR, corroborating the picture of free electron transport deduced from the transmission. As seen in Fig. 6.2(a), the plasma edge hardens upon cooling to 200 K, then moves to lower frequencies and sharpens as the temperature is decreased to 6 K. Phonon absorption features are observed near 61 cm^{-1} (α mode) and 133 cm^{-1} (β mode); both sharpen considerably at lower temperatures. These features are displayed in more detail in Fig. 6.3(a). In the mid-IR near 2400 cm^{-1}, a peak appears in the reflectance at low temperatures [Fig. 6.2(b)]. This phenomenon, known as the Burstein shift, marks the onset of direct, allowed interband transitions (175). A comparison of this peak frequency with the band gap energy determined from transmission (see Fig. 6.4) yields an agreement within roughly 10%. Reflectance data for the extended frequency range are shown in the inset to Fig. 6.2(b).

Figure 5(a) displays the real part of the optical conductivity $\sigma_1(\omega)$, obtained by Kramers-Kronig transformation of the reflectance. The free carrier response is plainly visible as a Drude oscillator (Lorentzian centered at zero frequency) which

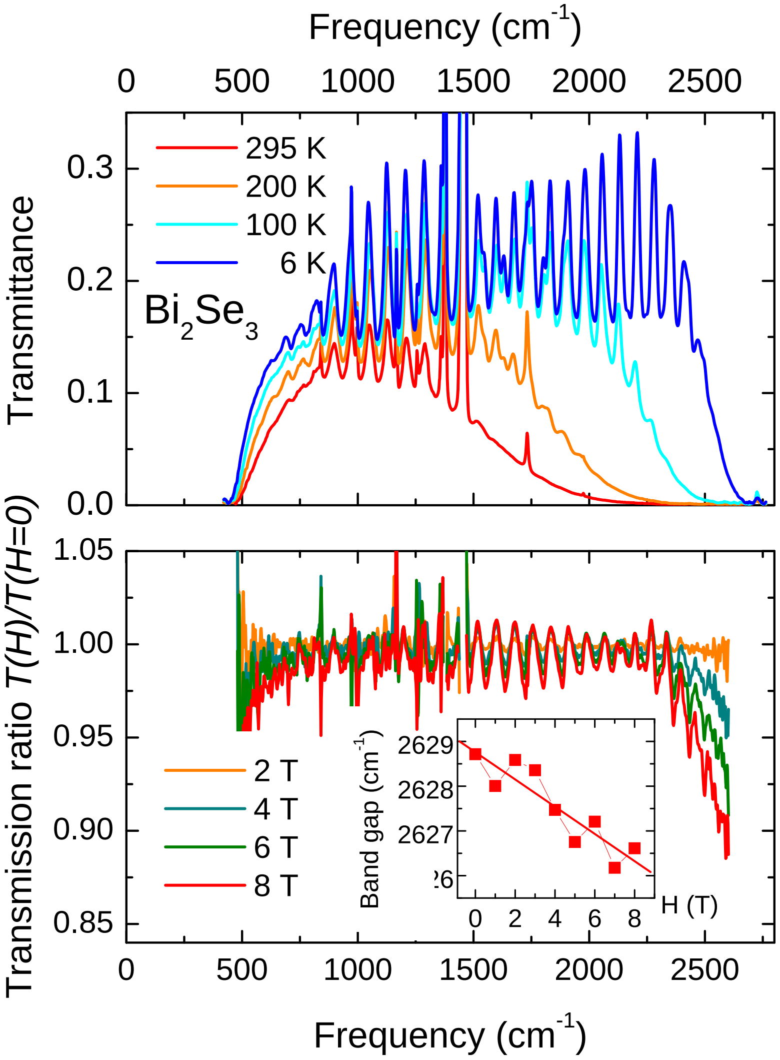

Figure 6.1: (a) Infrared transmittance of Bi_2Se_3 for a range of temperatures T=6-295 K. (b) Transmission ratios $T(6\text{K}, H)/T(6\text{K}, 0\text{T})$. Inset: suppression of band gap edge by magnetic field.

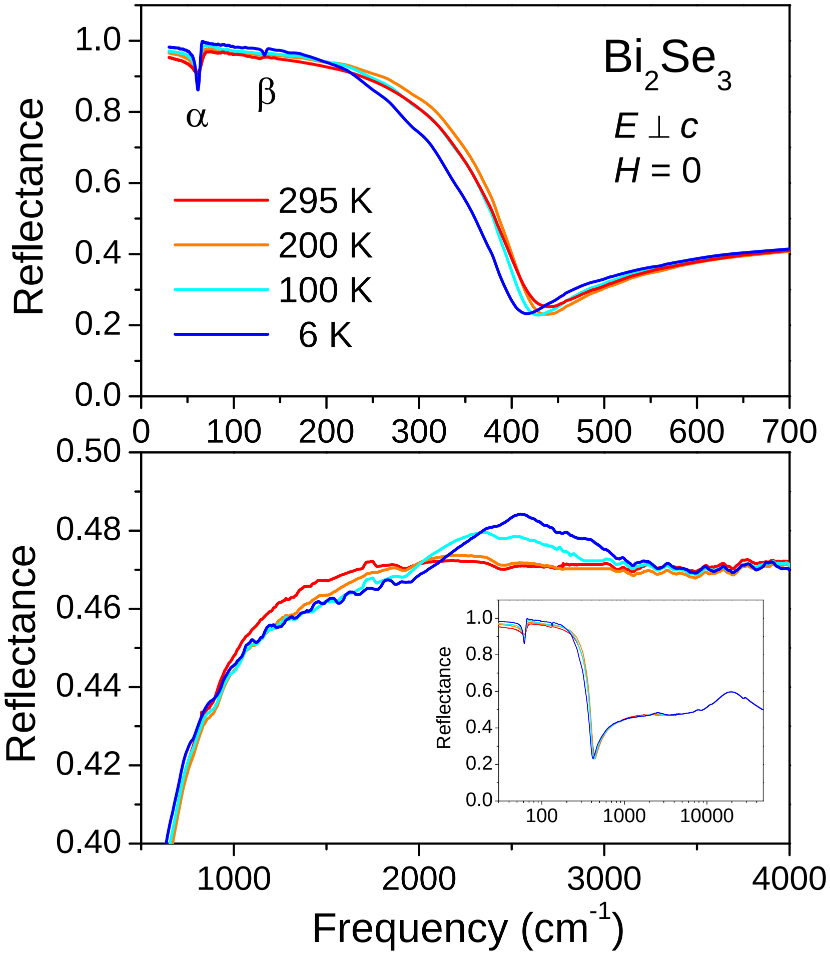

Figure 6.2: Infrared reflectivity of Bi_2Se_3 in zero magnetic field. The far-IR spectra (a) are characterized by a free-carrier plasma edge, as well as several phonon features. In the mid-IR range at low temperatures a peak develops near the band gap energy. Inset: Reflectance over the extended frequency range.

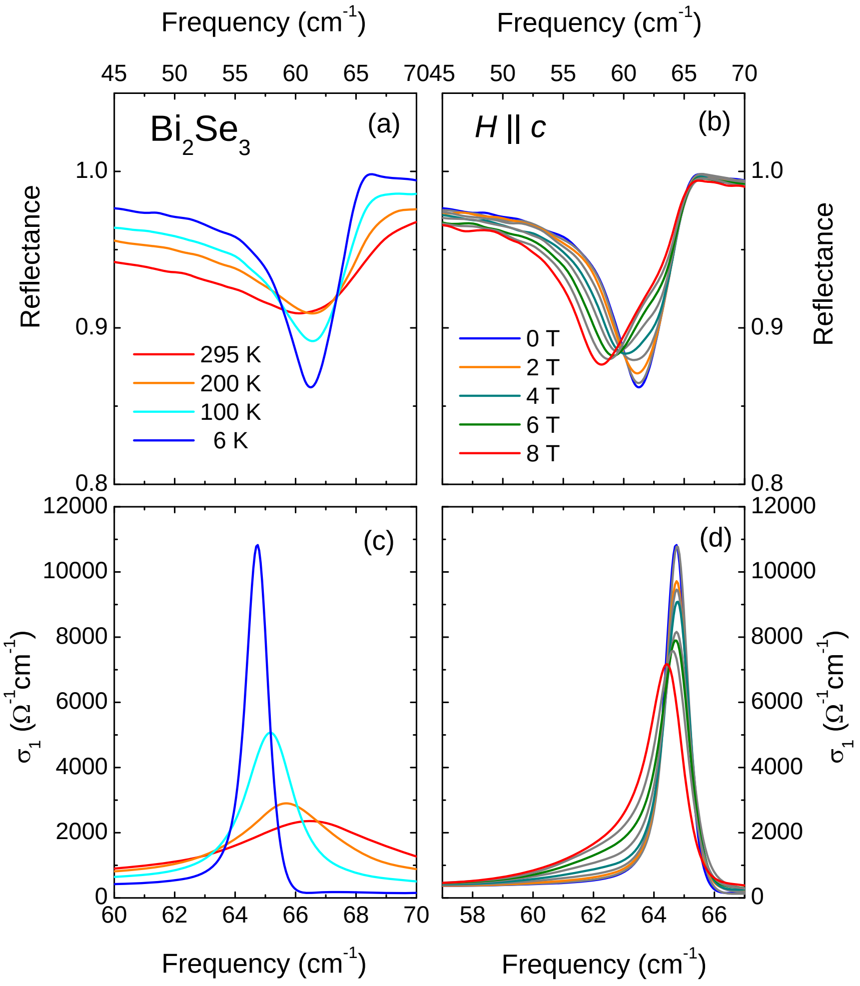

Figure 6.3: Infrared reflectance (top panels) and optical conductivity (bottom panels) for temperatures 6-295 K (left panels) and magnetic fields parallel to the c axis (right panels). The anomalously strong phonon is asymmetrically broadened in magnetic field.

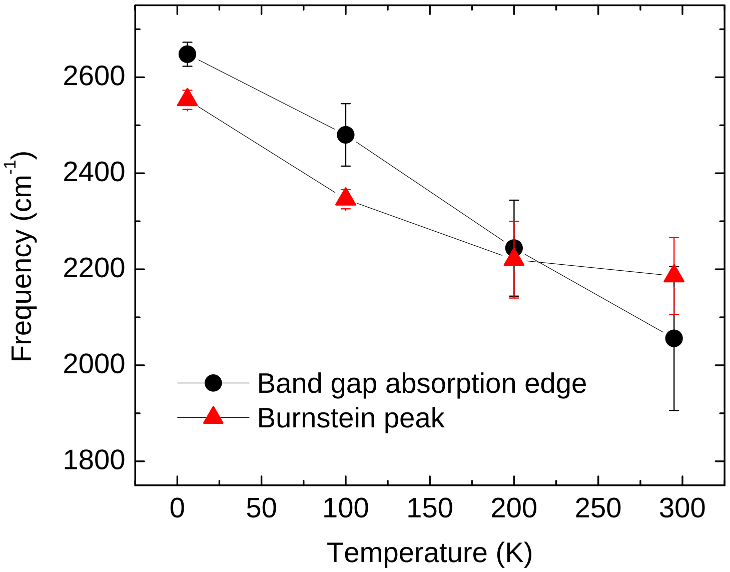

Figure 6.4: Band gap absorption edge and Burnstein peak frequencies as a function of magnetic field.

sharpens considerably with decreasing temperature. An oscillator fit reveals a collapse in the quasiparticle scattering rate, which experiences a three-fold decrease, from 60 → 22 cm^{-1}. This sharpening uncovers a broad mode (labeled here as γ) in the far-IR centered at $\omega_\gamma = 300$ cm^{-1}. The phonons also sharpen [Fig. 6.3(c)], as well as experience a shift of eigenfrequency: ω_β increases by 5 cm^{-1}, while ω_α anomalously decreases by 2 cm^{-1}. The α mode, which has previously been identified as having an oscillator strength much greater than theory would predict (170), exhibits an asymmetric Fano lineshape, and will be discussed in more detail in Section III. B. below. At higher frequencies, the Burstein shift causes a significant transfer of spectral weight from a gapped region spanning $1000 < \omega < 2500$ cm^{-1} to a peak at 3000 cm^{-1}.

6.2.5 Reflectance and optical conductivity in magnetic field

The application of magnetic field $H \parallel c$ initiates several distinct effects in the infrared response. Looking first at the reflectivity in Figs. 3(b) and 6(a), we

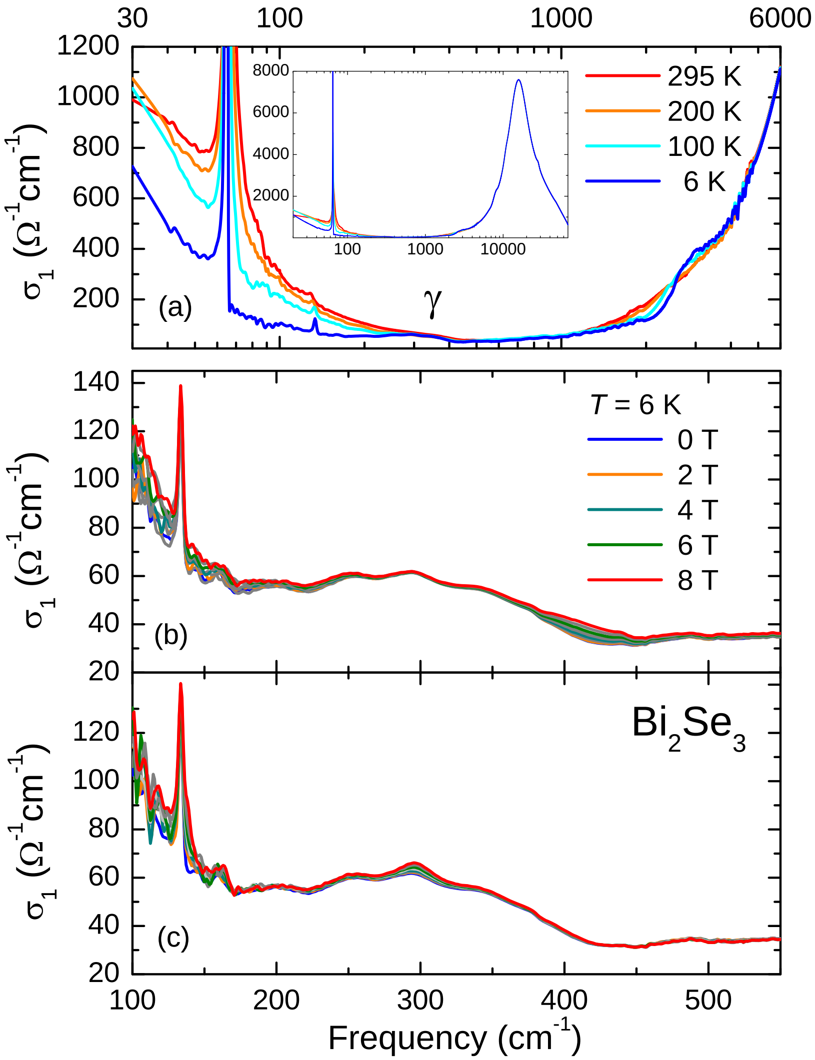

Figure 6.5: Optical conductivity $\sigma_1(\omega)$ for Bi$_2$Se$_3$ in zero magnetic field (a), as well for magnetic fields applied parallel (b) and perpendicular (c) to the trigonal c axis. Inset: Optical conductivity over a wide frequency range.

see that the absorption feature corresponding to the α phonon undergoes a shift to lower frequencies and a change in lineshape. At the same time, the reflectance in the plasma minimum is enhanced without changing the overall lineshape of the plasmon. The β mode is not modified by magnetic field, and no measurable change of reflectance occurs in the mid-IR. The optical conductivity spectra in field [Figs. 3(d) and 5(b)] exhibit an overall broadening of the Drude peak and γ mode. The Drude broadening is consistent with reports of positive magnetoresistance (172). They also illustrate more clearly the shift of the α phonon to lower frequencies and reveal that the mode is being asymmetrically broadened.

For the other revlavent magnetic field orientation, $H \perp c$, the changes in reflectance are much subtler. For this reason we show in Fig. 6.6 not only the absolute reflectance [Fig. 6.6(b)], but also the magnetic field ratios $R(6\text{ K}, H)/R(6\text{ K}, 0\text{ T})$ [Fig. 6.6(c)]. Viewing the ratios, it is clear that two distinct changes are promoted by the field: a reflectance dip at $\omega \approx 390$ cm^{-1}, and a shift of the plasma edge to higher frequency. The latter effect is shown in more detail in the inset to Fig. 6.6(b), and constitutes a total shift of $\Delta\omega_p \approx 1.5$ cm^{-1}. If we turn to $\sigma_1(\omega)$, shown in Fig. 6.5(c), it is apparent that the lower-frequency dip seen in $R(\omega)$ corresponds to an increase in the oscillator strength of the γ mode. This is in contrast to $H \parallel c$, which only increased the width of the γ mode. The α phonon mode experiences a minor reduction of oscillator strength, but no shift in frequency.

6.3 Analysis and discussion

6.3.1 Integrated spectral weight

A more comprehensive understanding of the evolution of the optical conductivity with temperature and magnetic field can be gained through examination of the integrated spectral weight $N(\omega) = \int_0^\omega d\nu\ \sigma_1(\nu)$. $N(\omega)$ is a measure of the total excitations occuring below frequency ω, and is useful for assessing the energy scales involved in electronic processes. Figure 7(a) displays the zero-field transfer of specral weight with temperature. Between $T = 295$ K and 200 K, the narrowing

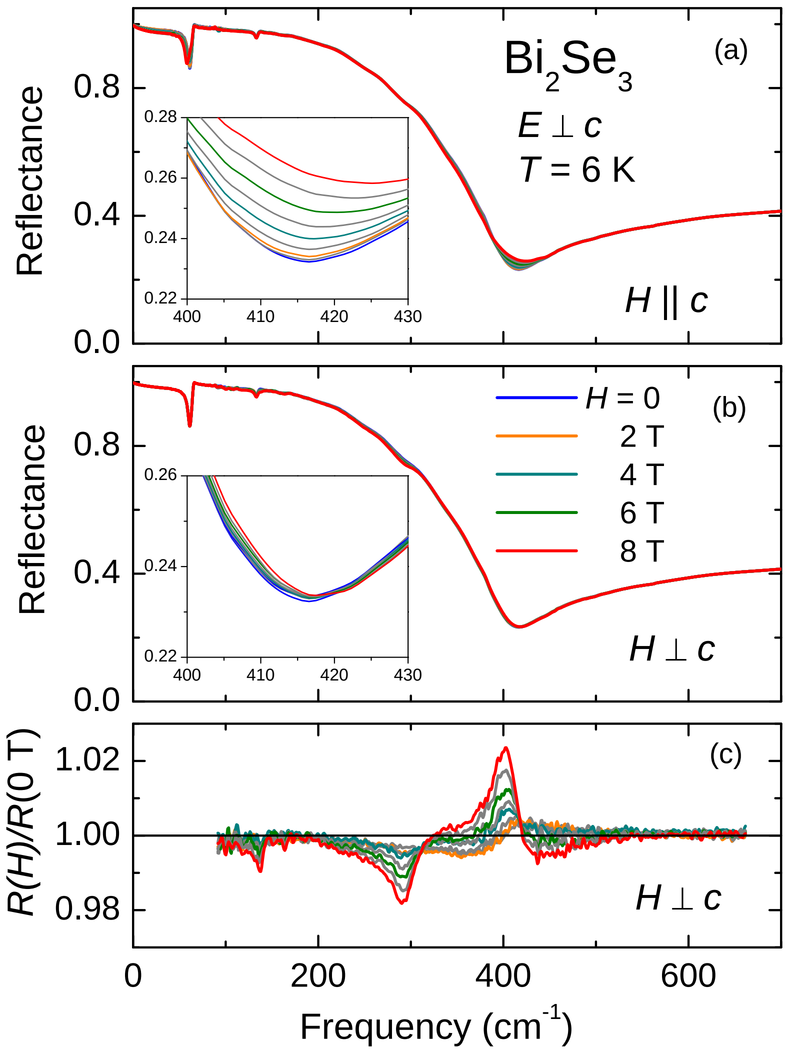

Figure 6.6: Infrared reflectivity of Bi_2Se_3 for magnetic fields applied parallel (a) and perpendicular (b) to the trigonal c axis. Also plotted (c) are the reflectance ratios $R(6\mathrm{K}, H)/R(6\mathrm{K}, 0\mathrm{T})$

of the Drude mode is accompanied by a modifcation of spectral weight over the entire far-IR, until the coherent weight is conserved near $\omega = 1000$ cm^{-1}. For 200 $\rightarrow$ 6 K, the low-frequency spectral weight is conserved below $\omega_\alpha \approx 64$ cm^{-1}, as evidenced by the convergence of the curves at that energy. For higher frequencies the gap in $\sigma_1(\omega)$ results in a redistribution of $N(\omega)$ up to $\omega = 4000$ cm^{-1}, where conservation of spectral weight is reached.

In the presence of an applied magnetic field the changes in spectral weight are mostly confined to a smaller energy scale, and involve a reshuffling of weight between the Drude, phonon, and γ modes. For $H \parallel c$ we observe in Fig. 6.7(b) a broadening of the Drude peak which is fully contained within 250 cm^{-1}. $N(\omega)$ is equal for all magnetic field values from 250-350 cm^{-1}, above which $N(\omega, 8\text{ T})$ increases slightly due to the high-frequency broadening of the γ mode. This anomalous spectral weight appears to have been transferred from the higher-energy portion of the spectrum, originating from undetectibly small changes of reflectance spread over a broad mid-IR frequency range. This phenomenon known to occur in other materials, including the cuprate superconductors (110). In fields oriented perpendicular to the c axis [Fig. 6.7(c)], very little modification of the Drude conductivity is observed. Instead, a small transfer of spectral weight occurs between the α phonon and the γ mode. This weight is largely regained by 500 cm^{-1}, but may extend slightly higher in frequency.

6.3.2 Evidence for electron-phonon coupling

It was noted in a previous optical study of the related compound Bi$_2$Te$_3$ (170) that the lowest-frequency infrared active phonon, analogous to the α mode at 64 cm^{-1} in Bi$_2$Se$_3$, displays an oscillator strength 60% greater than that predicted from a Born-van Karman lattice model. From this it was concluded that polarization effects must play a large role in the movements of the VI$^{(2)}$ atoms. Furthermore, it is clear from examination of the conductivity spectra in Fig. 6.3(d) that the phonon lineshape is strongly asymmetric, a signature of electron-phonon coupling and Fano physics. The Fano lineshape, ubiquitous across the branches of physics, appears in systems in which a discrete mode is coupled to a continuum

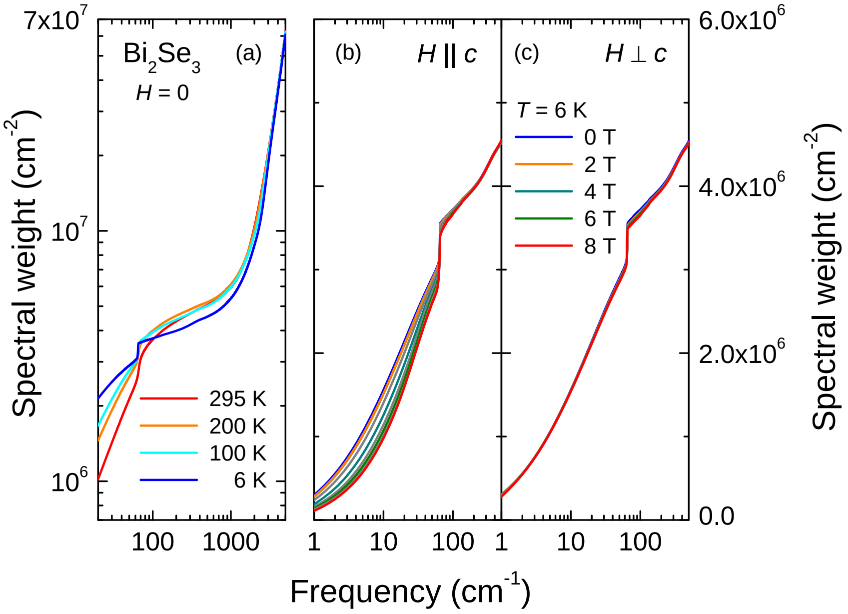

Figure 6.7: Integrated spectral weight $\int_0^\omega d\nu\ \sigma_1(\nu)$.

of excitations (176). Quantum interference between the wave functions for two transition pathways between the ground state and an excited state (one directly to a discrete excited state; the other to the continuum, and then to the discrete state) results in an asymmetric scattering cross section. This phenomenon is a common indicator of hybridization between phonons and conduction electrons in materials with high polarizability.

To better understand this behavior, we have applied to the data a fitting analysis which models the α phonon as a Fano resonance of the form

$$\hat{\sigma}(\omega) = A * \left(\frac{\mid q + \epsilon \mid^2}{1 + \epsilon^2} - 1 \right), \tag{6.1}$$

as a function of the reduced energy $\epsilon = (\omega - \omega_0)/(\Gamma/2)$. This lineshape is characterized by the center frequency ω_0, linewidth Γ, and amplitude A, similar to a Lorentz oscillator. The Fano parameter q determines the asymmetry of the resonance, and is a useful measure of the degree of coupling between the discrete and continuum modes (177). The Lorentz lineshape is recovered for $|q| \to \infty$ and the sign of q sets the direction of asymmetry. q is in general a complex parameter, but can be equivalently accounted for with an additional constant A, as shown above. All other spectral features, including free-carrier and interband absorptions, were modeled with classical Lorentz oscillators. A representative fit for $H = 4$ T is compared to the far-IR experimental reflectance data in Figs. 8(a). The measured lineshape is clearly reproduced by the Fano functional form. Fitting parameters for the α phonon and Drude peak are displayed in Table 1.

The evolution of the fit parameters for the α and Drude modes with magnetic field yields insight into the nature of free electron-lattice coupling in Bi_2Se_3. Since changes to the α mode are minimal for $H \perp c$, we will focus on data for $H \parallel c$. The most prominent overall effect of magnetic field upon the conductivity spectra in Fig. 6.5(b) is the increase of the linewidth $1/\tau^{Drude}$ of the Drude peak. This parameter has been extracted from the oscillator fit and is plotted with triangles in Fig. 6.8(b). We see that $1/\tau^{Drude}$ is constant at low fields, increases sharply for intermediate fields, and saturates at 30 cm^{-1} at $H = 7$ T. The width of the modified phonon (not shown) increases linearly with field over entire range. The asymmetry parameter q, indicated by squares in Fig. 6.8(b), scales with $1/\tau^{Drude}$, including the same plateau features for $H < 3$ T and $H < 7$ T. This correlation suggests that the strength of coupling between the two modes may increase as the free-carrier scattering frequency approaches that of the lattice vibration. The negative value of q indicates that the phonon is primarily interacting with states at higher energy (178); this is consistent with the idea of the α mode interacting more strongly with the plasmon when the Drude peak is broader, having more states pushed above the phonon frequency. Interactions between the α mode and γ mode may exist as well, since the latter is strongly field-dependent as well.

Magnetic field-induced modification of the Fano effect has been observed in several areas of condensed matter physics; the role of the field in modifying the response is unique to each system. In experiments involving mesoscopic coupled-quantum-dot interferometers (179) and coupled carbon nanotubes (180), the magnetic field modifies the Fano interaction via the Aharonov-Bohm effect, adding an arbitrary phase to one of the transition pathways. In ultrathin epitaxial semiconductors, application of magnetic field tends to symmeterize Fano resonance

Table 6.1: Parameters used for low-frequency oscillators in Fano/Lorentz fit to infrared spectra, as shown in Fig. 6.8.

H (T)	$\omega^2_{p,Drude}$ (10^6 cm^{-2})	$1/\tau_{Drude}$ (cm^{-1})	A	ω_0 (cm^{-1})	Γ (cm^{-1})	q
0	2.52	22	64.76	34	0.41	-17
1	2.52	22	64.79	34	0.42	-17
2	2.52	22	64.78	30.2	0.46	-17
3	2.63	24	64.79	33.4	0.48	-16
4	2.89	25	64.80	36.8	0.50	-15
5	3.28	26	64.80	52	0.54	-12
6	3.43	28	64.80	146	0.58	-7.0
7	3.43	30	64.75	260	0.66	-5.0
8	3.33	30	64.57	310	0.69	-4.8

features due to Landau level confinement (181). This is in contrast to the situation in bulk intrinsic semiconductors, where Fano resonances are created when magnetoexcitons overlap in energy with continuum band states (182).

An intriguing connection to the proposed topological insulator behavior in Bi_2Se_3 is the fact that modes defined by the coupling of a plasmon and a longitudinal optical phonon are sensitive to surface space-charge layers (177). While the bulk carriers certainly dominate the response in the present sample, it would be informative to monitor this effect in low-carrier density crystals in which the surface states are responsible for a significant portion of the metallicity.

6.3.3 Assessing relevant magnetic field scales via comparsion to elemental bismuth

Changes of the optical spectra of Bi_2Se_3 with magnetic field, while informative, are fairly mild. This is due to the small magnitude of the experimental magnetic field relative to the field scales of the electronic system. According to magneto-transport measurements at low temperatures, magnetic fields on the or-

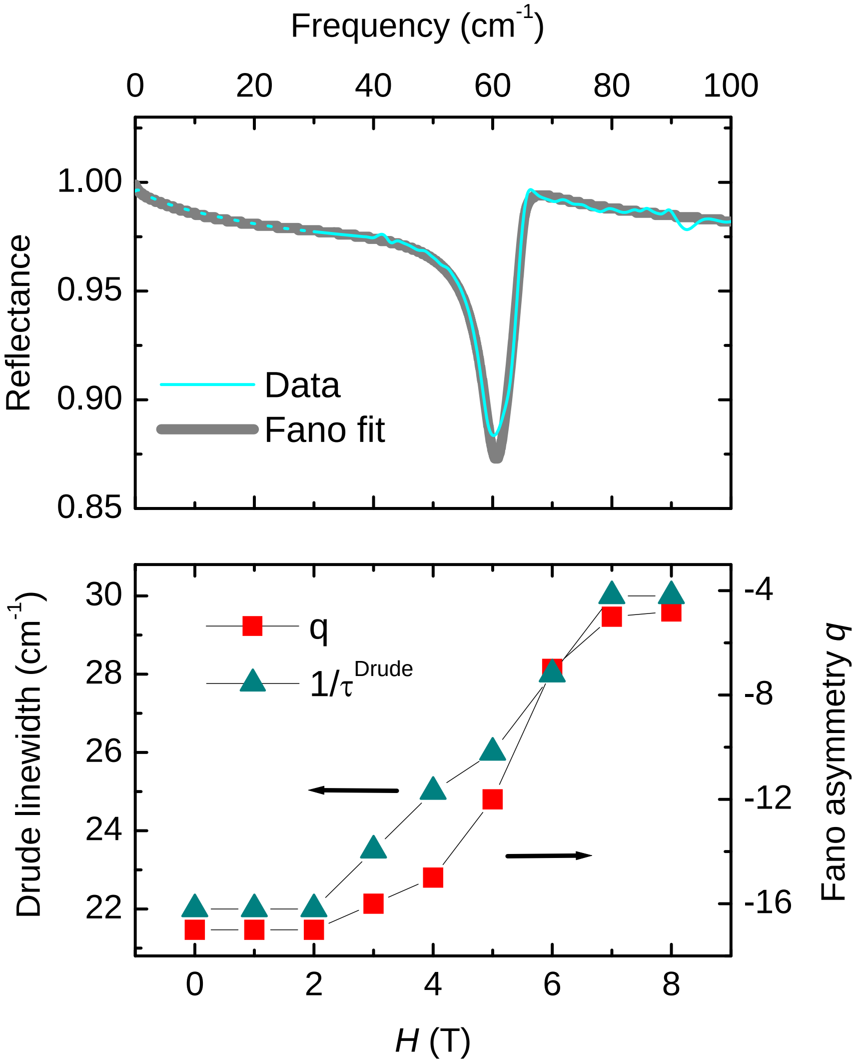

Figure 6.8: (a) Representative fit (thick line) of Fano lineshape to far-IR reflectance data (thin line). Here, $T = 6$ K and $H = 4$ T. (b) Fit parameters q (square symbols) and $1/\tau^{Drude}$ (triangle symbols) as a function of magnetic field. The Fano asymmetry scales with the linewidth of the Drude conductivity.

der of 16 T, twice those accesible in the present study, are needed to resolve Shubinikov-de Haas oscillations of the Hall coefficient (172). Cyclotron absorption should conceivably be observed at lower fields than this, however. Given the effective mass of 0.105 m_e determined for $H \parallel c$ from magnetoabsorption measurements (172), the cyclotron frequency should be $\omega_c = eH/2\pi cm = 71$ cm^{-1} at 8 T. Since the free-carrier scattering rate is approximately $1/\tau^{Drude} = 30$ T, the cyclotron mode should be within the experimental window, yet we do not observe it in our experiment.

This behavior can be contrasted with that of elemental bismuth, which has much lighter charge carriers ($m^* = 0.004$) and lower carrier density, rendering it more susceptible to the magnetic field (183). Indeed, in Bi quantum oscillations have been observed at fields less than 1 T, and the quantum limit, the magnetic field at which all carriers reside in the lowest Landau levels, is only 9 T. Figure 9 displays reflectance data for Bi at $T = 6$ K in magnetic fields up to 8 T, just below the quantum limit. Here we see a dramatic reconstruction of the electromagnetic response by magnetic field: the sharp plasma edge at 160 cm^{-1} in zero field has become nearly unrecognizable, and the low-frequency reflectance is strongly suppressed. Analysis and comparison of the optical conductivity is more complicated because the small effective mass precludes the use of the KK transformation.

6.4 Conclusion

We have determined the optical conductivity $\hat{\sigma}(\omega)$ in magnetic field for the narrow-gap semiconductor Bi$_2$Se$_3$ through a combination of infrared reflectance and UV-visible ellipsometry. A gap in the conductivity induces an extensive redistribution of spectral weight over the mid-IR frequency region. Magnetic fields $H \perp c$ introduce a new absorption in the far-IR, as well as slightly shift the metallic plasma edge minimum. For $H \parallel c$, a strong low-frequency phonon is significantly modified, and a Fano lineshape analysis reveals an interesting scaling between the phonon asymmetry and the broadening width of the Drude peak. This observation sheds more light on the nature of electron-phonon coupling in this system. Future

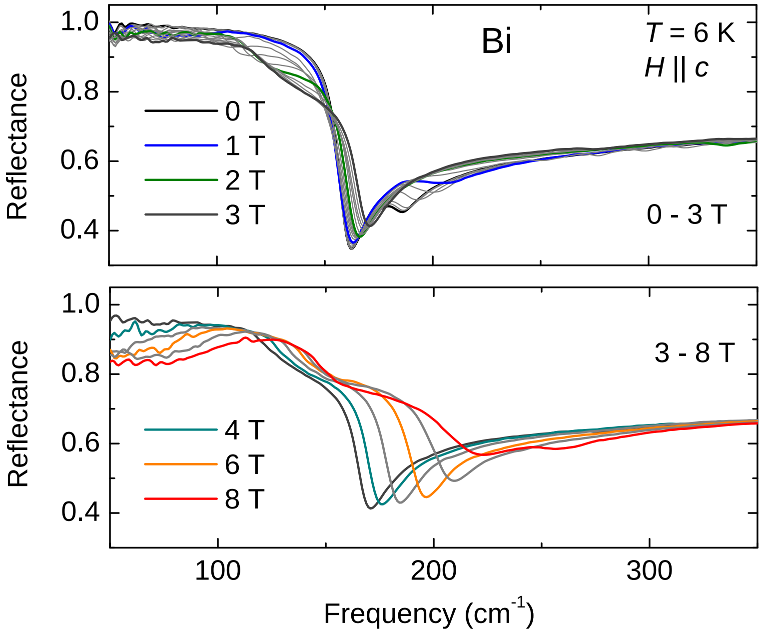

Figure 6.9: Infrared reflectance of elemental bismuth in magnetic fields oriented parallel to the trigonal c axis. Maximum measured field is just below the quantum limit of 9 T.

studies will investigate crystals which are closer to the stoichiometric levels in an attempt to optically characterize the expected topological insulator behavior.

Acknowledgments

This research was supported by NSF DMR 0705171.

Bibliography

[1] S. L. Cooper and K. E. Gray, in Physical Properties of High Temperature Superconductors IV, edited by D. M. Ginsberg (World Scientific, Singapore, 1994) pp. 63–188.

[2] D. N. Basov and T. Timusk, Rev. Mod. Phys. **77**, 721-779 (2005).

[3] D. N. Basov, T. Timusk, B. Dabrowski, and J. D. Jorgensen, Phys. Rev. B **50**, 3511 (1994).

[4] T. Shibauchi, H. Kitano, K. Uchinokura, A. Maeda, T. Kimura, and K. Kishio, Phys. Rev. Lett. **72**, 2263 (1994).

[5] S. V. Dordevic, E. J. Singley, D. N. Basov, Seiki Komiya, Yoichi Ando, E. Bucher, C. C. Homes, and M. Strongin, Phys. Rev. B **65**, 134511 (2002).

[6] M. Reedyk, T. Timusk, J. S. Xue, and J. E. Greedan, Phys. Rev. B **49**, 15984 (1994).

[7] J. Schützmann, S. Tajima, S. Miyamoto, Y. Sato, and R. Hauff, Phys. Rev. B **52**, 13665 (1995).

[8] C. Bernhard, D. Munzar, A. Golnik, C.T. Lin, A. Wittlin, J. Humlicek, and M. Cardona, Phys. Rev. B **61**, 618 (2000).

[9] C. C. Homes, T. Timusk, R. Liang, D. A. Bonn, and W. N. Hardy, Phys. Rev. Lett. **71**, 1645–1648 (1993).

[10] C. C. Homes, T. Timusk, D. A. Bonn, R. Liang, W. N. Hardy, Physica C **254**, 265 (1995).

[11] D. N. Basov, H. A. Mook, B. Dabrowski, and T. Timusk, Phys. Rev. B **52**, R13141 (1995).

[12] S. Tajima, J. Schutzmann, S. Miyamoto, I. Terasaki, Y. Sato, and R. Hauff, Phys. Rev. B **55**, 6051 (1997).

[13] C. Bernhard, D. Munzar, A. Wittlin, W. Konig, A. Golnik, C. T. Lin, M. Kläser, Th. Wolf, G. Müller-Vogt, and M. Cardona, Phys. Rev. B **59**, R6631 (1999).

[14] D. Munzar, C. Bernhard, A. Golnik, J. Humlĭček, M. Cardona, Solid State Commun. **112**, 365 (1999).

[15] D. N. Basov, S. I. Woods, A. S. Katz, E. J. Singley, R. C. Dynes, M. Xu, D. G. Hinks, C. C. Homes, and M. Strongin, Science **283**, 49 (1999).

[16] D. N. Basov, C. C. Homes, E. J. Singley, M. Strongin, T. Timusk, G. Blumberg, and D. van der Marel, Phys. Rev. B **63**, 134514 (2001).

[17] A. S. Katz, S. I. Woods, E. J. Singley, T. W. Li, M. Xu, D. G. Hinks, R. C. Dynes and D. N. Basov, Phys. Rev. B **61**, 5930 (1999).

[18] A. B. Kuzmenko, N. Tombros, H. J. A. Molegraaf, M. Gruninger, D. van der Marel, and S. Uchida, Phys. Rev. Lett. **91**, 37004 (2003).

[19] A. V. Boris, D. Munzar, N. N. Kovaleva, B. Liang, C. T. Lin, A. Dubroka, A. V. Pimenov, T. Holden, B. Keimer, Y. -L. Mathis, C. Bernhard, Phys. Rev. Lett. **89**, 277001 (2002).

[20] Dominik Munzar, Todd Holden, Christian Bernhard, Phys. Rev. B **67**, 020501(R) (2003).

[21] K. Tamasaku, Y. Nakamura, and S. Uchida, Phys. Rev. Lett. **69**, 1455 (1992).

[22] T. Timusk and C. C. Homes, Solid State Commun. **126**, 63 (2003).

[23] S. V. Dordevic, E. J. Singley, J. H. Kim, M. B. Maple, Seiki Komiya, S. Ono,Yoichi Ando, T. Rõõm, Ruxing Liang, D. A. Bonn, W. N. Hardy, J. P.

Carbotte, C. C. Homes, M. Strongin, and D. N. Basov, Phys. Rev. B **69**, 094511 (2004).

[24] A. M. Gerrits, M. E. J. Boonman, A. Wittlin, P. J. M. van Bentum, V. H. M. Duijn, and A. A. Menovsky, Phys. Rev. B **51**, 12049 (1995).

[25] S. V. Dordevic, S. Komiya, Y. Ando, Y. J. Wang, and D. N. Basov, Phys. Rev. B **71**, 054503 (2005).

[26] S. V. Dordevic, S. Komiya, Y. Ando, Y. J. Wang, and D. N. Basov, Europhys. Lett. **61**, 122 (2003).

[27] K. M. Kojima, S. Uchida, Y. Fudamoto and S. Tajima, Phys. Rev. Lett. **89**, 247001 (2002).

[28] Diana Dulic, S. J. Hak, D. van der Marel, W. N. Hardy, A. E. Koshelev, Ruixing Liang, D. A. Bonn, and B. A. Willemsen, Phys. Rev. Lett. **86**, 4660 (2001)..

[29] G. Blatter, M. V. Feigel'man, V. B. Geshkenbein, A. I. Larkin, and V. M. Vinokur, Rev. Mod. Phys. 66, 1125 (1994).

[30] M. Golosovsky, M. Tsindlekht, and D. Davidov, Supercond. Sci. Techno. **9**, 1 (1996).

[31] S. N. Artemenko, I. G. Gorlova, and Yu I. Latyshev, Phys. Lett. A **138**, 428 (1989).

[32] W. K. Kwok, J. Fendrich, U. Welp, S. Fleshler, J. Downey, and G. W. Crabtree, Phys. Rev. Lett. **72**, 1088 (1994).

[33] E. Zeldov, D. Majer, M. Konczykowski, V. B. Geshkenbein, M. M. Vinokur, and H. Shtrikman, Nature **375**, 373 (1995).

[34] Y. Matsuda, M. B. Gaifullin, K. Kumagai, K. Kadowaki, and T. Mochiku, Phys. Rev. Lett. **75**, 4512 (1995).

[35] D. van der Marel and A. Tsvetkov, Czech. J. Phys. **46**, 3165 (1996).

[36] M. Tachiki, T. Koyama, and S. Takahashi, Phys. Rev. B **50**, 7065 (1994).

[37] L. Bulaevskii and John R. Clem, Phys. Rev. B **44**, 10234 (1991).

[38] L. N. Bulaevskii, V. L. Pokrovsky, and M.P. Maley, Phys. Rev. Lett. **76**, 1719 (1996).

[39] M. Ichioka, Phys. Rev. B **51**, 9423 (1995).

[40] A. E. Koshelev, L. I. Glazman, and A. I. Larkin, Phys. Rev. B **53**, 2786 (1996).

[41] Kouji Segawa and Yoichi Ando, Phys. Rev. B **69**, 104521 (2004).

[42] C. C. Homes, M. Reedyk, D. A. Cradles, and T. Timusk, Appl. Opt. **32**, 2976 (1993).

[43] W. J. Padilla, Z. Q. Li, K. S. Burch, Y. S. Lee, K. J. Mikolaitis, and D. N. Basov, Rev. Sci. Instrum. **75**, 4710 (2004).

[44] D. Y. Smith, Phys. Rev. B **13**, 5303 (1976).

[45] W. J. Padilla, Y. S. Lee, M. Dumm, G. Blumberg, S. Ono, Kouji Segawa, Seiki Komiya, Yoichi Ando, and D. N. Basov, Phys. Rev. B **72**, 060511(R) (2005).

[46] Yu. Eltsev and O. Rapp, Phys. Rev. B **57**, R3237-R3240 (1998).

[47] A. E. Koshelev, Phys. Rev. B **76**, 054525 (2007).

[48] Yoshihiko Nonomura and Xiao Hu, Phys. Rev. B **74** 024504 (2006).

[49] A. E. Koshelev, arXiv:cond-mat/0602341 v1 (2006).

[50] S. N. Artemenko and S. V. Remizov, JETP Lett. **66**, 853 (1997).

[51] A. E. Koshelev and I. Aranson, Phys. Rev. B **64**, 174508 (2001).

[52] H. Shibata and T. Yamada, Phys. Rev. Lett. **81**, 3519 (1998).

[53] Diana Dulic, A. Pimenov, D. van der Marel, D. M. Broun, Saeid Kamal, W. N. Hardy, A. A. Tsvetkov, I. M. Sutjaha, Ruixing Liang, A. A. Menovsky, A. Loidl, and S. S. Saxena, Phys. Rev. Lett. **86**, 4144 (2001).

[54] A. Pimenov, A. Loidl, D. Dulic, D. van der Marel, I. M. Sutjahja, and A. A. Menovsky, Phys. Rev. Lett. **87**, 177003 (2001).

[55] D. van der Marel and A. A. Tsvetkov, Phys. Rev. B **64**, 024530 (2001).

[56] Ch. Helm, L. N. Bulaevskii, E. M. Chudnovsky, and M. P. Maley, Phys. Rev. Lett. **89**, 057003 (2002).

[57] S. V. Dordevic, Seiki Komiya, Yoichi Ando, and D. N. Basov, Phys. Rev. Lett. **91**, 167401 (2003).

[58] A. E. Koshelev, L. N. Bulaevskii, and M. P. Maley, Phys. Rev. B **62**, 14403 (2000).

[59] Yoichi Ando and Kouji Segawa, Phys. Rev. Lett. **88**, 167005 (2002).

[60] J. R. Clem and M. W. Coffey, Phys. Rev. B **42**, 6209-6216 (1990).

[61] Mark W. Coffey and John R. Clem, Phys. Rev. B **44**, 6903 (1991).

[62] D. M. Gaitonde and T. V. Ramakrishnan, Phys. Rev. B **56**, 11951 (1997).

[63] Lorenz Bartosch, Leon Balents, and Subir Sachdev, arXiv:cond-mat/0502002 v3 (2006).

[64] Kathryn A. Moler, Alexander L. Fetter, and Aharon Kapitulnik, J.Low. Temp. Phys. **100**, 185 (1995).

[65] I. Kakeya, T. Wada, R. Nakamura, and K. Kadowaki, Phys. Rev. B **72**, 014540 (2005).

[66] A. L. Fetter and M. J. Stephen, Phys. Rev. **168**, 475 (1968).

[67] T. Koyama, Phys. Rev. B **68**, 224505 (2003).

[68] A. E. Koshelev and I. Aranson, Phys. Rev. B **64**, 174508 (2001).

[69] L. N. Bulaevskii, D. Domínguez, M. P. Maley, and A. R. Bishop, Phys. Rev. B **55**, 8482 (1997).

[70] Y.-S. Lee, Kouji Segawa, Yoichi Ando, and D. N. Basov, Phys. Rev. B **70**, 014518 (2004).

[71] P. J. Thomas, J. C. Fenton, G. Yang, and C. E. Gough, arXiv:cond-mat/0001365 v1 (2000).

[72] M. Dumm, D.N. Basov, Seiki Komiya, Yasushi Abe, and Yoichi Ando, Phys. Rev. Lett. **88**, 147003 (2002).

[73] J. Hwang, J. Yang, T. Timusk, S. G. Sharapov, J. P. Carbotte, D. A. Bonn, Ruixing Liang, and W. N. Hardy, Phys. Rev. B **73**, 014508 (2006).

[74] A. Hosseini, R. Harris, S. Kamal, P. Dosanjh, J. Preston, R. Liang, W. N. Hardy, and D. A. Bonn, Phys. Rev. B **60**, 1349 (1999).

[75] Y. S. Lee, Z. Q. Li, W. J. Padilla, S. V. Dordevic, C. C. Homes, Kouji Segawa, Yoichi Ando, and D. N. Basov, Phys. Rev. B **72,** 172511 (2005).

[76] E. M. Gyorgy, R. B. van Dover, L. F. Schneemeyer, A. E. White, H. M. O'Bryan, R. J. Felder, J. V. Waszczak, W. W. Rhodes, and F. Hellman, Appl. Phys. Lett. **65**, 2465 (1990).

[77] J. A. Herbsommer, G. Nieva, and J. Luzuriaga, Phys. Rev. B **62**, 3534 (2000).

[78] P. J. Turner, R. Harris, Saeid Kamal, M. E. Hayden, D. M. Broun, D. C. Morgan, A. Hosseini, P. Dosanjh, G. K. Mullins, J. S. Preston, Ruixing Liang, D. A. Bonn, and W. N. Hardy, Phys. Rev. Lett. **90**, 237005 (2003).

[79] For a theoretical prospective see, for example, A. J. Leggett, Nat. Phys. **2**, 134 (2006).

[80] H. J. A. Molegraaf, C. Presura, D. van der Marel, P. H. Kes, and M. Li, Science **295**, 2239 (2002).

[81] A. B. Kuzmenko, N. Tombros, H. J. A. Molegraaf, M. Gruninger, D. van der Marel, and S. Uchida, Phys. Rev. Lett. **91**, 037004 (2003).

[82] C. C. Homes, S. V. Dordevic, D. A. Bonn, R. Liang, and W. N. Hardy, Phys. Rev. B **69**, 024514 (2004).

[83] A. F. Santander-Syro, R. P. S. M. Lobo, N. Bontemps, W. Lopera, D. Girata, Z. Konstantinovic, Z. Z. Li, and H. Raffy, Phys. Rev. B **70**, 134504 (2004).

[84] A. V. Boris, N. N. Kovaleva, O. V. Dolgov, T. Holden, C. T. Lin, B. Keimer, C. Bernhard, Science **304**, 708 (2004).

[85] M. R. Norman, M. Randeria, B. Janko, and J. C. Campuzano, Phys. Rev. B **61**, 14742 (2000).

[86] J. E. Hirsch, Physica C **199**, 305 (1992).

[87] S. Chakravarty, Hae-Young Kee, and E. Abrahams, Phys. Rev. Lett. **82**, 2366 (1999).

[88] P. F. Maldague, Phys. Rev. B **16**, 2437 (1977).

[89] D. Baeriswyl, C. Gros, and T. M. Rice, Phys. Rev. B **35**, 8391 (1987).

[90] R. A. Ferrell and R. E. Glover, III, Phys. Rev. **109**, 1398 (1958).

[91] Complications of the sum rule analysis due to frequency cutoffs have been shown to be irrelevant in the superconducting state, and do not affect the magneto optics analysis. See F. Marsiglio, Phys. Rev. B **73**, 064507 (2006) and F. Marsiglio, E. van Heumen, and A. B. Kuzmenko, Phys. Rev. B **77**, 144510 (2008).

[92] X. F. Sun, Kouji Segawa, and Yoichi Ando, Phys. Rev. Lett. **93**, 107001 (2004).

[93] A. D. LaForge, W. J. Padilla, K. S. Burch, Z. Q. Li, S. V. Dordevic, Kouji Segawa, Yoichi Ando, and D. N. Basov, Phys. Rev. B **76**, 054524 (2007).

[94] Li Yu, D. Munzar, A. V. Boris, P. Yordanov, J. Chaloupka, Th. Wolf, C. T. Lin, B. Keimer, and C. Bernard, Phys. Rev. Lett. **100**, 177004 (2008).

[95] M. Gruninger, D. van der Marel, A. A. Tsvetkov, and A. Erb, Phys. Rev. Lett. **84**, 1575 (2000).

[96] J. Schutzmann, S. Tajima, S. Miyamoto, Y. Sato, and R. Hauff, Phys. Rev. B **52**, 13665 (1995).

[97] C. Bernhard, D. Munzar, A. Golnik, C. T. Lin, A. Wittlin, J. Humlicek, and M. Cardona, Phys. Rev. B **61**, 618 (2000).

[98] Y. Ando and K. Segawa, Phys. Rev. Lett. **88**, 167005 (2002).

[99] Y. S. Lee, Kouji Segawa, Z. Q. Li, W. J. Padilla, M. Dumm, S. V. Dordevic, C. C. Homes, Yoichi Ando, and D. N. Basov, Phys. Rev. B **72**, 054529 (2005).

[100] J. E. Sonier, J. H. Brewer, R. F. Kiefl, D. A. Bonn, J. Chakhalian, S. R. Dunsiger, W. N. Hardy, R. Liang, W. A. MacFarlane, R. I. Miller, D. R. Noakes, T. M. Riseman, and C. E. Stronach, Phys. Rev. B **61**, R890 (2000).

[101] A. E. Koshelev, L. I. Glazman, and A. I. Larkin, Phys. Rev. B **53**, 2786 (1996).

[102] L. N. Bulaevskii, A. E. Koshelev, V. M. Vinokur, and M. P. Maley, Phys. Rev. B **61**, R3819 (2000).

[103] L. B. Ioffe and A. J. Millis, Science **285**, 1241 (1999).

[104] N. Shah and A. J. Millis, Phys. Rev. B **65**, 024506 (2001).

[105] J. Orenstein, J. Corson, S. Oh, and J. N. Eckstein, Annalen der Physik **15**, 596-605 (2006).

[106] Y. Wang, L. Li, and N. P. Ong, Phys. Rev. B **73**, 024510 (2006).

[107] R. Kubo, J. Phys. Soc. Japan 12, 570 (1957).

[108] A. S. Katz, S. I. Woods, E. J. Singley, T. W. Li, M. Xu, D. G. Hinks, R. C. Dynes, and D. N. Basov, Phys. Rev. B **61**, 5930 (2000).

[109] Li Yu, D. Munzar, A. V. Boris, P. Yordanov, J. Chaloupka, Th. Wolf, C. T. Lin, B. Keimer, and C. Bernhard, Phys. Rev. Lett. **100**, 177004 (2008).

[110] A. D. LaForge, W. J. Padilla, K. S. Burch, Z. Q. Li, A. A. Schafgans, Kouji Segawa, Yoichi Ando, and D. N. Basov, Phys. Rev. Lett. **101**, 097008 (2008).

[111] D. N. Basov, T. Timusk, B. Dabrowski, and J. D. Jorgensen, Phys. Rev. B **50**, 3511 (1994).

[112] V. J. Emery and S. A. Kivelson, Nature **374**, 434 (1995).

[113] J. Corson, R. Mallozzi, J. Orenstein, J. N. Eckstein and I. Bozovic, Nature **398**, 221 (1999).

[114] H. Ding, T. Yokoya, J. C. Campuzano, T. Takahashi, M. Randeria, M. R. Norman, T. Mochiku, K. Kadowaki, and J. Giapintzakis, Nature **382**, 51 (1996).

[115] A.G. Loeser, Z.-X. Shen, D.S. Dessau, D.S. Marshall, C.H. Park, P. Fournier, and A. Kapitulnik, Science **273**, 325 (1996).

[116] S. Chakravarty, A. Sudbo, P.W. Andersen, and S. Strong, Science **261**, 337 (1993).

[117] T. Shibauchi, L. Krusin-Elbaum, M. Hasegawa, Y. Kasahara, R. Okazaki, and Y. Matsuda, Proc. Nat. Acad. Sci. USA **105** 7120 (2008).

[118] A. A. Schafgans, A. D. LaForge, S. V. Dordevic, M. M. Qazilbash, Seiki Komiya, Yoichi Ando, and D. N. Basov, unpublished.

[119] M. R. Norman, H. Ding, M. Randeria, J. C. Campuzano, T. Yokoya, T. Takeuchi, T. Takahashi, T. Mochiku, K. Kadowaki, P. Guptasarma, and D. G. Hinks, Nature (London) **392**, 157 (1998).

[120] T. Yoshida, X. J. Zhou, T. Sasagawa, W. L. Yang, P. V. Bogdanov, A. Lanzara, Z. Hussain, T. Mizokawa, A. Fujimori, H. Eisaki, Z.-X. Shen, T. Kakeshita, and S. Uchida, Phys. Rev. Lett. **91**, 027001 (2003).

[121] There have been several recent reports of evidence for hole pockets. See J. Chang, Y. Sassa, S. Guerrero, M. Mansson, M. Shi, S. Pailhes, A. Bendounana, R. Mottl, T. Claesson, O. Tjernberg, L. Patthey, M. Ido, M. Oda, N. Momono, C. Mudry, and J. Mesot, New J. Phys. **10**, 103016 (2008); and Jainqiao Meng, Guodong Liu, Wentao Zhang, Lin Zhao, Haiyun Liu, Daixiang Mu, Shanyu Liu, Xiaoli Dong, Wei Lu, Guiling Wang, Yong Zhou, Yong Zhu, Xiaoyang Wang, Zuyan Xu, Chuangtian Chen, and X. J. Zhou, arXiv:0906.2682. The distinction is not crucial here, as the question is whether electron pockets can play a dominant role.

[122] Y. S. Lee, Kouji Segawa, Z. Q. Li, W. J. Padilla, M. Dumm, S. V. Dordevic, C. C. Homes, Yoichi Ando, and D. N. Basov, Phys. Rev. B **72**, 054529 (2005).

[123] N. Doiron-Leyraud, C. Proust, D. LeBoeuf, J. Levallois, J.-B. Bonnemaison, R. Liang, D. A. Bonn, W. N. Hardy, and L. Taillefer, Nature **447**, 565 (2007).

[124] D. LeBoeuf, N. Doiron-Leyraud, J. Levallois, R. Daou, J.-B. Bonnemaison, N. E. Hussey, L. Balicas, B. J. Ramshaw, R. Liang, D. A. Bonn, W. N. Hardy, S. Adachi, C. Proust, and L. Taillefer, Nature **450**, 533 (2007).

[125] C. Jaudet, D. Vignolles, A. Audouard, J. Levallois, D. LeBoeuf, N. Doiron-Leyraud, B. Vignolle, M. Nardone, A. Zitouni, R. Liang, D. A. Bonn, W. N. Hardy, L. Taillefer, and C. Proust, Phys. Rev. Lett. **100**, 187005 (2008).

[126] S. E. Sebastian, N. Harrison, E. Palm, T. P. Murphy, C. H. Mielke, R. Liang, D. A. Bonn, W. N. Hardy, and G. G. Lonzarich, Nature **454**, 200 (2008).

[127] Olivier Cyr-Choinire, R. Daou, Francis Lalibert, David LeBoeuf, Nicolas Doiron-Leyraud, J. Chang, J.-Q. Yan, J.-G. Cheng, J.-S. Zhou, J. B. Goodenough, S. Pyon, T. Takayama, H. Takagi,4, Y. Tanaka and Louis Taillefer, Nature **458**, 743 (2009).

[128] T. Helm, M. V. Kartsovnik, M. Bartkowiak, N. Bittner, M. Lambacher, A. Erb, J. Wosnitza, and R. Gross, Cond-mat arXiv:0906.1431v2.

[129] A. J. Millis and M. R. Norman, Phys. Rev. B **76**, 220503R (2007).

[130] N. Harrison, Phys. Rev. Lett. **102**, 206405 (2009).

[131] Sudip Chakravarty and Hae-Young Kee, Proceedings of the National Academy of Sciences**105**, 8835 (2008).

[132] J. M. Tranquada, D. N. Basov, A. D. LaForge, A. A. Schafgans, arXiv:0905.2208.

[133] R. -H. He, K. Tanaka, S. -K. Mo, T. Sasagawa, M. Fujita, T. Adachi, N. Manella, K. Yamada, Y. Koike, Z. Hussain, and Z. -X. Shen, Nat. Phys. **5**, 119 (2009).

[134] T. Valla, A. V. Federov, J. Lee, J. C. Davis, and G. D. Gu, Science **314**, 1914 (2006).

[135] L. B. Ioffe and A. J. Millis, Science **245**, 1241 (1999); *ibid.*, Phys. Rev. B **61**, 9077 (2000).

[136] D. van der Marel Phys. Rev. B **60**, R765 (1999).

[137] A. D. LaForge, W. J. Padilla, K. S. Burch, Z. Q. Li, A. A. Schafgans, Kouji Segawa, Yoichi Ando, and D. N. Basov, Phys. Rev. B. **79**, 104516 (2009).

[138] A. A. Schafgans, A. D. LaForge, S. V. Dordevic, M. M. Qazilbash, Seiki Komiya, Yoichi Ando, and D. N. Basov, unpublished (2009).

[139] J. Chang, R. Daou, Cyril Proust, David LeBoeuf, Nicolas Doiron-Leyraud, Francis Laliberte, B. Pingault, B. J. Ramshaw, Ruixing Liang, D. A. Bonn, W. N. Hardy, H. Takagi, A. Antunes, I. Sheikin, K. Behnia, Louis Taillefer, arXiv:0907.5039.

[140] D. N. Basov, H. A. Mook, B. Dabrowski, and T. Timusk, Phys. Rev. B **52**, 13159

[141] A. V. Puchkov, D. N. Basov, and T. Timusk, J. Phys. Cond. Mat. **8**, 10049 (1996).

[142] Tsuyoshi Kawakami, Takasada Shibauchi, Yuhki Terao, Minoru Suzuki, and Lia Krusin-Elbaum, Phys. Rev. Lett. **95** 017001 (2005).

[143] T. Shibauchi, L. Krusin-Elbaum, Ming Li, M. P. Maley, and P. H. Kes, Phys. Rev. Lett. **86**, 5763 (2001).

[144] V. M. Krasnov, A. E. Kovalev, A. Yurgens, and D. Winkler, Phys. Rev. Lett. **86**, 2657 (2001).

[145] E. Berg, E. Fradkin, E.-A. Kim, S. A. Kivelson, V. Oganesyan, J. M. Tranquada, and S. C. Zhang, Phys. Rev. Lett. **99**, 127003 (2007); E. Berg, E. Fradkin, and S.A. Kivelson, Cond-mat arXiv:0810.1564.

[146] In the limit of $1/\tau >> \Omega_{LF}$ the broadened coherent response would be indistinguishable from a constant offset.

[147] For a large range of underdoped cuprate superconductors, the value of the superfluid density is significantly larger than the spectral weight which is donated from low frequencies during the superconducting transition. This anomaly can be interpreting as a lowering of electronic kinetic energy in the superconducting state. For more details, see Refs. (110) and (137) and references therein.

[148] S. Tajima, T. Noda, H. Eisaki and S. Uchida, Phys. Rev. Lett. **86**, 500 (2001).

[149] C. C. Homes, private communication.

[150] Q. Li, M. Hücker, G. D. Gu, A. M. Tsvelik, and J. M. Tranquada, Phys. Rev. Lett. **99**, 067001 (2007).

[151] B. Lake, H. M. Ronnow, N. B. Christensen, G. Aeppli, K. Lefmann, D. F. McMorrow, P. Vorderwisch, P. Smeibidl, N. Mangkorntong, T. Sasagawa, M. Nohara, H. Takagi, and T. E. Mason, Nature **415**, 299 (2002).

[152] D. Haug, V. Hinkov, A. Suchaneck, D. S. Insov, N. B. Christensen, Ch. Niedermayer, P. Bourges, Y. Sidis, J. T. Park, A. Ivanov, C. T. Lin, J. Mesot, B. Keimer, arXiv:0902.3335v1 (2009).

[153] N. E. Hussey, A. P. Mackenzie, J. R. Cooper, Y. Maeno, S. Nishizaki, and T. Fujita, Phys. Rev. B **57**, 5505 (1998).

[154] M. G. Hildebrand, M. Reedyk, T. Katsufuji, and Y. Tokura, Phys. Rev. Lett. **87**, 227002 (2001).

[155] E. M. Black, L. Conwell, L. Seigle, and C. W. Spencer, J. Phys. Chem. Sol. **2**, 240 (1957).

[156] F.J. DiSalvo, Science **285**, 703 (1999).

[157] Haijun Zhang, Chao-Xing Liu, Xiao-Liang Qi, Xi Dai, Zhong Fang and Shou-Cheng Zhang, Nat. Phys. **5**, 438 (2009).

[158] D. Hsieh, D. Qian, L.Wray, Y. Xia, Y. S. Hor, R. J. Cava, and M. Z. Hasan, Nature **452**, 970 (2008).

[159] L. Fu, C. L. Kane, Phys. Rev. Lett. **100**, 096407 (2008).

[160] K.J. Plucinski, W. Gruhn, I.V. Kityk, W. Imiolek, H. Kaddouri, S. Benet, Optics Comm. **204**, 355361 (2002),

[161] Xiao-Liang Qi, Taylor L. Hughes, and Shou-Cheng Zhang, Phys. Rev. B **78**, 195424 (2008).

[162] A.P. Schnyder *et al.*, Phys. Rev. B **78**, 195125 (2008).

[163] S.Y. Zhou, G.-H. Gweon, J. Graf, A.V. Fedorov, C.D. Spataru, R.D. Diehl, Y. Kopelevich, D.-H. Lee, Steven G. Louie, and A. Lanzara, Nat. Phys. **2**, 595.

[164] Y. Xia, L. Wray, D. Qian, D. Hsieh, A. Pal, H. Lin, A., Bansil, D. Grauer, Y. S. Hor, R. J. Cava, and M. Z. Hasan, arXiv:0812.2078v1.

[165] Guohong Li and Eva Y. Andrei, Nat. Phys. **3**, 693 (2007).

[166] H. Kohler and H. Fischer, Phys. Stat. Sol. (b) **69**, 349 (1975)

[167] J. Navrtil, J. Hork, T. Plechacek, S. Kamba, P. Losta k, J. S. Dyck, W. Chen, and C. Uher, J. Sol. Stat. Chem. **177** 1704 (2004).

[168] Y. S. Hor, A. Richardella, P. Roushan, Y. Xia, J.G. Checkelsky, A. Yazdani, M. Z. Hasan, N.P. Ong, and R.J. Cava, arXiv:0903.4406.

[169] D. L. Greenaway and G. Harbeke, J. Phys. Chem. Sol. **26**, 1585 (1965).

[170] W. Richter, H. Kohler, and C. R. Becker, Phys. Stat. Sol. (b) **6**, 619 (1977).

[171] A. Sklenar, C. Drasar, A. Krejcova, and P. Lostak, Cryst. Res. Technol. **35**, 1069 (2000).

[172] V. A. Kulbachinskii, N. Miura, H. Nakagawa, H. Arimoto, and T. Ikaida, P. Lostak and C. Drasar Phys. Rev. B **59**, 15 733 (1999).

[173] V.A. Kulbachinskiia, A.Yu. Kaminskiia, V.G. Kytina, A. de Visser, JMMM **272276**, 1991 (2004).

[174] P. Janicek, C. Drasar, P. Lostak, J. Vejpravova, and V. Sechovsky, Physica B **403**, 3553 3558 (2008).

[175] H. Kohler and J. Hartmann, Phys. Stat. Sol. (b) **63**, 171 (1974).

[176] U. Fano, Phys. Rev. **124**, 1866 (1961).

[177] G. Abstreiter, M. Cardona, and A. Pinczuk, Light Scattering in Solids IV, Topics in Applied Physics Vol. 54 (Springer Verlag, Heidelberg, 1984), pp. 10150.

[178] Andrea Damascelli, Ph. D. dissertation, University of Groningen (1999).

[179] Kensuke Kobayashi, Hisashi Aikawa, Akira Sano, Shingo Katsumoto, and Yasuhiro Iye, Phys. Rev. B **70**, 035319 (2004).

[180] Jinhee Kim, *et al.,* Phys. Rev. Lett. **90**, 166403 (2003).

[181] D. V. Vasilenko, N. V. Lukyanova, and R. P. Sesyan, Semiconductors **32**, 15 (1999).

[182] S. Glutsch, U. Siegner, M. -A. Mycek, and D. S. Chemla, Phys. Rev. B **50**, 17009 (1994).

[183] V. S. Edelman, Adv. Phys. **25**, 555 (1976).